

Population Kinetics of a Repetitively-Pulsed Nanosecond Discharge

by

Benjamin T. Yee

A dissertation submitted in partial fulfillment
of the requirements for the degree of
Doctor of Philosophy
(Nuclear Engineering & Radiological Sciences)
in the University of Michigan
2013

Doctoral Committee:

Associate Professor John E. Foster, Chair
Doctor Edward V. Barnat, Sandia National Laboratories
Doctor Isaiah M. Blankson, National Aeronautics and Space Administration
Professor Augustus Evrard
Professor Mark J. Kushner

©Benjamin T. Yee

2013

I would like to dedicate this dissertation to someone else.

A C K N O W L E D G M E N T S

Who is this?

Preface

This is a dissertation about something; I really hope it's good.

TABLE OF CONTENTS

Dedication	ii
Acknowledgments	iii
Preface	iv
List of Figures	vii
List of Tables	ix
List of Appendices	x
List of Abbreviations	xi
 Chapter	
1 Introduction	1
1.1 Overview	1
1.1.1 Motivation	1
1.1.2 History	4
1.1.3 Questions	7
1.1.4 Approach	8
1.2 Literature Review	9
1.2.1 Early History of Pulsed Discharges	9
1.2.2 The Streamer Model	11
1.2.3 Diffuse Streamers	12
1.2.4 Repetitively-Pulsed Nanosecond Discharges	14
1.3 Summary	16
2 Theory	19
2.1 Ionized Gas	19
2.2 Plasma Criteria	23
2.2.1 Debye Length	23
2.2.2 Debye Sphere	24
2.2.3 Plasma Oscillations	24
2.3 Discharge Initiation	26
2.3.1 Townsend Mechanism	26
2.3.2 Streamer Mechanism	27

2.3.3 Homogeneity Condition	28
2.4 Atomic Spectroscopy & Notation	31
2.4.1 Spectral Lineshapes	36
2.4.2 Absorption	38
3 Experiment	41
3.1 Discharge Apparatus	41
3.2 Field Calculations	46
3.3 Operating Procedures	48
3.4 Electrical Characteristics	49
3.5 Energy Coupling	52
4 Metastable Measurements	54
4.1 Setup	56
4.2 Noise Suppression & Absorption Analysis	60
4.3 Results	63
4.3.1 Temperatures	64
4.3.2 Line-integrated Densities	67
4.3.3 Metastable Destruction	70
4.4 Summary	74
5 Modeling	76
5.1 Model Development	77
5.1.1 Continuity Equation	78
5.1.2 Distribution Effects	81
5.1.3 Energy Equation	86
5.1.4 Model Solutions	88
5.2 Perturbation Study	90
5.3 Plasma Dynamics	91
5.4 Summary	91
6 Population Kinetics	92
7 Conclusions	93
Appendices	94
Bibliography	97

LIST OF FIGURES

1.1	A simplified depiction of the avalanche breakdown process in a gas.	2
1.2	A sketch of J.J. Thomson's early experiments on pulsed plasmas in long vacuum tubes [1].	10
2.1	Comparison of the Maxwell-Boltzmann energy distribution and the Druyvesteyn distribution for the same average energy (illustrated by the dotted line).	21
2.2	Illustration of the various regimes of plasma in terms of electron temperature and density with the RPND regime highlighted, adapted from [2].	25
2.3	An illustration of the development of a single streamer. (a) A seed electron is accelerated by the applied electric field. (b) The initial electron develops into an avalanche which leaves a large region of positive space charge, slowing further advance. (c) The streamer propagates toward the cathode via photoionization and the anode via nonlocal electrons and photoionization. Adapted from [3] and [4].	28
2.4	Numerical calculations of the avalanche length and avalanche radius for in helium at a pressure of 4.0 Torr as a function of the slope of the electric field, dE/dt	30
2.5	Minimum preionization densities required at a variety of pressures and breakdown delays. The dotted line indicates the background ionization level as a result of cosmic radiation.	31
2.6	A partial Grotrian diagram of neutral helium, from [5].	35
2.7	A comparison of the three primary spectral lineshapes, each with the same full width.	37
3.1	Two illustrations of the RPND apparatus. The upper version is an annotated sketch of the device, and the bottom version simplifies the geometry into its three electrical components.	42
3.2	Simplified diagram of the gas flow path and pumping system.	44
3.3	Photograph of the discharge apparatus.	45
3.4	Sketch of the unassembled back-current shunt, and a photograph of it assembled around the transmission line.	46
3.5	Heatmap and vector plot of the electric field in the RPND discharge apparatus.	47
3.6	Typical voltage waveform of the RPND. Arrows indicate reflections back to the power supply. The dotted line delineates the time at which the power supply begins to exhibit double pulsing.	49

3.7	High resolution views of the voltage and current waveforms for the first incident and reflected pulse, at each of the operating pressures.	51
3.8	Plot of the energy coupled into the discharge with the first pulse as a function of pressure.	53
4.1	Optical beam path of the laser in the absorption spectroscopy experiment. DFB - Distributed feedback laser diode; FI - Faraday isolator; ND - neutral density filter; S - shutter; PD - photodiode; AP - aperture.	57
4.2	Measurement of the transmitted laser light at the nominal transition wavelength at 4.0 Torr of helium.	59
4.3	Heatmaps of the transmitted laser signal for the 4.0 Torr condition at various stages of post-processing.	61
4.4	Comparison of the measured transmission profile (open symbols) and the computer-generated matches for at several different times for the 4.0 Torr operating condition.	63
4.5	Plot of the gas temperatures at each of the operating pressures and each axial location as a function of time.	65
4.6	Plot of the average gas temperature as a function of deposited energy.	66
4.7	Plots of the line-integrated metastable densities at each of the operating pressures and each axial location as a function of time.	68
4.8	Zoomed in view of the increases in metastable density as a result of pulse reflections.	69
4.9	Measurements of the long-duration metastable density trends. Exponential fits are indicated by the dotted lines.	71
4.10	Peak line-integrated metastable densities as a function of pressure.	72
4.11	Comparison of the decay rates for various processes at 0.3 Torr as a function of metastable density.	73
5.1	Schematic description of the PIC simulation process, adapted from [6].	82
5.2	Contour plots of the EEDFs determined from PIC simulations, and the corresponding Maxwell-Boltzmann distributions for a range of electric fields.	85
5.3	Simulations showing the effects of perturbations to the initial conditions on the metastable dynamics.	90

LIST OF TABLES

4.1 Listing of the extrapolated, pre-pulse line-integrated metastable densities, and decay coefficients as a function of pressure.	74
--	----

LIST OF APPENDICES

A Millimeter-Wave Interferometry	94
B Rotational Spectroscopy	95

LIST OF ABBREVIATIONS

RPND repetitively-pulsed nanosecond discharge

DBD dielectric-barrier discharge

APP atmospheric-pressure plasma

EEDF electron energy distribution function

FIW fast ionization wave

LAS laser-absorption spectroscopy

LCIF laser collision-induced fluorescence

MHD magnetohydrodynamic

FWHM full-width half maximum

FID fast ionization dynistor

PTFE polytetrafluoroethylene

PIC particle-in-cell

CHAPTER 1

Introduction

1.1 Overview

1.1.1 Motivation

Plasmas, commonly called the fourth state of matter, are a gas where a significant fraction of the neutral atoms or molecules have been split into pairs of electrons and positive ions. Initially, a curiosity of the laboratory, they have become a critical part of every day life. The electrically charged nature of plasmas makes them a practical means by which to convert electrical energy into electromagnetic, chemical, kinetic, or even nuclear energy. From an applications perspective, they are indispensable in lighting, semiconductor manufacturing, plastic processing, and space propulsion. On a more broad scale, virtually all observable light in the universe is the result of a plasma in some form or another [7].

Some exceptions aside, only three things are required to create a plasma: a gas, an energy source, and a means of transferring the energy to the gas. In man-made applications, the energy source is typically electricity, and the simplest transfer mechanism is via two electrodes placed on either side of the gas. The application of a potential difference to these electrodes produces an electric field as seen in figure 1.1. The field accelerates a single seed electron in the gas (often created by background cosmic radiation) until it collides with a neutral particle. The electron, having acquired a sufficient amount of energy, liberates a second electron loose from the particle, leaving behind a relatively heavy and immobile



Figure 1.1: A simplified depiction of the avalanche breakdown process in a gas.

ion. Subsequently, both the first and second electron are now accelerated by the electric field. Again, they collide with two more neutral atoms, creating two new electrons. As long as the electric field persists, the number of electron and ion pairs increases exponentially. This process is generally referred to as an avalanche.

Eventually, the production of ions and electrons in the gap balances out with the rate at which they leave the system, whether by collection at the electrodes or some other process. The resulting ionized gas may be referred to as a plasma if it meets certain criteria. Simply put, there must be a high enough density and number of charged particles for their electromagnetic interaction to dominate over random collisions with neutral gas particles.

Despite this relatively simple recipe, the physical characteristics can vary greatly depending on what gas is used, what pressure it is at, what voltage is used, whether the electricity is applied constantly or varied over time, what kind of electrodes are used, etc. As a result, man-made plasmas are generally produced under very specific conditions. For example, a plasma etcher used in semiconductor manufacturing may need to operate oper-

ate at pressures that are one-thousandth of atmospheric pressure with ultra-pure (99.999%) gases [8].

Plasmas like those which occur in plasma etchers, feature ions and neutral gas particles with temperatures that are below 1,000 K, or roughly 1,340° F. Though this temperature is relatively high compared to room temperature, it is well below the temperature of the electrons which may be in excess of 20,000 K. Plasmas which exhibit this disparity in temperatures are often called nonequilibrium or “low-temperature” plasmas.

Conversely, there exists another class of plasmas where the electrons, ions, and neutral particles are all at the same temperature. These are called thermal plasmas. Generally speaking, the closer the gas pressure is to atmosphere, the more thermal a plasma is owing to the rapid increase in the frequency of collisions between neutral and charged particles [9]. Additionally, the temperatures in a thermal plasma can be quite high and, in many cases, can easily melt all metals assuming that the total energy content of the plasma is high enough. For example, the arc of an arc welder is a thermal plasma. Similar high temperature plasmas, have a number of other applications which include a variety of high-intensity lamps, metal cutting, and surface coating.

There are, however, a number of applications which would benefit from operation at higher pressures, but with low-temperature ions and neutrals so as to avoid heat damage. This has spurred a substantial amount of research on nonequilibrium atmospheric-pressure plasmas (APPs) in recent years [10]. Ideally, such a plasma could be generated at or near atmospheric pressure with hot electrons, but minimal heating of surrounding gas. Though this field of research is still relatively young, it has produced a variety of new plasmas and capabilities. One of the more ubiquitous examples is use of plasmas to process the surface of plastics so that ink can adhere. Separately, nonequilibrium APPs are the technology which drives plasma televisions [11].

As mentioned, these applications promise to be the first of many for such plasmas. More recently, there have been innovative proposals to use these plasmas in water purification

[12], wound sterilization [13], improved combustion engines [14], nanoparticle production [15], and more. However, each situation has its own challenges when it comes to the design and development of a plasma source, particularly at these elevated pressures. Particularly problematic is the tendency of APPs to develop instabilities which can cause them to rapidly transition to thermal plasmas in a matter of nanoseconds.

There exist a few ways of getting around these instabilities. One example is the dielectric-barrier discharge which passively regulates the amount of power which can be deposited into the plasma [16]. Another example includes split-ring resonators which use natural feedback mechanisms to damp out potential instabilities [17]. The technique considered here, referred to as the repetitively-pulsed nanosecond discharge, or RPND, uses high voltage pulses which are so short that the instability does not have time to develop [18]. The RPND is a nonequilibrium plasma which can operate at pressures ranging from approximately 10^{-3} –1 atmospheres [19]. At atmospheric pressure the RPND can produce a uniform plasma in volumes on the order of 10 mL [20]. As the pressure is reduced, the plasma volume can reach the order of liters [21].

The importance of large-area, uniform, high-pressure plasmas such as the RPND was highlighted in the National Academies' most recent decadal survey of plasma science [7]. However, there is still much that is not known about such plasmas. From the same survey, it is said that “the full promise of APPs will be known only if they can be understood and managed based on fundamental scientific principles at two extremes—the nanoscopic kinetic level, where selective chemistry occurs, and the global stability level.” It is this challenge, specifically the investigation of the nanoscopic kinetic level, which drives the research presented here.

1.1.2 History

Historically, the study of low-temperature APPs has been almost indistinguishable from the study of plasmas as a whole. However, this was not necessarily a matter of reasoned choice.

Plasma generation at atmospheric-pressure obviates the need for an effective vacuum pump. Additionally, prior to the creation of large battery banks, early sources of electrical energy had relatively small capacities. This precluded the generation of thermal atmospheric plasmas which required large amounts of energy.

Indeed, the requirements for a low-temperature APP are sufficiently rudimentary that the first man-made one (and likely the first man-made plasma), was probably a spark generated by rubbing fur against amber. This is commonly attributed to Thales of Milêus from around 600 B.C. Following Thales, electrical sparks came to intrigue many scientists including Gottfried Liebniz, Benjamin Franklin, and Charles Wheatstone. By the mid-1800s, Plücker, Geißler, and Hittorf began some of the first work on low-pressure plasmas though it was Crookes who would later identify plasma as a separate state of matter. Later, J.J. Thomson's discovery of the electron and discretized charge in 1897 marked the beginning of modern plasma research.

By this time, the necessary tools and techniques existed to create steady plasmas in pure, rarified gases. The behaviors of which were dominated by the motion and interaction of the charged electrons and ions. Critically, the effects of the neutral particles were negligible, thus isolating the electrical properties of the plasma. These carefully controlled systems were ideal for basic studies of plasma behavior and were used to great effect by individuals such as Lewi Tonks and Irving Langmuir [22]. In fact, many modern concepts in plasma physics can be traced back to their work.

In contrast, the pulsed APPs, characteristic of the earliest man-made plasmas [23], were easy to create, but notoriously difficult to work with. It could take them only a few nanoseconds to form, and less than a millisecond to decay away. For many years, there were simply no instruments capable of taking measurements this quickly. Furthermore, the neutral particles which were of no consequence in the low-pressure plasmas, could not be ignored. The neutral particles were present in such quantities that they could confound or obscure otherwise simple measurements.

As a consequence, there is still a great deal that is not known about pulsed APPs, particularly lightning, streamers, and a type of plasma which Thomson referred to as a “luminous front.” By the 1970s, this latter plasma had come to be called the fast ionization wave, or FIW [19]. It was generated by a single voltage pulse lasting around 100 nanoseconds and peaking at 10s or 100s of kilovolts. For the right pressure and gas, the FIW could fill volumes of nearly 40 L with a relatively uniform plasma, but with little heating of the gas.

These properties were attractive for a number of uses, but the FIW faced a number of implementation-related challenges. The switches used to trigger the FIW could only operate up to 100 times each second [24]. Unfortunately, the lifetime of a plasma at elevated pressures is relatively short, and the plasma generated by the FIW would decay away quickly after each pulse. This meant that the FIW-generated plasma had a relatively low duty cycle; the ratio of the time the plasma spends on to the time it spends off. This was disadvantageous for plasma-processing applications where low duty cycles are equivalent to long processing times. The low duty cycle also necessitated so-called preionization of the gas with UV lamps or a secondary plasma generator, adding to the cost and complexity of the system [3]. Finally, the pulse generators used for FIWs were not considered reliable enough for long operational lifetimes.

Recent advances in solid-state switching technology has largely solved these issues. At present, switches exist which can reliably operate 100,000 times a second; sufficiently fast that the plasma duty cycle approaches 100% [25]. This has the additional benefit of obviating the need for a preionization stage, as a sufficient number of electrons persist between pulses. The discharge produced by the use of these new switches is what we refer to as the RPND.

1.1.3 Questions

The large pedigree of pulsed plasma research belies the fact that they are still not well-understood. This remains especially true for RPNDs which present significant experimental challenges. A major component of this has to do with the time scales associated with the RPND. The formation of a RPND often requires no more than a few nanoseconds. Very sensitive equipment is required in order to measure changes which occur during this period. Unfortunately, such equipment is particularly susceptible to the broadband electronic noise generated by both real and displacement currents of the fast pulses. There is a plethora of other problems that can be traced back to topic of timing. For example, the length and insulators of detector cables can introduce substantial delays, and must be considered in order to synchronize different measurements.

Consequently, the majority of RPND studies focus on measurements after the discharge has occurred, when changes happen at a much slower rate. A great deal of information is available for this period of time, including chemical compositions, atomic densities, electron densities, gas temperatures, and more. While undoubtedly important, these measurements provide limited insight on what is happening *while* the plasma is forming. It is natural, then, to ask, what are the RPND plasma properties during formation?

Additionally, most studies have used a limited range of gases: oxygen, nitrogen, air, hydrogen, or some mixture thereof. The choice of these gases is deliberate and reflects specific applications in combustion and aerospace. However, the use of rare gases (such as helium) and rare gas mixtures has become popular because they provide for a wider range of stable operating conditions. Notably, it has been found that the unique internal electronic structure of rare gases can produce very different discharges. Given this, there is the question of how rare gas RPNDs compare to more conventional ones.

Finally, the persistence of the plasma between pulses makes the development of a RPND very different from a FIW.

Finally, though the RPND and FIW are qualitatively similar, there are some fundamental

differences between the two. These largely stem from the persistence of the plasma between pulses. It is this plasma which guarantees uniform breakdown in the case of RPND, while the FIW is largely dependent on very high energy electrons. At the same time, if the plasma is too dense at the beginning of the voltage pulse, it can limit the final density of the electrons and excited atoms. Because plasma-induced chemistry is a product of these particles, this pre-pulse plasma plays a decisive role in the number of reactions a RPND can produce. Therefore, one must ask how the properties of a RPND compare to those of a FIW and how they vary with the operating conditions.

1.1.4 Approach

The dissertation presented here represents efforts to either answer or provide a foundation to answer these questions. In order to develop the appropriate context for this work, the next section will be a comprehensive review of the RPND literature. It begins with the first reported pulsed APPs and concludes with contemporary studies.

The following two chapters set the basis for the experimental and numerical studies. Chapter 2 presents the theory necessary to understand RPNDs including streamer discharges, atomic spectroscopy, and collision processes. Subsequently, Chapter 3 describes the design of the helium RPND discharge apparatus used for the experimental studies and as the basis for the simulations. Also included in this chapter are several measurements of the basic discharge properties.

Chapters 4 through 5 provide more detailed measurements and analysis of the RPND dynamics. In Chapter 4, the measurements of the helium metastables in a RPND are presented and analyzed as a function of pressure and axial location in the discharge apparatus. Chapter 6 presents and analyzes similar measurements of the spontaneous plasma emissions. Finally, Chapter 5 discusses the development of a global model for a helium plasma and its use with the experimental data to infer the plasma properties of the RPND. The dissertation concludes with a summary of the results and suggestions for further avenues of

research.

1.2 Literature Review

RPNDs are only a recent invention which resulted from advances in fast-switching semiconductors. However, the physics of their formation is related to a much more broad category of plasmas which includes lightning, streamers, and even some transient phenomena in DC glows [26]. These plasmas are unique in that their spatial structure develops at speeds much faster than can be accounted for by the conventional Townsend mechanism. Loeb refers to this phenomena as “ionizing waves of potential gradient.”¹.

1.2.1 Early History of Pulsed Discharges

In 1835 (as reported by Thomson [1]), Charles Wheatstone attempted to measure what he thought to be the speed of electricity in a six-foot long discharge tube of unspecified pressure [27]. It is now known that he was actually measuring the speed with which a plasma formed between the two electrodes. He accomplished this by the use of a rotating mirror which allowed him to see images of two sections of the tube, slightly displaced. The displacement between the images was proportional to the speed with which the plasma traveled between them. Wheatsone estimated this speed to be at least 8×10^7 cm/s.

Interestingly, von Zahn later noted that this was *not* the speed of the emitting particles [28]. The visible light did cross the gap at an appreciable speed, but there was no detectable Doppler shift in the light emitted parallel to the propagation. As a result, it was concluded the light-emitting particles could not be traveling at the same speed as the light.

Later, Thomson revisited this work with an improved apparatus [1]. This included a tube that was now 15 m in length and five mm in diameter, as seen in figure 1.2. Also

¹It should be noted that the phrase wave does not indicate any kind of periodic motion or spatial arrangement. Simply put, it describes a boundary which separates ionized and unionized gas which travels from one electrode to another.

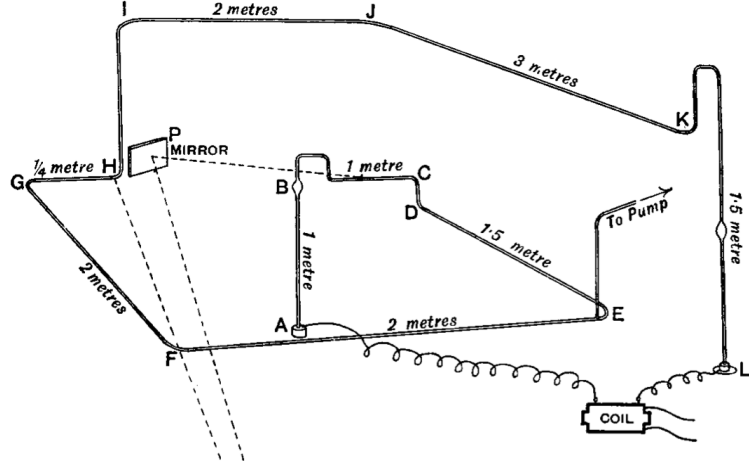


Figure 1.2: A sketch of J.J. Thomson’s early experiments on pulsed plasmas in long vacuum tubes [1].

using the rotating mirror apparatus, Thomson was able to greatly improve on the estimates of Wheatstone. He estimated that the so-called “luminous front” had a speed that was more than 1.5×10^{10} cm/s, or in excess of half of the speed of light. Furthermore, Thomson determined that the luminous front always appeared to travel from the positively pulsed electrode (anode) to the ground electrode (cathode).

The study of these luminous fronts was revisited by several researchers in the wake of Thomson [29–31], but their attempts to duplicate the measured speeds were met with varied success. In 1930, Beams confirmed definitively those of Thomson. He also found that the front always initiated at the electrode with the highest, absolute potential, relative to ground. Beams hypothesized that the rapid motion of the front was a result of a self-propagating region of high space charge, quote:

In the neighborhood of the electrode . . . the field is very high and intense ionization should take place. This ionization due to the large difference in mobilities of positive ions, negative ions and electrons respectively should result in the establishment of a space charge. This space charge, once formed near the high potential electrode . . . must move down the tube regardless of the polarity of the applied potential because of the changes it produces in the field near its edges.

At about the same time, Schonland and Collens reported on their observations of lightning [32]. Though the general structure and length scale of lightning is substantially different from the luminous fronts observed by Beams and Thomson, the two phenomena would later prove to be very similar. In their work Schonland and Collens noted that lightning would usually occur in a two-step process. Based on the images they obtained, they suggested that the leader was generated by a relatively small “dart” with a mean vertical velocity of 7.2×10^8 cm/s. The dart moved in a random manner, changing directions at random intervals, but always moving toward the ground.

The second step began when this dart reached the ground. Once there, a bright return stroke would occur along the same path that the leader had traced out. In contrast to the leader stroke, the return stroke had a velocity of 5×10^9 cm/s. Schonland and Collens hesitantly attributed the leader stroke to an extended electron avalanche, and the return stroke to thermal ionization along the conductive path generated by the dart. However, calculations by Cravath and Loeb showed that the speeds of the proposed avalanche was inconsistent with the fields at the head of a lightning stroke [33]. Instead, they suggested that the dart was actually a moving region of space charge which locally accelerated electrons to ionizing energies. This was similar to the mechanism earlier proposed by Beams.

1.2.2 The Streamer Model

It was long known that sparks in air were similar to lightning. Advances in technology during the 1930’s led to experiments which reinforced this similarity. In response to the measurements of Schonland and Collens; Snoddy, Beams, and Dietrich studied the breakdown of gas in a long tube with both positive and negative applied potentials [34]. Using an oscilloscope, they observed both the leader and a return stroke in both cases. However, the propagation of the plasma wave toward the cathode required a source electrons ahead of the wave. The authors proposed that photoionization might provide these necessary electrons.

Around the same time, Flegler and Raether had come to a similar conclusion regarding

the importance of photoionization. This led them to develop a more thorough theoretical model for these waves [35] which came to be known as the streamer theory. This was followed by a similar treatment by Loeb and Meek [36–38]. The streamer theory divided the initial plasma formation into two steps. In the first step, an electron avalanche is initiated between two electrodes. The avalanche travels toward the anode and leaves behind a region of positive space charge. In the second step, the return stroke begins at the anode and travels along the conductive path generated by the initial avalanche toward the cathode.

The streamer model proved relatively successful in describing the development of sparks and lightning. Theoretical estimates of the speed matched the velocity measurements that were acquired with photographs and oscillographs. Additionally, the theory was able to account for the branching manner in which lightning was formed as well as the constriction in space.

Following the initial work of Flegler, Raether, Loeb, and Meek, a number of researchers began to explore the boundary between the Townsend mechanism and the streamer mechanism. Most notable was Fisher and Bederson’s work in 1951 [39], which was later extended to nitrogen [40] and argon [41]. These studies suggested that the streamer theory was incomplete. Furthermore, the reliance of the streamer theory on photoionization would later prove very contentious [42]. Finally, there was a whole class of discharges that it did not readily explain.

1.2.3 Diffuse Streamers

As noted by Chalmers [43], Rogowski and Buss [44, 45] observed a fast, diffuse, glow discharge immediately prior to the filaments of a streamer discharge. Allibone and Meek, noted similar diffuse discharges in air based on oscillographs and photographs [46–48]. However, the Boys apparatus [49] which was employed in these studies (an ancestor to the modern streak camera) was unable to capture the evolution of the diffuse glow, given its large spatial extent.

This was first noted by Allibone who attempted to use Lichtenberg figures² to definitively capture this diffuse glow [50]. Later, Saxe and Meek used the recently invented photomultiplier tube to record the evolution of the light emissions in the brief, diffuse glow [51] as a function of space. Both studies agreed in the existence of the diffuse glow, despite some disagreement on the nature of its geometry and propagation.

By 1968 (according to Kunhardt and Byszewski [4]), Stankevich and Kalinin had provided the most firm evidence yet of a diffuse discharge in a dense gas [52]. This was later confirmed by experiments with a pulsed nanosecond discharge by Mesyats, Bychkov, and Kremnev [53]. In their analysis, they concluded that photoionization could not play a role in such short-lived discharges. The formation of their discharge only required several nanoseconds, much shorter than the lifetimes of the excited states responsible for photon emission. They suggested that the streamer model required some extension.

In addition to the diffuse discharge, Stankevich and Kalinin also noted the detection of x-rays with each pulse. This suggested the presence of high-energy electrons impinging on the surface of the electrodes, despite the high collisionality of the dense gas. Not only that, but the electron energies could even exceed what would be expected from the vacuum electric fields [54]. The eventual conclusion was that the electric field associated with the space charge at the head of the streamer produced very energetic electrons which deposited their energy far from the streamer tip [4,55], allowing the streamer to spread out beyond the diffusive region of the electrons.

It was based on the studies of the fast electrons in these discharges that Mesyats, Bychov, and Kremnev proposed the use of a fast electron beam for pumping high-pressure gas lasers. Similar work was conducted simultaneously by Fenstermacher et al. [56]. Palmer [57], and Levatter and Lin [3] determined that there was a threshold amount of preionization required to ensure homogeneity of the discharge. Hunter [58], and Koval'chuk and Mesyats [59] later proposed that such discharges be used for fast-closing switches. Gas lasers and fast

²Such figures directly exposed photographic emulsions to the electrical discharge. The developed image was a time-integrated representation of the discharge.

switches would drive much of the later research on fast, pulsed discharges.

Eventually these discharges came to be referred to as fast ionization waves (FIWs). A large body of Russian literature developed around their study, though much of it has remained untranslated. In 1994, Vasilyak produced an extensive review of these studies [19]. The data include wave velocities for a variety of gases and pressures. Other parameters such as attenuation coefficients for the waves, high energy electron currents, electric field measurements, and a circuit model of the FIW are also included.

1.2.4 Repetitively-Pulsed Nanosecond Discharges

The type of discharge originally studied by Babich, Loika, and Tarasova came to be known as the fast ionization wave (FIW). In the years following its discovery, a substantial effort was made to document the properties of the FIW over a wide range of conditions. In these studies, the wave velocity, current, and attenuation were the most frequently measured quantities. Much of this work is summarized in a review by Vasilyak [19]. Also reviewed are Slavin and Sopin's work which was the first to attempt a computation of the electron energy distribution function EEDF in FIWs [60].

The experimental measurements and computational work reported by Vasilyak were expanded on by a series of studies conducted at the Moscow Institute of Physics. These are reviewed by Starikovskaia et al. [24] and included measurements of the electron density, electric field, and energy coupling for FIWs in air, nitrogen, and hydrogen. The computational work by Starikoskaia and Starikovskii [61] still represents the most detailed study of the EEDF in nitrogen FIWs.

However, Starikovskaia et al. noted that the usefulness of FIWs were limited, in part, by their repetition rates. The power supplies for FIWs were capacitor banks, charged in parallel, and discharged in series (also referred to Marx banks). Unfortunately, the spark gaps used to trigger these capacitor banks would not operate above a few hundred Hz. This changed in the late 1990's with the development and commercialization of fast, solid-state

switches. Specifically, with the fast ionization dynistor it was possible to achieve repetition rates of 100 kHz [25].

This led to a new class of repetitively-pulsed discharges, or the RPND. These discharges operated at sufficiently high rates such that the electrons and ions would persist in significant quantities between pulses. This meant that the plasma duty cycle was increased by a significant amount. These improved qualities of the RPND over the FIW inspired a number of novel, application-driven studies. This included:

- Plasma-assisted combustion [18, 62, 63]
- Magnetohydrodynamic energy bypass engines [18, 64, 65]
- Plasma actuators [66, 67]
- High-pressure xenon lamps [68]
- Plasma medicine [13, 69]
- Water treatment [70]

Though not specific to the RPND, Becker et al. [10] provide an extensive discussion of the potential uses for non-equilibrium air plasmas.

As a result, contemporary researchers have produced a wealth of literature on the operation of RPNDs. More recently, there have been detailed measurements of the gas temperatures [62, 71–77], chemical composition [73–75], electric fields [78–80], and energy coupling [62, 81]. Notably, these studies have been generally restricted to molecular gases; air, nitrogen, and occasionally, hydrogen.

The first such study was the work of Laroussi and Lu who examined a RPND excited in a stream of helium flowing from a tube into air [82, 83]. The resulting plasma had the appearance of a jet, emitted from the open end of the tube. Using fast photography they observed that the jet was actually a series of plasma “bullets” formed with each pulse. Measurements of the bullet velocities showed that their speed greatly exceed what would be

expected purely from electrons drifting under the applied electric field. They described the bullet as a classic cathode-directed streamer propagated by photoionization.

The plasma bullets of Laroussi and Lu spawned a great deal of interest in RPND helium plasma jets³ For example, Walsh et al. studied the atomic oxygen production for helium-oxygen mixtures with the use of emission spectroscopy and a global plasma chemistry model [84]. Urabe et al. employed a variety of laser diagnostics to measure the radial density profiles of helium metastable atoms and molecular nitrogen ions in a similar jet. This work was supported by a number of two-dimensional plasma simulations such as those by Naidis [85] and Breden, Miki, and Raja [86].

Simultaneously, there has been a decline in the study of FIWs, and relatively little on large-volume RPNDs. One of the most recent FIW studies was produced by Takashima et al. [87]. In it, the authors reported on FIWs in helium and nitrogen which were studied using capacitive probes and voltage-current characteristics. The results were compared to extensive two-dimensional fluid simulations and an analytic, one-dimensional drift model. In most cases, the measurements and simulations showed good agreement.

1.3 Summary

Contemporary RPND studies have mostly focused on measurements in the afterglow plasma or of time-integrated quantities. This has limited the understanding of how RPNDs develop as only so much can be inferred from these measurements. Particular issues, such as the electron energetics in the wave front are not firmly known. Relatedly, the relative importance of photoionization and nonlocal electrons is still under debate. Even measurements of common plasma parameters such as electron densities and temperatures are in short supply. Each of these issues is important in the development of a thorough theoretical understand-

³A distinction should be made between plasma jets, excited by sinusoidal power supplies, similar to the well-known dielectric-barrier discharge [16], and those produced by nanosecond pulses. Differences between the two were reported by Walsh, Shi, and Kong [20].

ing of RPNDs, as well as the validation of simulations, and optimization for real world applications.

Relatedly, the study of RPNDs has generally been limited to molecular gases such as air, nitrogen, oxygen, or combustion-related mixtures. Consequently, little information has been published on rare gas RPNDs, in spite of the fact that their unique physics makes them ideal for certain uses. For example, rare gas discharges exhibit very little gas heating, making them desirable for the treatment of highly sensitive materials. Additionally, the radiative emissions of rare gases have a range of uses from commercial lighting to gas lasers. Finally, the large degree of Penning ionization resulting from rare gases may make them useful in RPND gas mixtures as a means of optimizing discharge properties.

In order to address these issues, this work will use a combination of experiments and modeling to examine the plasma dynamics of a helium RPND on time scales ranging from 5 ns to 100 μ s and at pressures from 0.3 to 16.0 Torr. The nanosecond time scale results will be one of a very few datasets available on the evolution of the RPND during its formation. This will provide new insight on the dominant physical processes in the wave front. To complement this, the microsecond time scale measurements will reveal the dominant loss mechanisms in between pulses as well as the time-averaged characteristics of the RPND. Lastly, the parameterization with pressure will offer the chance to examine how the physics of the discharge is altered by the collisionality.

Experimentally, the RPND will be studied by its current and voltage characteristics, optical emissions, and with laser absorption spectroscopy. The current and voltage characteristics will be used to determine the energy absorbed by the plasma with each pulse. The optical emissions will provide information about the excited state dynamics and the wave velocity. Finally, the laser absorption spectroscopy will be used to resolve the short time scale dynamics and as a benchmark for the numerical modeling. The modeling will focus on the development of a detailed global model of a helium discharge. This model will be informed by additional particle-in-cell simulations, and solutions of the Boltzmann equa-

tion. Using the metastable measurements as a baseline, the global model will be used to predict the electric field, electron temperature, electron density, excited state densities, and emissions of the RPND.

CHAPTER 2

Theory

In order to properly understand the RPND—the experimental measurements, and the models, it is necessary to develop a theoretical underpinning. The RPND is an ionized gas, and, dependent on its characteristics, a plasma. Therefore, we begin with a review of the statistical description of an ionized gas, equilibrium solutions, and several approximations. Subsequently, the discharge initiation process is considered from the perspective of a single avalanche. The Townsend model is briefly reviewed, followed by a more detailed explanation of the streamer model. This naturally leads to the development of a homogeneous discharge condition based on the preionization density—the basis for the RPND. Following this, a qualitative introduction to atomic structure is provided in order to introduce spectroscopic concepts such as energy levels, transitions, lineshapes, and absorption cross sections.

2.1 Ionized Gas

An ionized gas is a volume of gas in which some fraction of the neutral atoms and/or molecules have been separated into electron and ion pairs. For a sufficiently large number of particles and collision rate, the behavior of each species in the ionized gas can be described by a continuous distribution function.

This function is an expression of the likelihood of finding a particle within a specific range of velocities in a specific volume, as a function of time. This function is denoted as

$f_\alpha(\vec{r}, \vec{v}, t)$, where the subscript α denotes the species, f is the distribution function, \vec{r} is the position, \vec{v} is the velocity, and t is the time.

The behavior of f_α can be shown [88] to be governed by the Boltzmann equation,

$$\frac{\partial f_\alpha}{\partial t} + \vec{v} \cdot \nabla f_\alpha + \frac{q_\alpha}{m_\alpha} (\vec{E} + \vec{v} \times \vec{B}) \cdot \nabla_v f_\alpha = \left(\frac{\partial f_\alpha}{\partial t} \right)_{\text{coll}}. \quad (2.1)$$

Here, m is the particle mass, q is its charge, \vec{E} is the electric field, \vec{B} is the magnetic field, and $(\partial f_\alpha / \partial t)_{\text{coll}}$ is a term which represents changes to the distribution function as a result of collisions. Coupled with Maxwell's equations, equation 2.1 provides a complete description of the behavior of the fields and particles in a plasma.

For a species in equilibrium in the absence of external forces and $(\partial f_\alpha / \partial t)_{\text{coll}} = 0$, it can be shown [89] that the distribution of energies is

$$f_\alpha(\epsilon) = C \epsilon^{1/2} \exp\left(-\frac{\epsilon}{k_B T_\alpha}\right) \quad (2.2)$$

where C is a normalizing constant, ϵ is the energy, k_B is Boltzmann's constant, and T_α is the temperature of the species. This is referred to as the Maxwell-Boltzmann distribution. It should be emphasized that this solution only applies when the classical species can be considered to be in equilibrium. Gradients and electromagnetic fields can both significantly alter the distribution function of a species. This can be of particular importance in the calculation or reaction rates, or the measurement of temperatures.

Additionally, the Boltzmann equation may be solved for electrons in equilibrium constant electric field, provided that a constant current density, and only elastic collisions. This is generally valid if the electric field strength is sufficiently small such that the mean energy of the electrons does not become comparable to the threshold energies for inelastic collisions. This result was originally presented by Druyvesteyn and Penning [89] and has come

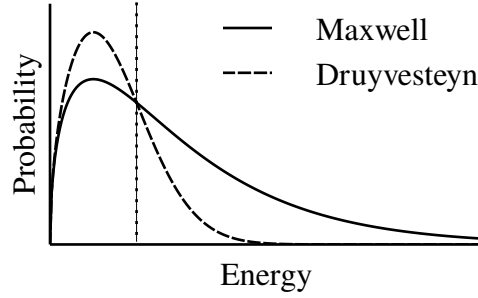


Figure 2.1: Comparison of the Maxwell-Boltzmann energy distribution and the Druyvesteyn distribution for the same average energy (illustrated by the dotted line).

to be known as the Druyvesteyn distribution. It is defined as,

$$f_\alpha(\varepsilon) = C \varepsilon^{1/2} \exp\left(-\frac{\varepsilon^2}{\langle \varepsilon \rangle^2}\right) \quad (2.3)$$

where $\langle \varepsilon \rangle$ is some mean energy, determined by the gas properties. This solution tends to suppress the probability of higher and lower-energy electrons in favor of more intermediate values. Figure 2.1 compares the probability distributions from equations 2.2 and 2.3 for the same temperature T_α . The dotted line illustrates the average energy for the two distributions, which is not the same as the most probable energy.

Additional solutions of equation 2.1 in anything but these simple cases can be very challenging (c.f. Chapter 18 of [90]). Even computational approaches can be stymied by the seven-dimension phase space and high dynamic range. In most situations, the Boltzmann equation is reduced to more tenable expressions by integrating over velocity-space (leaving f as a function of space and time). The first so-called moment is the conservation equation or continuity equation [90],

$$\frac{\partial n_\alpha}{\partial t} + \nabla \cdot (n_\alpha \vec{u}_\alpha) = G_\alpha - L_\alpha. \quad (2.4)$$

In this case, there is now a mean velocity \vec{u} , as well as gain (G) and loss (L) terms which

replace the collision operator. The gain and loss terms are generally expressed as the product of the densities of the interacting species, and a rate coefficient. For an electron-impact interaction where the target is relatively stationary, the rate coefficient is

$$K = \int_0^\infty f_e(\varepsilon) \sigma(\varepsilon) \sqrt{\frac{2\varepsilon}{m_e}} d\varepsilon, \quad (2.5)$$

where σ is the energy-dependent cross section.

The definition of the mean velocity, \vec{u} can be obtained by multiplying equation 2.1 by v and integrating over velocity-space, to obtain the second moment [90],

$$m_\alpha n_\alpha \left[\frac{\partial \vec{u}_\alpha}{\partial t} + (\vec{u}_\alpha \cdot \nabla) \vec{u}_\alpha \right] = q_\alpha n_\alpha (\vec{E} + \vec{u}_\alpha \times \vec{B}) - \nabla \cdot \vec{\Pi} + \vec{f}_{\text{coll}}. \quad (2.6)$$

This expresses the conservation of momentum by the plasma. It provides a means by which to solve for the mean velocity of the system, however it also introduces two additional terms. \vec{f}_{coll} deals with the forces transferred to α via collisions. This is often approximated as the Krook collision operator, which is only dependent on known quantities: m , n , \vec{u} , G , L , and the momentum transfer frequency, ν_m , for the species α and all species it interacts with. The second term, $\vec{\Pi}$, is the pressure tensor and can only be defined by the third moment of the Boltzmann equation. In fact, each additional moment introduces a new term requiring a higher order moment, *ad infinitum*. In most situations, this chain of equations is terminated after the first two or three moments by the use of an additional assumption such as an equation of state. One common example of an equation of state is the isothermal relation, $p = nk_B T$, which can be used to remove the pressure tensor.

For the purposes of this paper, one more moment will suffice. Assuming that the pressure is isotropic, one can multiply equation 2.1 by $mv^2/2$, and integrate over velocity-space to find the energy conservation equation,

$$\frac{\partial}{\partial t} \left(\frac{3}{2} p_\alpha \right) + \nabla \cdot \frac{3}{2} (p_\alpha \vec{u}_\alpha) + p_\alpha \nabla \cdot \vec{u}_\alpha + \nabla \cdot \vec{q}_\alpha = \frac{\partial}{\partial t} \left(\frac{3}{2} p_\alpha \right) \Big|_{\text{coll}}. \quad (2.7)$$

In this case, p represents the isotropic pressure, and \vec{q} is the heat flow. The first term on the LHS represents the total energy contained by the species, the second term is the energy flux in and out of the volume, and the third term accounts for changes due to compression or expansion. The RHS is the collision operator which describes energy added or removed from the system as a result of collisions.

Equations 2.4 and 2.7 are particularly important for this study. As will be detailed in Chapter 5, the two can be used to create a global model of the plasma. Such a model assumes spatial homogeneity of the plasma in order to reduce the associated computational costs. This allows the model to address large numbers of species over long periods of time as will be required in the case of the RPND.

2.2 Plasma Criteria

Though the Boltzmann equation describes both an ionized gas and a plasma, the two are distinct as a plasma is necessarily an ionized gas, but not vice versa. A plasma is unique in that its dynamics are governed by long range electromagnetic forces, unlike gases in which short-range collisions dominate. As a result, plasmas frequently exhibit large scale structure and organization. Examples of these structures are ubiquitous in astronomy where phenomena such as the aurora borealis, coronal mass ejections, and even interstellar media are all plasmas [91]. There are three criteria which form a more exact definition of what constitutes a plasma.

2.2.1 Debye Length

If an electrical perturbation is introduced into an ionized gas, the charged particles will tend to rearrange themselves to shield it out. A plasma is an ionized gas which is large enough for this shielding effect to occur. The characteristic length scale for this shielding effect to take place is referred to as the Debye length, denoted λ_D . It can be shown to be equal to

$\sqrt{\epsilon_0 T_e / (en_0)}$, where ϵ_0 is the vacuum permittivity, T_e is the electron temperature, and n_0 is the plasma density. If the characteristic length scale of the ionized gas is L , then $\lambda_D < L$ for it to be considered a plasma.

2.2.2 Debye Sphere

However, the above condition by itself is not sufficient for shielding to occur. It is possible that an ionized gas may have a relatively small Debye length, but also lack enough charged particles for shielding to occur. More simply put, it would be impossible for a single electron to shield out even the smallest of perturbations. For that reason, the number of particles in a Debye sphere must be greater than unity in a plasma, or $n_0(4\pi\lambda_D^3/3) \gg 1$.¹

2.2.3 Plasma Oscillations

Finally, a plasma may exhibit Debye shielding, but lack the collective behavior of a plasma. This can occur when the collision frequency with neutral particles is too high. In this case, the behavior of the ionized gas would be determined more by the random collisions. Therefore, the characteristic response frequency of a plasma, commonly called the plasma frequency, must be greater than the neutral collision frequency, or $\omega_p > \nu$. The plasma frequency can be shown to be $\omega_p = \sqrt{e^2 n_0 / (\epsilon_0 m_e)}$.

There are many natural and man-made plasmas of varying size and quality. Figure 2.2 shows several categories of plasma, plotted as a function of their electron density and temperature. As can be seen in this example, the electron densities span seven decades, and the densities cover in excess of 20. This broad range of conditions presents a particularly challenging problem for both simulations and experimental measurements. Also highlighted in the figure is the range spanned by the RPND.

¹This condition is also implied in the derivation of the Debye length.

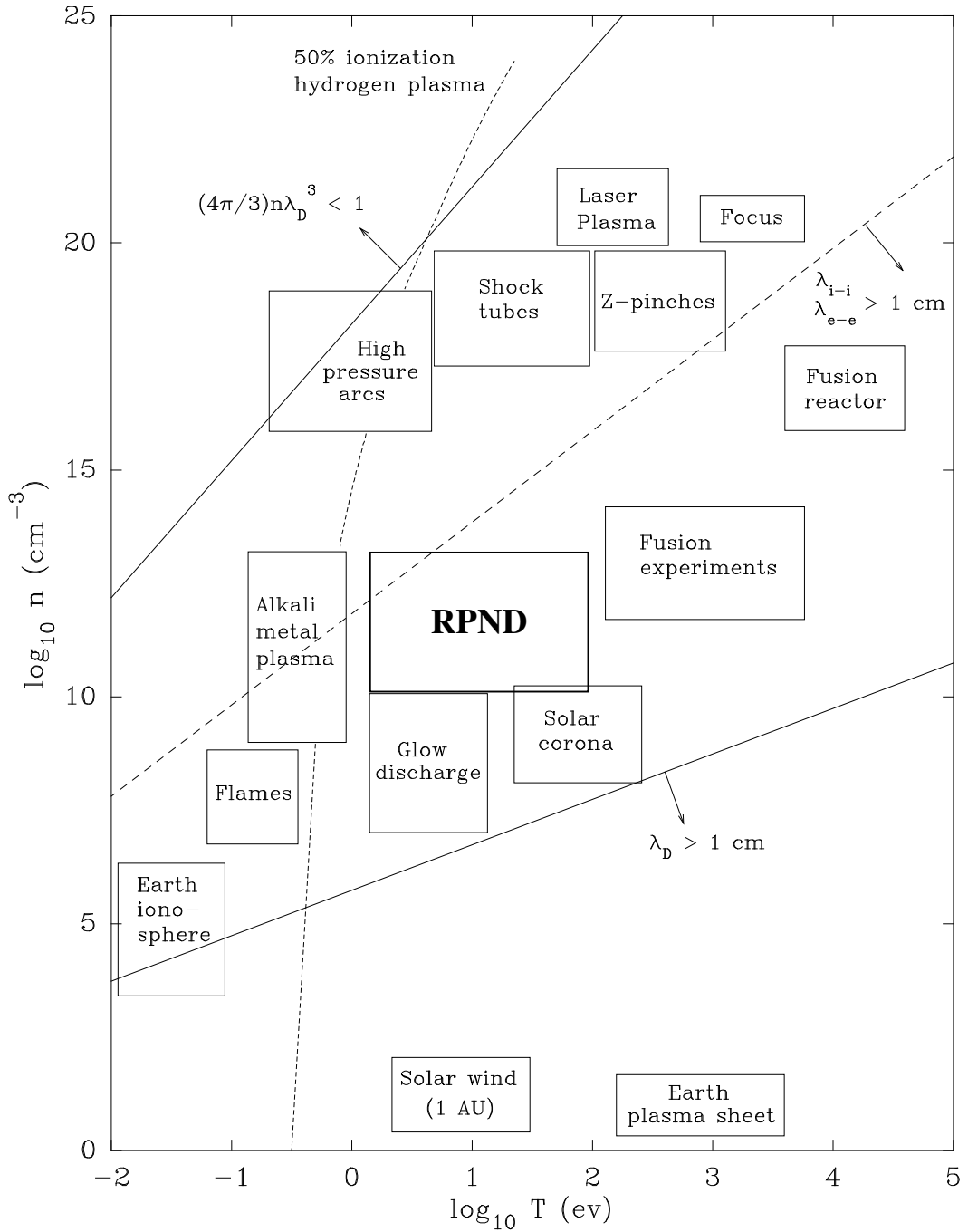


Figure 2.2: Illustration of the various regimes of plasma in terms of electron temperature and density with the RPND regime highlighted, adapted from [2].

2.3 Discharge Initiation

The Boltzmann equation is a continuous, statistical description of a plasma. By comparison, the initial breakdown of a plasma is a highly discontinuous process marked by its stochasticity. The initiation of a discharge is typically the result of electron avalanches which occur randomly throughout a volume of gas [89]. Often, the seed electrons for a plasma are the products of ionizing cosmic rays. At sea level this results in a few electrons per cubic-centimeter. As a result, it is necessary to consider the initiation of a discharge separately from a pre-existing plasma.

2.3.1 Townsend Mechanism

Classically, plasmas are created by two different mechanisms, the applicability of which depends on primarily on the strength of the electric field relative to the neutral gas density, a value called the reduced electric field [92]. At lower reduced fields, the Townsend mechanism is responsible for the formation of a plasma. Consider two electrodes separated by a gap filled with some gas. An electron starting near the cathode will drift toward the anode. For a large enough electric field, the electron will gain sufficient kinetic energy to ionize a neutral atom, producing a second electron. The two electrons are now accelerated by the field, instigating further ionization of the background gas. The population of electrons quickly grows, thus the process is referred to as an electron avalanche. Eventually, the avalanche electrons are collected at the anode.

In their wake are ions which slowly drift toward the cathode. As the ions impact the surface of the cathode, they occasionally cause a secondary electron to be emitted. This secondary electron initiates a new avalanche and helps to sustain the discharge. A steady state electric discharge occurs when the current of the ion collection at the cathode matches the current of the electron collection at the anode. The time scale of the Townsend discharge is usually determined by the positive ions, as their large mass results in slow drift velocities.

For an electric field of 50 V/cm at 200 mTorr, the drift velocity of a helium ion in helium is about 7×10^4 cm/s [93]. For a gap of 10 cm, this gives a drift time on the order of 10–4 s.

The Townsend mechanism is characterized by two parameters: α and γ , the first and second Townsend coefficients. α is the number of ionization events that occur per unit length, often expressed as a function of the reduced field [89]. The second Townsend coefficient is the probability that an ion impinging on the cathode produces a secondary electron. The values for γ can vary widely and depends on the type of ion, its energy, the cathode material, contamination of the surface, and many other factors. That said, typical values are around 0.01-0.1 [90].

2.3.2 Streamer Mechanism

In contrast, the streamer discharge which occurs for larger values of the reduced field does not depend on secondary emission. Additionally, streamer discharges can develop in time periods as short as 1 ns, much less than the time required for Townsend breakdown. In order to describe the streamer mechanism, again consider an electron between two electrodes, as seen in (a) of figure 2.3. As with the Townsend discharge, this electron initiates an avalanche which moves toward the anode. As the electrons travel toward the anode, they randomly collide and diffuse, leaving behind a cone of ions, as seen in part (b). However, the higher reduced field drastically increases α . This causes the space charge of the avalanche to create an electric field comparable to the one that is applied, slowing the propagation of the avalanche.

At this point the avalanche can be considered a streamer as it begins to increase its extent by several additional processes. The large internal fields of the avalanche can accelerate individual electrons and “inject” them in the direction of the anode [4]. In addition, as the excited atoms in the wake of the avalanche begin to radiate, they can cause photoionization throughout the volume. Photoelectrons generated close enough to the negative head, or positive tail of the streamer will initiate secondary avalanches which eventually connect

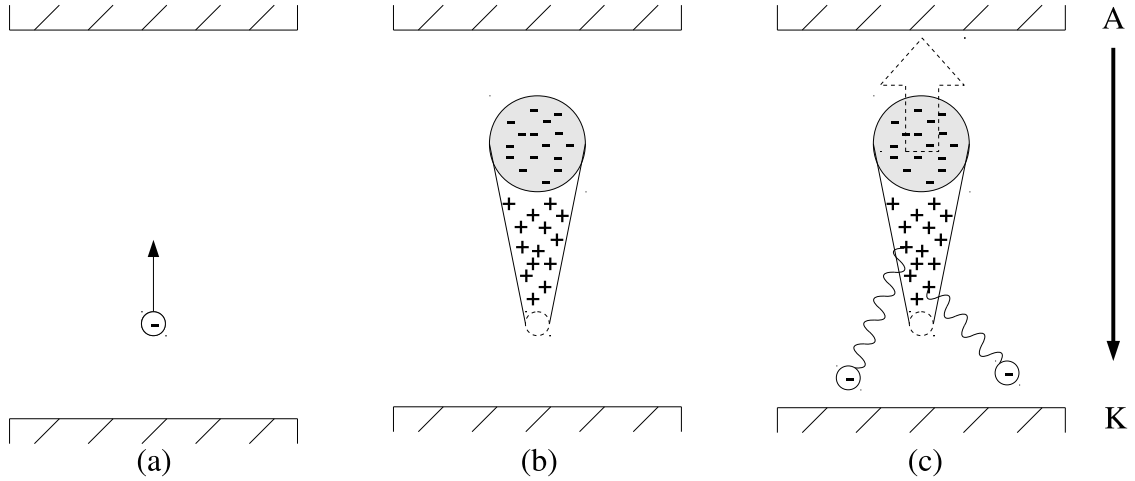


Figure 2.3: An illustration of the development of a single streamer. (a) A seed electron is accelerated by the applied electric field. (b) The initial electron develops into an avalanche which leaves a large region of positive space charge, slowing further advance. (c) The streamer propagates toward the cathode via photoionization and the anode via nonlocal electrons and photoionization. Adapted from [3] and [4].

to the primary one. While photoelectrons may cause some additional broadening of the streamer, the injection of electrons toward the anode is aligned with the direction of the internal field of the avalanche. As a result, the ionization caused by these electrons do not appreciably increase the radius of the streamer.

2.3.3 Homogeneity Condition

However, these processes are not critical in the formation of a large-volume discharge by an RPND. This description of a streamer only considers an avalanche generated by a single electron. In reality, many can form simultaneously assuming that there is more than one seed electron in the volume. With moderate preionization of the volume, the strong fields of the individual avalanches can begin to overlap². This smoothes out the field gradients which would otherwise radially constrict the streamers. Instead, ionization progresses homogeneously throughout the volume.

In order to determine the necessary preionization density, we refer to the work done by

²If the preionization of the volume is too large, it can effectively short out the electric field.

Levatter and Lin on gas laser discharges [3]. First, the electron drift velocity in an applied field can be expressed as the product of the field and the electron mobility μ . The electron mobility multiplied by the electric field is the steady-state drift velocity for an electron in that field and represents the balance between the frictional force of the neutral gas collisions and the electric field. Consequently, the mean velocity of electrons drifting in a time-varying field $E(t)$ can be expressed as

$$u(t) = \mu(E)E(t). \quad (2.8)$$

The length of the avalanche can be written as a time-integrated function of the electron drift velocity,

$$\xi = \int_{t_0}^t u(t)dt. \quad (2.9)$$

Here, t_0 is the time at which $E(t)$ becomes high enough that the first Townsend coefficient, α , exceeds 0. Because no electron multiplication occurs while $\alpha < 0$, this effectively represents the beginning of the avalanche.

The electric field in the head of the avalanche depends on its radius, which is dependent on the diffusion of the electrons as they cross the gap. This is governed by the free diffusion coefficient, D . For a fixed diffusion constant, the final avalanche radius would simply be $R = \sqrt{2D\Delta t}$, where Δt is the time after breakdown. As the diffusion coefficient typically varies with the applied electric field, the final avalanche radius will be assumed to be equal to $R = \sqrt{2\bar{D}\Delta t}$, where \bar{D} is the time-averaged diffusion coefficient.

Levatter and Lin assume that the avalanche slows when the peak field of the avalanche is equal to the applied field. Assuming that the electrons diffuse equally in all directions, the electric field of the avalanche head can be expressed as

$$E_a(r) = \frac{eN_e}{4\pi\epsilon_0 R^2} F(r/R), \quad \text{where} \quad (2.10)$$

$$F(r/R) = \frac{1}{R^2} \left[\operatorname{erf}(r/R) - \frac{2}{\pi^{1/2}} (r/R) \exp(-r^2/R^2) \right], \quad (2.11)$$

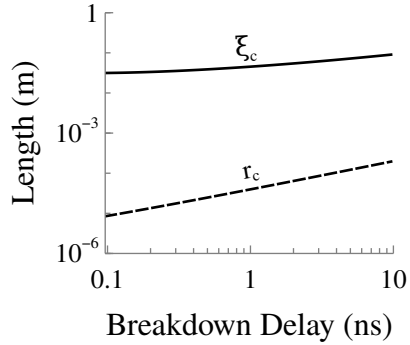


Figure 2.4: Numerical calculations of the avalanche length and avalanche radius for in helium at a pressure of 4.0 Torr as a function of the slope of the electric field, dE/dt .

where r is the radius with respect to the center of the avalanche, N_e is the number of electrons in the avalanche, erf is the error function. F is a dimensionless function which has a peak value of 0.428. Provided α as a function of reduced field, the number of electrons in the avalanche is equal to

$$N_e = \int_0^{\xi} \alpha(\xi') d\xi'. \quad (2.12)$$

Here, Levatter and Lin make a number of assumptions in order to develop an analytic and dimensionless solution for $E_{a,\max}(t) = E(t)$. However, it is possible to numerically integrate equations 2.9 and 2.12 to determine the time required for the avalanche to slow. This should provide a more accurate, but less general result. Assuming a linearly increasing electric field, figure 2.4 shows the results of such calculations for an avalanche in 4.0 Torr of helium, as a function of various breakdown delays. The breakdown delay is defined as the time it takes for $\alpha > 0$. The mobilities, diffusion coefficients, and Townsend coefficients were interpolated from solutions of the Boltzmann equation provided by the BOLSIG+ code with Phelps' cross sections [94]. For this range of breakdown delays, the avalanche was able to develop up to nearly 10 cm in length before it slowed. The times required for the avalanche to slow ranged from around 23 ns for the shortest breakdown delay, and 389 ns for the longest.

From this, a criteria for homogeneous breakdown of the gas can be developed. In order

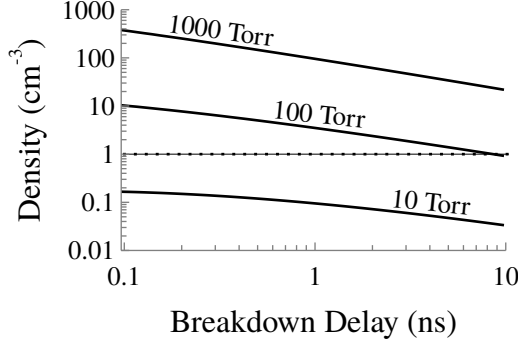


Figure 2.5: Minimum preionization densities required at a variety of pressures and breakdown delays. The dotted line indicates the background ionization level as a result of cosmic radiation.

for the field gradients to be smoothed out, the individual avalanche heads should roughly overlap by the time they have slowed. Assuming that all seed electrons in the volume initiate avalanches, this can be approximated as $n_{e,c} > r_c^{-3}$, where $n_{e,c}$ is the critical electron density, and r_c is the avalanche radius when it has slowed. As seen in figure 2.5, the required preionization density depends on both the breakdown delay and the operating pressure. Generally, the preionization density increases with pressure and decreases with breakdown delay. The dotted line in the figure indicates the anticipated background electron density from cosmic radiation. This suggests that, for the breakdown delays in question, the discharge will almost always be homogeneous at pressures below 100 Torr. While the plot suggests that large values of dE/dt might guarantee homogeneous breakdown at near-atmospheric pressure, the increasing likelihood of ionization instabilities [95] will preclude homogeneous discharge development.

2.4 Atomic Spectroscopy & Notation

As described, much of the experimental work presented will concern the use of spectroscopic techniques. Careful measurements of the light emitted from excited atomic states can yield electron densities and temperatures, excited state densities and temperatures, elec-

tric fields, and magnetic fields [96]. The topic of spectroscopy is extensive and it is neither necessary nor desirable to cover it in full. Instead we will only consider what is necessary to understand the emissions from a singly-excited, multi-electron atom.

An atom is composed of a small, positively charged nucleus, orbited by negatively charged electrons. The actual position of any single electron is probabilistic and described by a wavefunction—solutions of the Schrödinger equation for the atom in question. Each wavefunction is associated with a number of eigenvalues which quantize aspects of the state of bound electrons. In simple atoms, four such quantum numbers are of interest [97],

- $n = 1, 2, \dots$: the principal quantum number,
- $l = 0, 1, \dots, n - 1$: the orbital angular momentum number,
- $m_l = -l, \dots, l$: the projection of l , and
- $m_s = \pm 1/2$: the projection of the spin quantum number.

The quantum numbers are hierarchical such that each n , or shell, possesses a series of subshells, l , while each subshell possesses a number of individual orbital, m_l , and each orbital possess one of two spins. As a result of the Pauli exclusion principle, the wavefunction of each electron around an atom is described by a *unique* set of quantum numbers. This means, that any particular subshell can only contain $2(2l + 1)$ electrons. The subshells are often referred to using the nomenclature $0, 1, 2, 3, \dots = s, p, d, f, \dots$

As a result of their separation from the nucleus, the electrons in an atom possess some degree of potential energy. As the n and l of an electron increase, so does its potential energy. In the absence of electric and magnetic fields, m_l and s do not affect the potential energy of an electron. As an example, an electron in the $1s$ ($n = 1$ and $l = 0$) subshell has the lowest possible potential energy.

Absent from external influences, the individual states are populated with electrons so as to minimize the total potential energy of the system. This natural arrangement is referred to

as the ground state configuration. Often, but not always, the subshells are filled sequentially and in order from lowest to highest l [97]. Provided some input energy in the form of a collision or a photon, one or more of the electrons surrounding the atom may transition to another state, increasing the potential energy of the system. In low-temperature plasmas it usually one of the electrons from the outermost or partially filled subshell to be excited.

The potential energies of the electron configurations for multi-electron atoms are determined by the collective effects of all the surrounding electrons.

It is the collective effects of all electrons surrounding an atom which determine its potential energy. This results in a single set of total angular momenta which can be used to describe the atom. In lighter atoms [97], the contributions of the individual electrons are combined assuming a condition called L-S coupling. Under this assumption, the total angular momentum of the atom can written as $\vec{L} = \sum \vec{l}_i$, where i is each electron in a partially filled subshell (filled subshells sum to zero). Likewise, the total spin can be written as $\vec{S} = \sum \vec{s}_i$. These can be combined to form the total angular momentum of the atom, $\vec{J} = \vec{L} + \vec{S}$. Finally, the each atom is said to have an even or odd parity, defined as $(-1)^{\sum l_i}$, where -1 is odd, and 1 is even.

These quantities can be used to write a “term symbol” for the atom, of the form $^{2S+1}L_J^p$, where p is ‘o’ if the parity is odd, and omitted if it’s even. The term symbol can be augmented by prepending additional terms which address the subshells in which electrons can be found. This is typically written as nL^N , where N is the number of electrons in a given subshell (omitted if $N = 1$). For example, $1s2s^3S_1$, describes the triplet helium metastable state. In this case, there is a single electron in the 1s subshell and a second atom in the 2s subshell. The configuration has a total orbital angular momentum of 0 (denoted by the ‘S’), an even parity (denoted by the absence of a superscript ‘o’), a total spin of 1 (the superscript 3 is equal to $2S + 1$), and a total angular moment of 1.

Excited atomic states usually have finite lifetimes. Normally, electrons will undergo transitions to lower the potential energy of the system. This can also occur spontaneously,

through the emission of a photon, or through a superelastic collision with another particle. In the case of spontaneous transitions, only certain states can transition to others, as defined by a series of selection rules [97]:

- $\Delta S = 0$
- $\Delta L = \pm 1$ or 0
- $\Delta J = \pm 1$ or 0
- $L = 0$ cannot transition to $L = 0$
- $j = 0$ cannot transition to $J = 0$

These rules are determined from a lower order approximation, and thus are not strict. As a result, forbidden transitions can occur, however these generally take place at much lower rates.

Figure 2.6 is a Grotrian diagram of the energy levels in neutral helium and the allowed transitions. In this case, the atomic states are separated into the singlet ($S = 0$) and triplet ($S = 1$) manifolds. The singlet manifold is composed of excited states where the electron spins are anti-parallel, and the triplet manifold represents excited states where the electron spins are parallel. As indicated by the first selection rule, transitions between these two manifolds is forbidden, thus each is something of a self-contained system [98].

Also observable in the diagram are two “metastable” states. These are the 2s states at the bottom of the singlet and triplet manifolds. An electron in either state cannot spontaneously transition to a lower energy state. As a result, an electron in either state can be extremely long-lived. In addition, they are also the lowest-lying excited states of helium. For these reasons, helium plasmas tend to have high densities of metastable atoms. This makes them a good candidate for spectroscopic study as will be seen in Chapter 4.

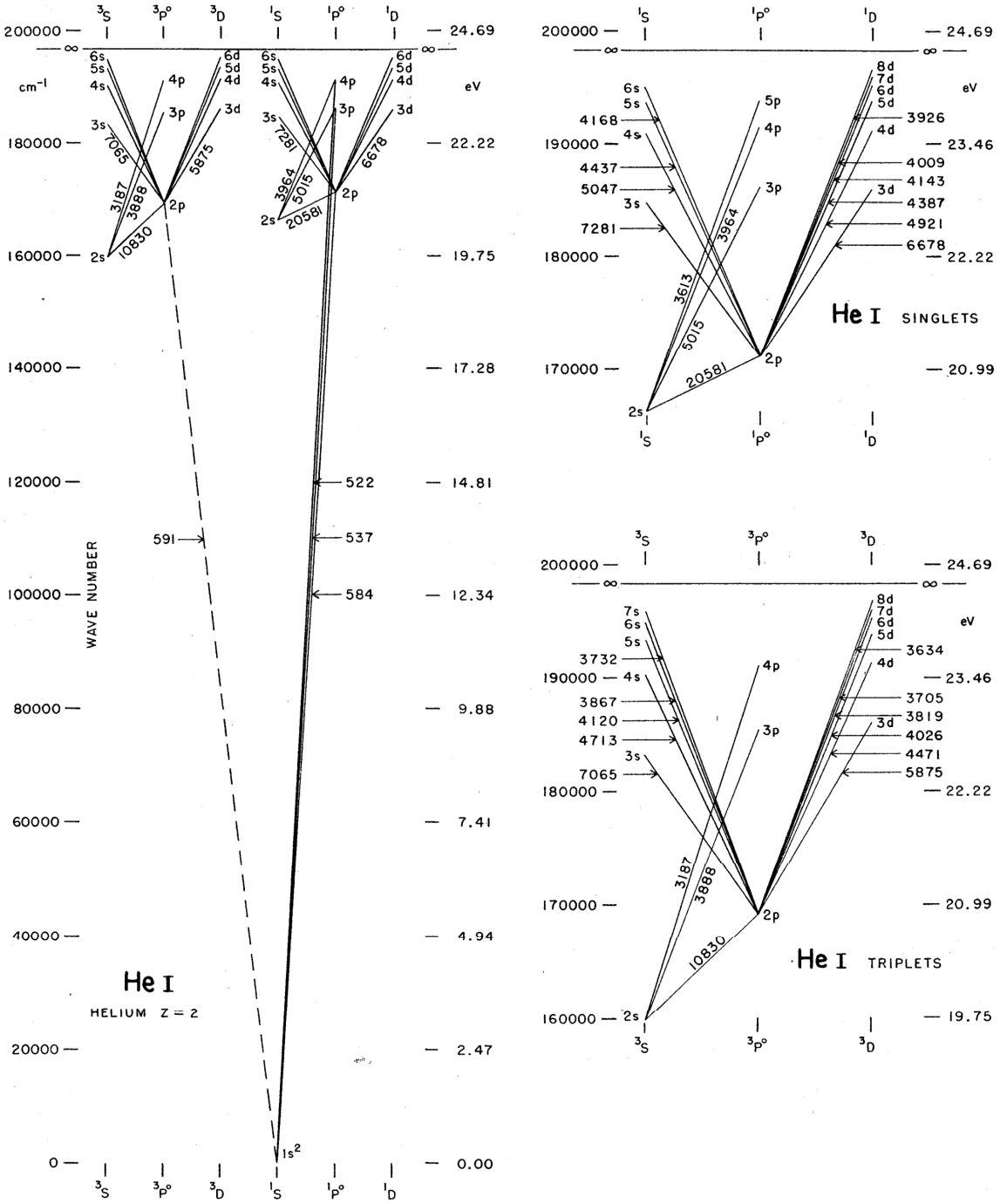


Figure 2.6: A partial Grotrian diagram of neutral helium, from [5].

2.4.1 Spectral Lineshapes

Electrons which transition to lower energy states emit photons which can be detected. Conversely, if an atom is exposed to a photon with an energy matching a transition, the atom may absorb the photon. Both processes are useful in determining the prevalence and dynamics of the excited states. This, in turn, can be used to infer various plasma properties.

Conservation of energy requires that the energy of the absorbed or emitted photon match the energy difference between the two states. However, the finite lifetime of excited atomic states implies, via the time-energy formulation of the uncertainty principle, some uncertainty in the actual energy difference between the states. As a result, the emitted photon will possess an energy selected from a distribution of energies.

This distribution is referred to as the spectral lineshape. The narrowest permissible lineshape, or natural lineshape, of an atomic transition can be shown [99] to be a Lorentzian of the form,

$$g(\omega) = -\frac{1}{4\pi^2} \frac{A\lambda^3}{\Delta\omega_a} \frac{1}{1 + [2(\omega - \omega_a)/\Delta\omega_a]^2}, \quad (2.13)$$

where ω is the photon frequency, A is the Einstein coefficient for the transition, λ is the wavelength of the transition, ω_a is central frequency of the transition, and $\Delta\omega_a$ the full-width half maximum (FWHM) of the transition. In the ideal case, where the atoms motionless and unaffected by external perturbations, $\Delta\omega_a = A$ [99]. This is known as the natural linewidth.

Other processes can act to broaden or alter the spectral lineshape [100]. For example, inter-atomic collisions can reduce the lifetimes of excited states. This results in additional broadening of the line, though it retains its Lorentzian nature. As the frequency of inter-atomic collisions increases linearly with pressure, this phenomena is referred to as pressure broadening. It can be included in equation 2.13 by using $\Delta\omega_a = A + BP$, where B is a measured or calculated broadening coefficient, and P is the pressure [99].

Atomic motion can also play a role in the spectral lineshape. If an atom is moving toward or away an observer as it emits a photon, the emitted photon will be blue or red

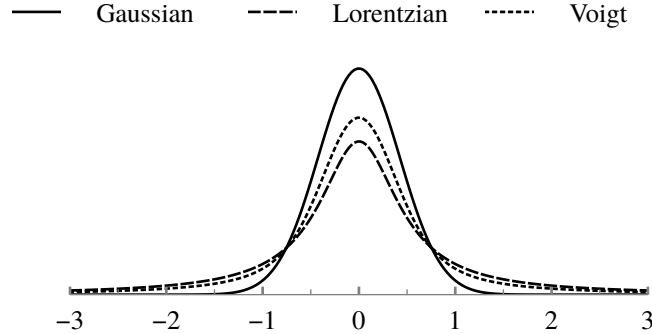


Figure 2.7: A comparison of the three primary spectral lineshapes, each with the same full width.

shifted. Likewise, if the atom is moving toward or away an incident photon, the energy of that photon will be shifted [99]. If this effect is averaged over the random motion of atoms in a gas, the result is an additional broadening of the lineshape, called Doppler broadening. Unlike pressure broadening, Doppler broadening introduces a Gaussian component to the lineshape such that,

$$g(\omega) = \sqrt{\frac{2 \ln 2}{\pi^3} \frac{\Delta\omega_a}{\Delta\omega_d}} \int_{-\infty}^{\infty} \frac{1}{[(\omega - \omega_a) - \omega']^2 + 4\Delta\omega_a^2} \times \exp \left[4 \ln 2 \left(\frac{\omega'}{\Delta\omega_d} \right)^2 \right] d\omega'. \quad (2.14)$$

Here, $\Delta\omega_d = \omega_a \sqrt{\frac{8k_B T_g \ln 2}{Mc^2}}$, is the width of the Doppler broadening, where T_g is the gas temperature, M is the particle mass, and c is the speed of light. This form of the spectral lineshape is known as the Voigt profile, and it must be numerically integrated. In the case that $\Delta\omega_d \gg \Delta\omega_a$, equation 2.14 can be simplified to a standard Gaussian distribution,

$$g(\omega) = \sqrt{\frac{4 \log 2}{\pi \Delta\omega_d^2}} \exp \left[-(4 \log 2) \left(\frac{\omega - \omega_a}{\Delta\omega_d} \right)^2 \right]. \quad (2.15)$$

The effect of the various broadening mechanisms is most apparent in the wings of the lineshape, far from the peak. Figure 2.7 illustrates the three major lineshapes with equiva-

lent full widths. The Voigt profile is composed of equally broad Lorentzian and Gaussian distributions. As can be seen, the wings of the Gaussian distribution fall off very quickly. In comparison, the Lorentzian component is observable well out to the edges of the figure.

The spectral lineshape can be altered by a number of other processes. Electric fields can influence the emissions via the Stark effect, while magnetic fields can split up degenerate states via the Zeeman effect. The fields of electrons and nearby molecules can also alter the lineshape of a transition. While not used in this study, such effects can be used as effective diagnostic tools in the measurement of field strengths, and charged particle densities in plasmas.

2.4.2 Absorption

As has been mentioned, a photon which closely matches the energy between two states can be absorbed by an atom. This property forms the basis for absorption spectroscopy where light with a known spectrum is used to illuminate a sample. The spectrum of the light that passes through the sample is measured and used to infer properties of the sample. In contrast to the emission processes occur spontaneously with a characteristic lifetime, often 10s of nanoseconds or more, absorption is almost instantaneous. This makes absorption-based spectroscopic methods desirable for fast phenomena, such as the RPND [101].

The cross section for a single atom to interact with a photon can be shown [99] to be,

$$\sigma(\omega) = A \frac{\lambda^2}{8\pi} \frac{g_1}{g_2} g(\omega). \quad (2.16)$$

where g_1 and g_2 are the number of degenerate configuration for the lower state and upper state respectively. $g(\omega)$ is the appropriate spectral lineshape, determined from the operating conditions.

It is important to recognize that absorption spectroscopy can also perturb the system it is measuring. Suppose two consecutive photons were incident on the atom. If the first was

absorbed, the likelihood that the second photon would be absorbed is zero. The cross section for absorption has not changed, there are simply no atoms available for the second photon to interact with. Therefore, if a photon field is incident on a volume of atoms susceptible to absorption, the degree to which the field is absorbed will depend on its intensity. The more intense the photon field is, the more it reduces the number of atoms available to interact with.

Eventually, this effect is balanced by a process called stimulated emission. In this process, an atom is already in an excited state with one or more lower states. If an photon is incident on the atom and matches the energy difference between its current state and a lower one, the photon may induce a transition to the lower state. This results in the emission of a second photon with the same energy and phase as the first. The cross section for stimulated emission is identical to that for photon absorption.

This feedback process where the absorption and emission processes balance with each other is known as saturation. The saturation of a volume of gas is a continuous process, and depends on the atomic states in question and areal density of the incident photons, or intensity. From a practical standpoint, absorption measurements require that the interrogating photon field remain below a threshold value. This saturation intensity can be shown [99] to be,

$$I_s = \frac{2\sqrt{2}h\nu_0 A}{\lambda^2}, \quad (2.17)$$

where h is Planck's constant, and ν_0 is the nominal frequency of the transition [99].

In this report, absorption and spontaneous emission diagnostics provide the experimental basis on which the RPND analyzed. Both are direct measures of the excited states that exist within a RPND. However, neither provides any direct measurement of the quantity or energies of the electrons. In the RPND, as with all plasmas, the electrons play a fundamental role in how the discharge behaves and develops. At the most basic level, it is the electrons which are accelerated by the electric field and collide with the gas atoms to produce the aforementioned excited states. Consequently, it should be possible for a sufficiently de-

tailed model to use measurements of the excited states in order to infer the properties of the electrons, as will be seen in Chapter 5.

CHAPTER 3

Experiment

3.1 Discharge Apparatus

The RPND apparatus used in the forthcoming experiments was similar in design to the coaxial geometry used by Vasilyak and others used in FIW studies [19]. As depicted in figure 3.1, it is essentially a cylindrical inner conductor, surrounded by a dielectric, covered by an outer conductor. An electrode, connected to the transmission line, and the RPND serve as the inner conductor. The dielectric took the form of a glass tube and an air gap. Finally, the outer conductor consisted of a series electrically connected metal shells which served as the current return path. Following from right to left, the inner conductor was composed of a vacuum window, a nipple, a double-sided flange tapped for an NPT connection, and the discharge tube containing the RPND. Unless otherwise noted, all vacuum components featured DN35 CF flanges with copper gaskets.

The tube was composed of borosilicate glass with metal vacuum flanges on both ends. The flanges of the tube also acted as the electrodes for the generation of the RPND. The glass tube had an inner diameter of 3.3 cm, an outer diameter of 4.0 cm, and a length of 22.9 cm. The overall length of the tube including the flanges was 30 cm. In the figure shown here, the right electrode served as the anode, and the left electrode was the cathode.

The dielectric surrounding the inner conductor was composed of several components. The vacuum window, nipple, double-sided flange, and anode were separated from the outer

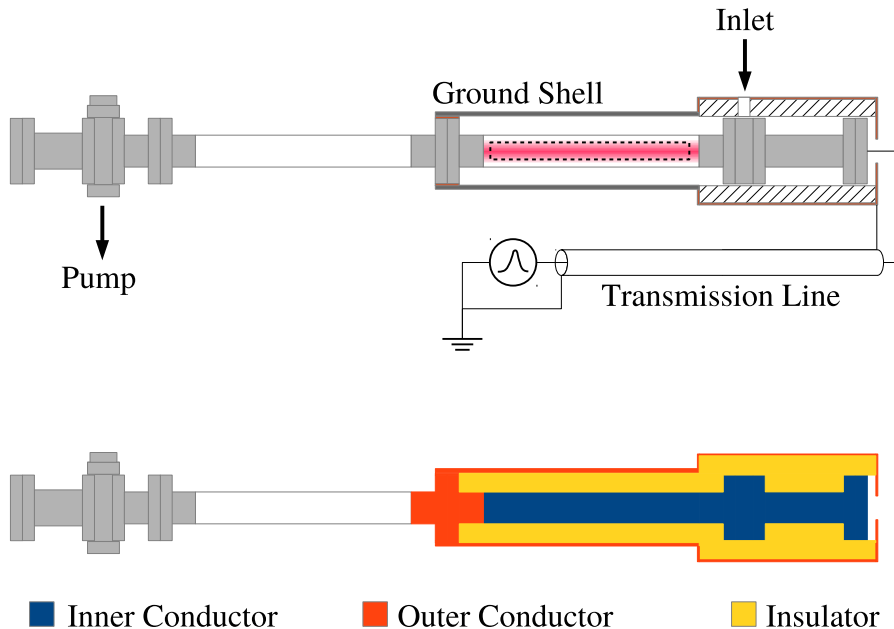


Figure 3.1: Two illustrations of the RPND apparatus. The upper version is an annotated sketch of the device, and the bottom version simplifies the geometry into its three electrical components.

conductor by an air gap and a polytetrafluoroethylene (PTFE) tube, 20 cm in length with an inner diameter of about 7.5 cm, and an outer diameter of 10 cm. The RPND portion of the inner conductor was separated from the outer conductor by the glass tube and an air gap of about 2.54 cm.

The left side of the discharge tube, or cathode, connected to the outer conductor and served as part of the current return path. Directly attached to the cathode was an aluminum tube, held in place by an acetyl resin shaft collar and a copper shim. Radial optical access to the discharge was provided by two slots milled into the ground shell. The slots were positioned on opposite sides of the shell and were 3.8 by 25.4 cm in length. The tube itself was 30 cm in length.

The end of the aluminum tube nearest the anode was affixed to a copper sheet which was oriented perpendicular with respect to the tube's axis of rotation. The sheet was 10 cm square, and was attached to the tube with conductive copper tape. A 5 cm diameter

hole was cut into the copper sheet to allow the discharge tube to pass through it. The sheet was secured to the edge of the PTFE tube by nylon screws. Surrounding the PTFE tube was a second shell, made of rolled copper sheet. This was electrically connected to the aluminum tube by a braided copper strap. The right end of the PTFE tube was covered by a second copper sheet, 10 cm square. Again, the sheet was secured to the PTFE tube by nylon screws and in electrical contact with the copper shell. In the center of the copper sheet was a HN bulkhead adapter for connection to the transmission line. The inner conductor of the bulkhead adapter was connected by a straight run of 5 cm of silicone-coated wire to the vacuum window flange. The outer conductor of the bulkhead adapter provided the ground connection for the discharge apparatus.¹

The voltage pulse was generated by a FID power supply, supplied by ANVS, Inc. (model PT510NM). The amplitude of each pulse was fixed at 6.4 kV with a repetition rate of 1.0 kHz. Each pulse had a fixed width of 25 ns, required approximately 4 ns to rise from 10% of its peak to 90% of its peak, and was roughly Gaussian in shape. A SRS DG645 delay generator was used to trigger the power supply output for all experiments and provided a reference time base for all measurements.

Preliminary experiments revealed multiple reflections between the power supply and the anode. A long run of RG 213 coaxial cable was used to temporally separate the reflections. This made it possible to study the effects of individual pulses. Based on the length of the cable (about 13.7 m), the delay was predicted to be 69.2 ns. As the reflection would have to cross the length of the transmission line twice before it reached the anode again, the total separation time between the initial pulse and each subsequent reflection was predicted to be 138.4 ns. This calculated delay was found to closely match the measured time period between the incident and reflected pulse.

A simplified version of the gas flow system can be seen in figure 3.2. The gas supply

¹Measurements confirmed that the entirety of the outer conductor had a low DC impedance to ground. However, it is likely that at frequencies relevant to the RPND, the impedance is not negligible. As a result, the outer conductor likely floats to a finite voltage during operation.

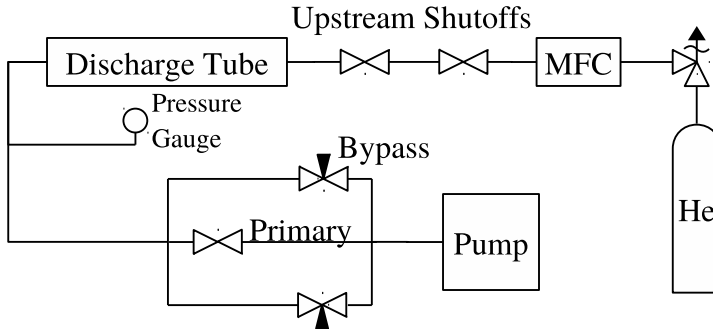


Figure 3.2: Simplified diagram of the gas flow path and pumping system.

was provided by a bottle of ultra-high purity helium. Following the regulator, the helium passed through a digital flow controller which was set at 25.0 sccm for all experiments. The helium then entered a gas distribution manifold, followed by a shutoff valve, a short run of 1/4" stainless steel tubing, another shutoff valve, about 2 m of 1/4" polyethylene tubing, and then the discharge tube via the double-sided flange.

The gas exited the discharge tube via an identical tube, on the side opposite the inlet, see figure 3.1. This second tube was intended to electrically isolate the discharge portion of the apparatus so that only a single conductive path to ground existed. The pressure was monitored downstream of the second tube with two capacitance manometers (one with a full scale range of 10 Torr, the other with a range of 100 Torr). The gas exhaust of the second tube was connected to an oil-seal roughing pump via three independent paths. The primary pump path had the highest gas conductance and was controlled by a bellows valve. However, this path was typically closed in favor of two needle valve bypasses. The needle valves were used to control the pumping speed and obtain the desired operating pressure. Immediately upstream of the roughing pump was a zeolite trap in order to limit oil backstreaming.

The base pressure of the system was measured to be approximately 15 mTorr. The leak rate was measured several times by evacuating the apparatus and then sealing it from the pump by all three pump paths. The leak rate was found to be 2.0×10^{-3} sccm. Given a constant flow rate of 25.0 sccm, the fractional impurity can be conservatively estimated to be 80 ppm.

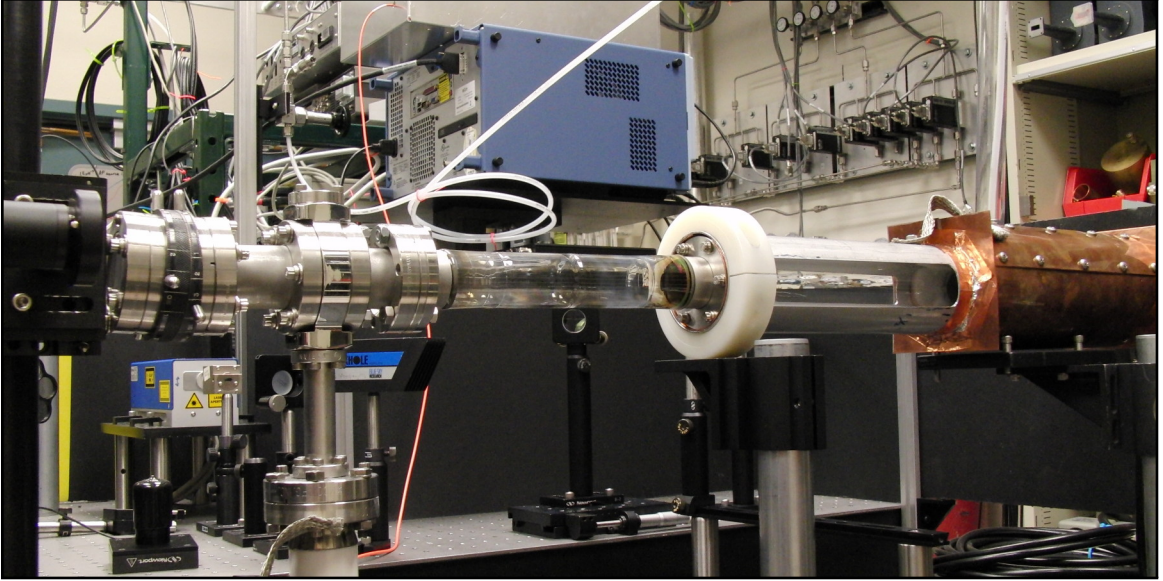


Figure 3.3: Photograph of the discharge apparatus.

The assembled discharge apparatus can be seen in figure 3.3. The RPND apparatus was supported two 1.5 in mounting posts with angle brackets. The mounting posts attached to a 122 cm by 76 cm optical breadboard, supported by urethane shock absorbers, and a rigid frame. The roughing pump was attached to the apparatus with flanged bellows in order to reduce mechanical vibrations.

All electrical measurements were made with a LeCroy 6100A WaveRunner oscilloscope which had a bandwidth of 1.0 GHz. Electrical connections to the oscilloscope were made with RG 50/U coaxial cable and standard BNC connectors. All connections were terminated at 50Ω unless otherwise noted. The voltage of the pulses was monitored from a 1 : 1000 divider built into the power supply. The current was measured from a current shunt which crossed a small electrical break in the outer conductor of the transmission line. The shunt was built into the transmission line as close as possible to the power supply, about 3 cm from the output connector.

The current shunt was composed of nine, low inductance, 1.0Ω resistors connected in parallel. As illustrated in figure 3.4 the resistors were soldered to two strips of copper foil. This assembly was then wrapped around the electrical break in the transmission line, brid-

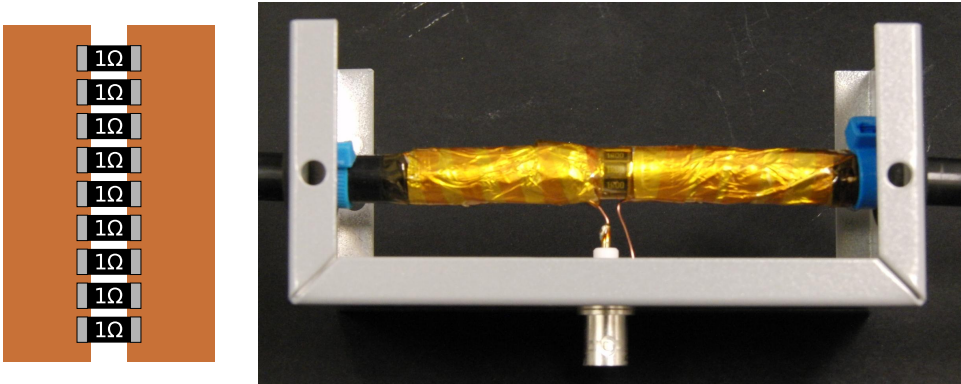


Figure 3.4: Sketch of the unassembled back-current shunt, and a photograph of it assembled around the transmission line.

ing it. Two short lengths of No. 18 copper wire were soldered to each side of the shunt assembly. These were then attached to a BNC bulkhead connector, fitted to a metal project box. The voltage across the resistors was used to measure the current traveling through the outer conductor of the transmission line. The copper foil was then secured to the outer conductor with several wraps of aluminum foil, followed by a layer of polyimide tape.

Data were retrieved from the oscilloscope with a desktop computer via the GPIB interface. Instrument control, data acquisition, and data storage were all managed by a LabView program. Analog input and output was handled with the auxiliary input and output ports of a SRS SR850 DSP lock-in amplifier.

3.2 Field Calculations

The electric field characteristics of the discharge apparatus were analyzed using Ansoft Maxwell 9, a two-dimensional, electrostatic solver. At the top of figure 3.5 is a logarithmic heatmap of the electric field magnitudes within the device. Overlaid are the electric field vectors in magenta. Below this is a plot of the electric field on a linear scale, across the central axis of the apparatus and along the outer edge, adjacent to the glass tube. It is apparent that the field strength is the strongest at the triple point which occurs near the glass-metal seal. Also noticeable is the fast fall off of the electric field with distance from the anode.

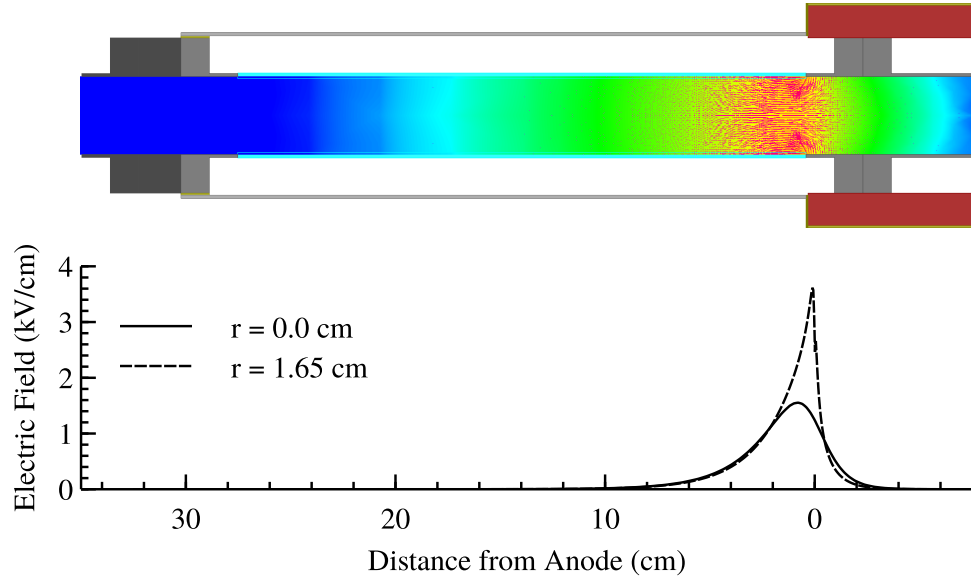


Figure 3.5: Heatmap and vector plot of the electric field in the RPND discharge apparatus.

The presence of the external ground shield produces an electric field contour vastly different from that of two parallel plates. This is also reflected in the electric field vectors. Specifically, the many locations possess fields with strong radial components, especially those near the anode.

These static fields are only valid in the absence of free charge within the system. However, these characteristics suggest that the discharge formation will be somewhat different than the one-dimensional description of a streamer in Chapter 2. First, assume that the electrons are distributed uniformly throughout the discharge tube, prior to the pulse. As a pulse is applied, ionization would preferentially take place near the anode. As the electrons would be drawn toward the anode, and leave behind some amount of positive space charge. However, as the positive space charge builds up, it would begin to act as a virtual anode, increasing the electric field further from the physical anode. The virtual anode would then begin to draw its own electron current, predominantly from around the edges, near the wall. In this manner, the discharge would propagate away from the anode, leaving a quasineutral ionized gas in the center of the discharge tube and a positive space charge region along the wall.

3.3 Operating Procedures

One of two operating procedures for the RPND was used depending on how recently the discharge had last been turned on. If the discharge was inactive for over one hour, then a full startup procedure was used. Otherwise, an abbreviated process was used.

In the case that the discharge had not been operated for over an hour, the roughing pump was turned on and the primary pump path valve was opened as was the first shutoff valve upstream of the discharge chamber, seen in figure 3.2. The system was then allowed to pump down to its base pressure. Afterward the second upstream shutoff valve was opened and the system was again allowed to reach base pressure. At this point the helium flow was turned on and set to 25.0 sccm. The primary pump path was then closed and the needle valve bypasses were used to adjust the system pressure to 3.0 Torr.

Next, the delay generator was turned on and the output for triggering the power supply was activated. Then, the FID power supply was turned on. This would produce an easily visible discharge within the discharge tube. The system was allowed to operate at this condition for one hour in order to remove potential contamination on the walls and electrodes. At the end of this period, the voltage waveform was checked to ensure that it was consistent with previous experiments. Once this was confirmed, the pressure was adjusted to the desired operating condition.

The discharge was shutdown by first shutting off the power supply, followed by the delay generator. Then, the helium flow was shut off, and the primary pump path was opened. The system was allowed to come to base pressure before the two upstream shutoff valves were closed, after which the primary pump path was closed. The roughing pump was then shut off.

In the cases that the discharge had been operated within the last hour, it was possible to use an abbreviated startup procedure. This process was fundamentally the same as the previous one, however once the pump-related procedures were complete the discharge only required five minutes to reach a steady state. This was verified with multiple measurements

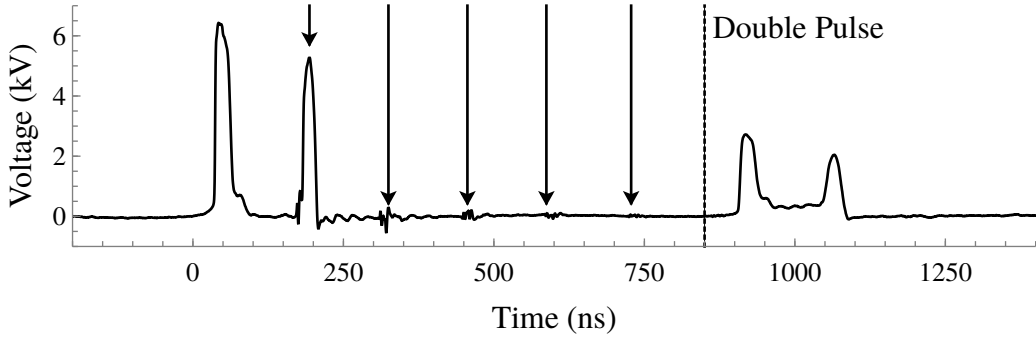


Figure 3.6: Typical voltage waveform of the RPND. Arrows indicate reflections back to the power supply. The dotted line delineates the time at which the power supply begins to exhibit double pulsing.

of the current and voltage characteristics as well as the discharge emissions. At times prior to this five minute equilibration period, the reflected pulse energy was noticeably higher, and the delay between the trigger pulse and the output pulse was variable.

It seems likely that the increased reflected pulse energy during the equilibration period is due to poor matching between the output impedance of the power supply and the plasma load [62]. When the pulse train is initiated, the first series of pulses perceive an almost open load. During this time, the plasma density tends to increase more with each pulse than is lost between pulses. This increase in plasma density, reduces its impedance and improves energy coupling to the plasma. At the same time, the increasing plasma density results in an increasing shielding effect of the applied voltage. Eventually, these effects balance out and the density increased caused by each pulse equals the density decrease which occurs between pulses. At this point the energy coupled into the plasma with each pulsed remains essentially fixed.

3.4 Electrical Characteristics

The typical voltage waveform, as seen in figure 3.6, exhibited a number of features. It begins with an incident pulse at $t = 0.0$. 138 ns later, it is followed by the pulse that has

been reflected from the anode. The reflected pulse is somewhat smaller, proportional to the energy deposited in the discharge. Additional reflections are visible at integer multiples of 138 ns. These subsequent reflections are much smaller than the initial one, suggesting that much of the remaining pulse energy was dissipated after the first reflection reached the anode. Curiously, a second pulse appears at 800 ns. This is believed to be a peculiarity of the power supply. For the most part, analysis of the RPND will focus on the times which precede 280 ns (the incident pulse and first reflected pulse).

The properties of the RPND were examined at: 0.3, 0.5, 1.0, 2.0, 3.0, 4.0, 8.0, and 16.0 Torr. The appearance of the discharge varied with the pressure in a continuous fashion, however it was apparent that there were three regimes of operation. At the low pressures, 0.3 and 0.5, it was difficult to initiate the discharge. Often, it would be necessary to increase the pressure to initiate the discharge, and then reduce the pressure to the desired conditions. The discharge appeared dim and relatively constricted about the central axis of the discharge tube, with a radial extent of approximately 1 cm. Accompanying these pressures was a large degree of electronic noise. This manifested primarily in the current waveforms, as seen in figure 3.7, as well as a number of equipment malfunctions.

As the pressure was increased (from 1.0-4.0 Torr), the electrical noise was observed to subside. The current waveforms showed significant reductions in the ringing that was particularly prominent at lower pressures. In addition, the visual extent of the discharge increased substantially, to the point where it could be considered volume-filling. The discharge also increased its axial extent as well, eventually reaching well past its intended limit at the cathode. This occurred despite attempts to isolate the downstream pump sections from the discharge.

Such behavior is similar to that observed in plasma bullets [83] where the discharge is able to continue far past the cathode. This suggests that development of the RPND along the discharge tube led by a large region of positive space charge, as suggested in the discussion of the field characteristics. The ions that produce this positive space charge are eventually

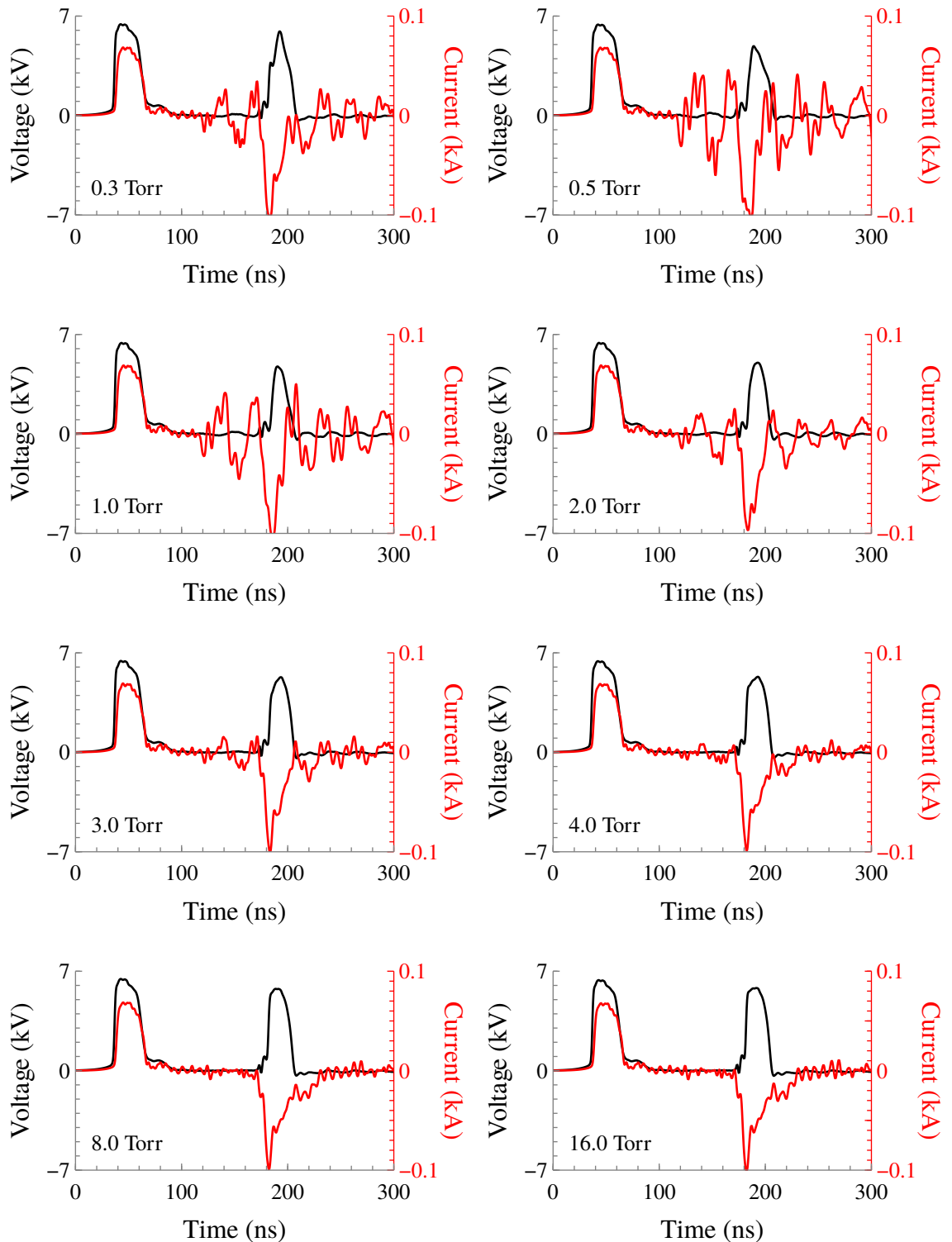


Figure 3.7: High resolution views of the voltage and current waveforms for the first incident and reflected pulse, at each of the operating pressures.

collected at the cathode or neutralized at the walls, however their low mobility (as noted in Chapter 2) prevents this from happening on time scales relevant to the RPND formation.

At higher operating pressure (8.0 and 16.0 Torr), the discharge receded back toward the cathode. This was accompanied by a decrease in the apparent brightness of the discharge to levels similar to that of the low pressure conditions. In contrast, the discharge appeared to remain volume-filling. While discharge initiation was difficult at the higher pressures, it was not accompanied by the electrical noise observed at lower pressures.

3.5 Energy Coupling

The product of the voltage and current waveforms, as seen in figure 3.7, gives the power deposited in the discharge as a function of time. Subsequently, the power integrated over time gives the total energy deposited in the discharge. However, this approach is somewhat complicated by several features of the RPND. As previously mentioned, the pulses produced by the power supply are not completely absorbed by the discharge. Therefore, the integration must be carried out over both the incident and the reflected pulse. Additionally, there is the concern that the oscillations in the current measurements could introduce fluctuations in the calculated energy deposition. However, the small voltage signal limits the error introduced by these fluctuations to less than 1%.

Figure 3.8 gives the total energy deposited for the first pulse at each of the operating conditions. The energy coupled to the discharge peaks at an energy of 5.5 mJ (out of a total incident energy of 8.8 mJ) at a pressure of 1.0 Torr, after which it slowly decreases. This peak in the coupled energy is coincident with the peak brightness of the discharge. Together, these suggest that the density of excited states will be optimized at intermediate pressures.

Though there appear to be no direct comparisons available in the literature, several papers report on energy coupling for similar systems. Macheret, Schneider, and Murray studied a parallel plate RPND in air, at 1-10 Torr and reported a total energy deposition of

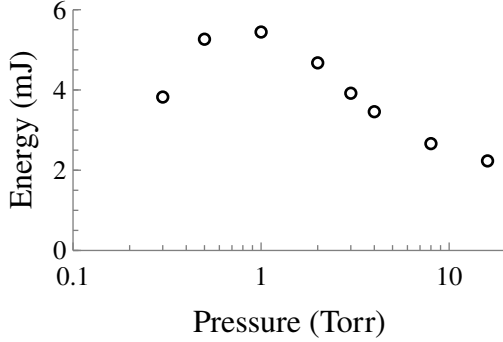


Figure 3.8: Plot of the energy coupled into the discharge with the first pulse as a function of pressure.

0.30-0.36 mJ, increasing with pressure [81]. Nishihara et al. recorded values of 1-2 mJ in a nitrogen RPND [72]. Pancheshnyi et al., in the study of an air-propane mixture at 750 Torr, found that each pulse deposited about 1.9 mJ of energy. Overall, the measured values for the deposited energy appear to be in comparable with those previously measured.

From an applications standpoint, the potential existence of a condition which optimizes the production of excited states is an interesting one. This behavior is also compelling from a physical standpoint as it suggests a phase change in the competition of two or more processes. Though this kind of competition is reminiscent of Paschen's law, the duration of the pulse is too short for appreciable ion drift to occur (an estimated maximum of 3 mm), therefore secondary electron emission is not important. These observations provide further impetus for a close examination of the RPND properties, particularly the excited state dynamics.

CHAPTER 4

Metastable Measurements

As was noted in Chapter 1, measurements of the RPND have been mostly limited to the afterglow plasma or time-integrated quantities. Electric field measurements, either with capacitive probes or nonlinear wave-mixing, thus far provide the only insight on the development of the RPND [79, 80, 87]. Though the electric field can be used to estimate electron densities and reaction rates in the plasma, this requires a number of additional assumptions regarding electron locality, and equilibrium with the applied field.

As a result, there is a lack of reliable information on particle properties of the RPND during its development. That said, such information is necessary to confirm the present understanding of how these discharges develop, how they may be optimized for specific applications, and how to improve existing numerical simulations. Therefore, a clear need exists for direct measurements of the RPND particle properties.

Unfortunately, this presents a significant challenge for most traditional plasma diagnostics. In most situations, the obvious choice would be the Langmuir probe given its simplicity and ease of implementation. However, the fast variations in the plasma potential, slow response of the ions, and high collisionality all preclude this approach [90]. Furthermore, any physical probe could potentially act as a large perturbation to the very system it is measuring.

The logical alternative to physical probes is the use of optical diagnostics, however these have their own associated difficulties. Electrons cannot be studied by their light emissions because, with the exception of bremsstrahlung and cyclotron radiation, they do not emit.

This leaves the light emitted from excited atoms. Atomic emission spectroscopy can be used to measure many different plasma quantities, from electron density, to local electric field strength [96]. Unfortunately, spontaneous emission can be a slow process compared to the development of the RPND. For example, the fastest neutral helium transition in visible wavelengths (3^3D_3 - 2^3P_2) has a decay rate of 14 ns [102].

This suggests that instead of waiting for spontaneous emission to occur, it may be better to use some form of active spectroscopy. Though the added complexity of a well-characterized light source is undesirable, it allows for several interesting opportunities. For example, a sufficiently intense laser can be used to directly interact with the electrons through Thomson scattering. It has a high spatial and temporal resolution and is able to measure the electron density and temperature simultaneously [103]. However, the RPND may have densities well below the interaction limit of $5 \times 10^{12} \text{ cm}^{-3}$ [75].

If it is not possible to directly interact with the electrons, the next alternative is interact with the atomic population. Probing of the ground state is difficult given its large separation from any excited state. Furthermore, the high densities of the neutral states would completely absorb all incident radiation, even over short pathlengths (leaving nothing to measure). Instead it makes more sense to probe an excited atomic state. The lowest lying one is the triplet metastable (2^3S), which resides at 19.82 eV above ground [102]. This relatively large energy gap assures that no such states will be naturally present at room temperature. The triplet metastable (and all higher-energy states in helium) will be populated almost exclusively by energetic electrons. Therefore, the triplet metastable density is a useful indicator of the electron energetics in the RPND as it develops. With a sufficiently complex model, it may even be used to infer properties of the electron population.

Perhaps the most straightforward means by which to measure the triplet metastable density is with absorption spectroscopy. This approach has a long history in the study of gas discharges, going back at least six decades [104]. At its most basic, the technique involves illuminating a plasma with light matching a transition between the metastable, and some

upper level. The amount of transmitted light is then measured with a detector on the opposite side of the plasma. The amount of transmitted light is proportional to the metastable density, integrated along the path of the light. As the temporal bandwidth of this technique is only limited by the time required for the light to traverse the plasma, it presents a promising approach for particle measurements during the development of the RPND.

4.1 Setup

Traditionally, the light used in absorption spectroscopy has been supplied by discharge tubes of same gas as the system under study. Though straightforward, this approach is limited by the luminosity of the discharge tube, and the fact that the emitted radiation is isotropic. More recently, Millard et al. noted that diode lasers provide a greatly improved light source for absorption experiments [105]. The laser light is easily directed and collimated for spatial selectivity, and has more than sufficient intensity [105]. Therefore, it was decided to use a diode laser in the measurement of the triplet metastable level.

As with the study by Millard et al., the decision was made to study the transition from the triplet metastable to the $2^3P_{0,1,2}^o$ state (a transition wavelength of approximately 1083 nm). This was done for several reasons. For one, the closest helium transition is over 7 nm away, making it relatively isolated. In addition, the different levels or values of J are all within the tuning range of a single diode. As each level has a different degeneracy, g , the strength of absorption varies depending on the selected level. Thus, the absorption strength can be increased for low densities, or decreased at high densities, improving the dynamic range of the diagnostic.

The laser used was a distributed feedback laser diode, produced by Toptica, model LD-1083-0070-DFB-1. The specified linewidth of the laser was 3 MHz, well below the natural linewidth of the transition at 10.2 MHz. This can be exploited to directly measure the gas temperature of the system, as will be seen in the next section. The diode was rated for a total

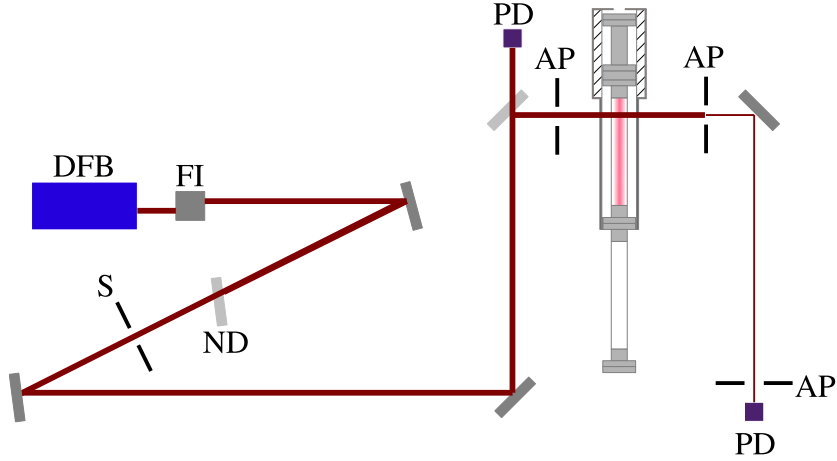


Figure 4.1: Optical beam path of the laser in the absorption spectroscopy experiment. DFB - Distributed feedback laser diode; FI - Faraday isolator; ND - neutral density filter; S - shutter; PD - photodiode; AP - aperture.

output power of 70 mW, with a beam size of 1 mm by 3 mm and vertical polarization. The diode was housed in a Toptica DL DFB housing which incorporated the collimating optics. A Toptica DCC 110 was used to provide current control for the diode laser, and a Toptica DTC 110 was used to control the thermoelectric cooler for the diode.

The layout in figure 4.1 reflects the optical beam path used in the absorption experiment. The laser light is produced by the distributed feedback laser diode (DFB). It then enters an Electro-Optics Technology, Inc. Faraday isolator (FI) which prevents back-reflections from entering the diode. Without the isolator in place, such back-reflections can cause mode-hopping, resulting in unreliable tuning. The laser intensity is then reduced by a neutral density filter (ND). After which, the laser passes through a Vincent Associates electronic shutter (S). Then, the beam is split by a Thorlabs BSF10-C beam sampler at a 45° angle. This reduced the laser intensity below the saturation intensity (0.45 mW/cm^2) of the transition. The beam was collimated with two apertures (AP) on both sides of the discharge apparatus. The beam exiting the apparatus was then sent through a final aperture to filter nearly-colinear plasma emissions before it was coupled into an optical fiber by a Thorlabs F240SMA-780 collimation package.

Behind the beam sampler was a Thorlabs DET300 germanium photodiode. The signal from this photodiode was terminated at $1\text{ M}\Omega$ and used to monitor the beam. The opposite end of the optical fiber was affixed to a Thorlabs DET410 InGaAs photodiode. The photodiode signal was amplified by a Femto HVA-200M-40-B voltage amplifier before being sent to the oscilloscope. The time resolution of the metastable measurements was determined by the InGaAs photodiode which had a specified rise time of 5 ns.

In order to measure the absorption of the laser, it was first necessary to tune the laser to the correct wavelength. This matter was complicated by the lack of a wavemeter with sufficient precision and accuracy. As a result, a signal generator was used to sweep the laser current so as to cover a frequency range of 40 GHz while the plasma was operating. The temperature of the diode was then slowly adjusted until absorption peaks corresponding to the $2^3S_1 - 2^3P_{0,1,2}^0$ transition were observed in the output of the InGaAs photodiode. This allowed the laser current to be tuned to coincide with the desired transition and provided a rough conversion between changes in the diode current and changes in the laser wavelength. A more accurate measurement of this relation was made with a CVI Melles Griot ET-25.4-10.00-30, solid dielectric etalon. It was found that a temperature of 36° C and a current of 63 mA produced resulted in an output wavelength of approximately 1082.9 nm and the conversion between diode current and wavelength was 0.6067 mA/GHz.

As described in Chapter 3, data acquisition was handled by a LabView program, connected to the oscilloscope by a GPIB cable. The auxiliary outputs of the SRS SR850 lock-in amplifier were used to adjust the diode laser current (via the DCC 110 module), and to trigger the electronic shutter. One of the auxiliary inputs of the lock-in amplifier was used to read out the pressure from the pressure controller.

Data were acquired for a range of pressures from 0.3-16.0 Torr, and at three axial locations: 5.08, 12.7, and 20.32 cm, relative to the glass-metal seal of the anode. In reference to their location relative to the gas inlet these will be referred to as the ‘upstream’, ‘midstream’, and ‘downstream’ locations, respectively. For each combination of location and pressure,

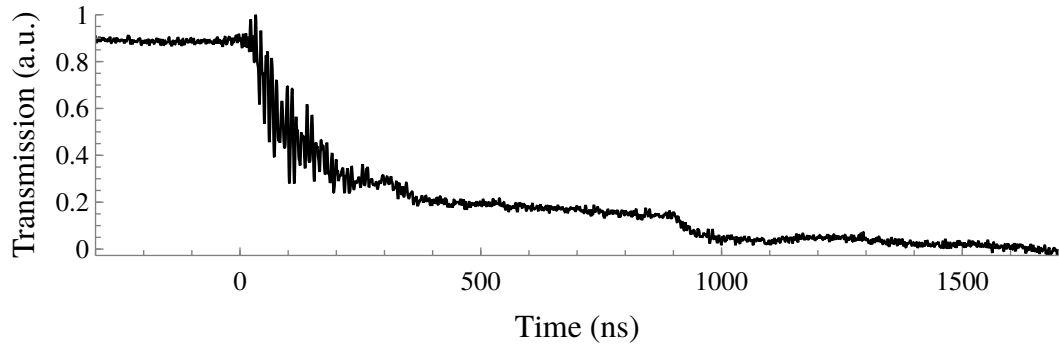


Figure 4.2: Measurement of the transmitted laser light at the nominal transition wavelength at 4.0 Torr of helium.

absorption spectra were measured over ± 3.85 GHz relative to the nominal transition frequency of the 2^3S_1 - $2^3P_0^o$ transition at intervals of 154 MHz. The absorption spectra were measured for time domains of –300-1700 ns relative to the voltage pulse. Additional measurements were made at the midstream position of the metastable densities from –88-700 μ s in order to investigate the loss mechanisms of the metastables.

The broadband electronic noise emitted by the fast pulses was a persistent issue and presented one the greatest challenges in the acquisition of accurate measurements. In order to reduce the noise present in the detector signal, the InGaAs photodiode was removed from the immediate area surrounding the discharge by the use of an optical fiber. The optical fiber was routed through a small opening in a grounded metal box where both the photodiode and the voltage amplifier resided. In addition, the DC power supply of the voltage amplifier was connected to an outlet on a Tripp-lite Isobar intended to provide isolation for the power input. The photodiode was connected directly to the input terminal of the amplifier minimizing the length between the two. Likewise, the amplifier was connected to a BNC bulkhead adapter by a 10 cm length of RG 50/U. The final connection to the oscilloscope was made by an additional 10 cm length of RG 50/U, running from the BNC bulkhead connection.

Figure 4.2 shows the transmission signal measured at the nominal transition wavelength while the plasma was active in 4.0 Torr of helium. The signal is an average of 200 indepen-

dent pulses. Further sampling had no appreciable effect on the waveform. As can be seen, despite the efforts to limit the electrical interference, there is still a substantial amount of noise present in the transmission signal. This is most noticeable in the large ringing which occurs for the first 200 ns after the voltage pulse. Without any kind of compensation for this noise it would be impossible to obtain reliable measurements of the transmission signal.

4.2 Noise Suppression & Absorption Analysis

The noise produced by the RPND was relatively consistent between pulses as well as over the duration of each experiment. As a result, it was possible to correct for the electrical noise and emissions from other transitions by measuring the signal from the photodiode in the absence of the laser and subtracting this from the signal with the laser. The acquisition process proceeded as follows:

1. Set desired laser wavelength.
2. Wait 5 s for laser output to settle.
3. Acquire 200 waveforms from photodiode.
4. Close shutter.
5. Acquire 200 waveforms from photodiode.
6. Repeat

The effect of this subtraction can be seen in figure 4.3 where the top heatmap shows the initial set of acquisitions with the laser on, and the middle heatmap shows the transmitted signal with the noise subtracted.

As the wavelength of the laser diode changed, so did the output power. This led to the gradient-like appearance of the top two plots in figure 4.3. In order to correct for this a measurement was made of the unattenuated laser power as a function of diode wavelength.

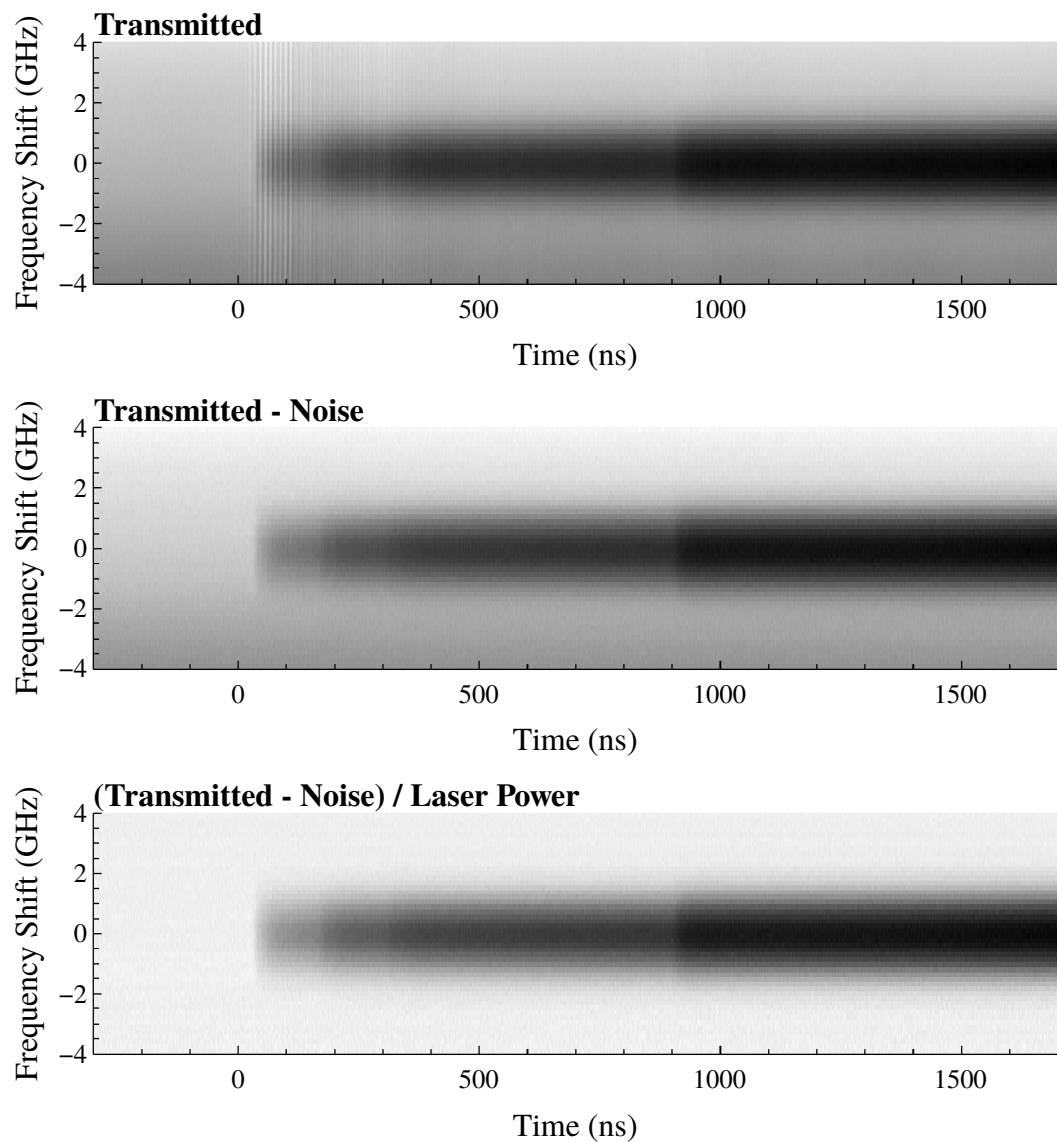


Figure 4.3: Heatmaps of the transmitted laser signal for the 4.0 Torr condition at various stages of post-processing.

This was done by deactivating the plasma and repeating the above acquisition procedure. The intensity of each point in the transmission spectra was then divided by the unattenuated laser power, producing the properly normalized transmission spectra.

These spectra were then analyzed using a transmission model based on the absorption cross sections described in Chapter 2. In a one-dimensional system, the change in intensity of an incident photon field (below the saturation limit), can be expressed as

$$\frac{dI(x, \omega)}{dx} = -\sigma(\omega)N(x)I(x, \omega) \quad (4.1)$$

where I is the intensity of the photon field as a function of distance x , ω is the frequency of the photons, N is the density of the interacting species, and σ is the interaction cross section. This equation has the simple solution,

$$T(\omega) = \frac{I(x, \omega)}{I_0(\omega)} = \exp \left[-\sigma(\omega) \int_0^x N(x') dx' \right], \quad (4.2)$$

where T is the transmitted intensity fraction, and I_0 is the initial intensity of the photon field. The absorption can be trivially obtained from the relation $A(\omega) = 1 - T(\omega)$.

For the purpose of analyzing the absorption spectra, a quantity called the line-integrated density will be defined. This is simply, $\langle N \rangle = \int_0^x N(x') dx'$. While equation 2.16 can be used to determine the absorption cross section it requires that a lineshape be specified. In general, it is preferable to select either a purely Gaussian or purely Lorentzian lineshape. This reduces the computational cost of spectral calculations in comparison to the use of the Voigt profile (equation 2.14). Whether the Voigt profile is necessitated or not can be determined by a comparison of the relative widths of the different broadening mechanisms. For a temperature of 300 K and a pressure of 8.0 Torr, it is found that $\Delta\omega_d = 1.7$ GHz and $\Delta\omega_a = 0.21$ GHz. Because neither broadening mechanism appears dominant, the choice was made to analyze the data with a Voigt profile, despite the added computational cost.

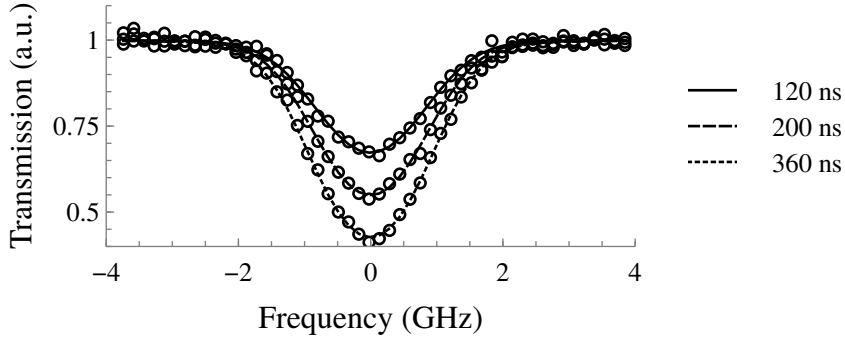


Figure 4.4: Comparison of the measured transmission profile (open symbols) and the computer-generated matches for at several different times for the 4.0 Torr operating condition.

Equations 4.2, 2.16, and 2.14 can be combined to form a model equation for the absorption spectrum. It can be seen that only two unknowns exist: the gas temperature, T_g , and the line-integrated density, $\langle N \rangle$. The model equation was matched to the measured spectrum at each time point using the Levenburg-Marquardt algorithm [106], as implemented by the SciPy library [107]. During the matching process, small variations in the center frequency of the laser diode were observed. This was assumed to be the result of long-term variations in the diode temperature that were not adequately compensated for by the temperature control system. The magnitude of these drifts were on the order of ± 60 MHz between experiments. This fluctuation in center frequency was measured for each experiment and used to correct the wavelengths in the post-processing.

4.3 Results

The matching algorithm proved robust enough to automatically match the transmission spectrum at each time step with no user intervention. Figure 4.4 shows three examples of the measured transmission spectra along with the computer-generated matches. The measured data cleanly coalesce to complete transmission far from the peak. In addition, the spectra show no evidence of the noise caused by the discharge. This suggests that the compensation

described in the previous section was adequate for these conditions. Across all cases, the total variation in the baseline transmission signal was approximately 0.02. This set a minimum line-integrated detection limit of approximately $3.0 \times 10^{14} \text{ m}^{-2}$, though the actual value varied with respect to the pressure and temperature.

4.3.1 Temperatures

The temperatures calculated for the metastables from the laser-absorption spectroscopy diagnostic are shown in figure 4.5. Prior to the pulse, the temperature estimates are subject to large variations. This is a result of the low metastable densities which precede the pulse. Without a substantial metastable population, the matching algorithm had difficulty discriminating between a combination of low temperatures and low densities (a small, narrow absorption spectrum) versus high temperatures and high densities (a very broad absorption spectrum).

Though it is not possible to provide an exact value of the errors in the calculated temperatures, the algorithm does provide an estimate of the standard deviation in its results. In all cases, the estimated standard deviation was less than 10 K by the end of the measurement period. Given this value, there appear to be no meaningful trends throughout the measurement period, and between the measurement locations.

In order to more clearly compare the temperatures at the different operating conditions, the results for each location were combined and averaged over the final 200 ns. This was then plotted with respect to the energy deposition calculations from Chapter 3, divided by the gas density. If the discharge was appreciably heating the helium, the temperature would be expected to increase with respect to the density-normalized energy deposition. As seen in figure 4.6 this does not appear to be the case. Indeed, most of the operating conditions show little to no statistical difference between each other and room temperature. The only exception to this is the 16.0 Torr operating condition with a mean temperature of 255 K. As no effort was made to cool the discharge tube, this appears to be an erroneous result. A

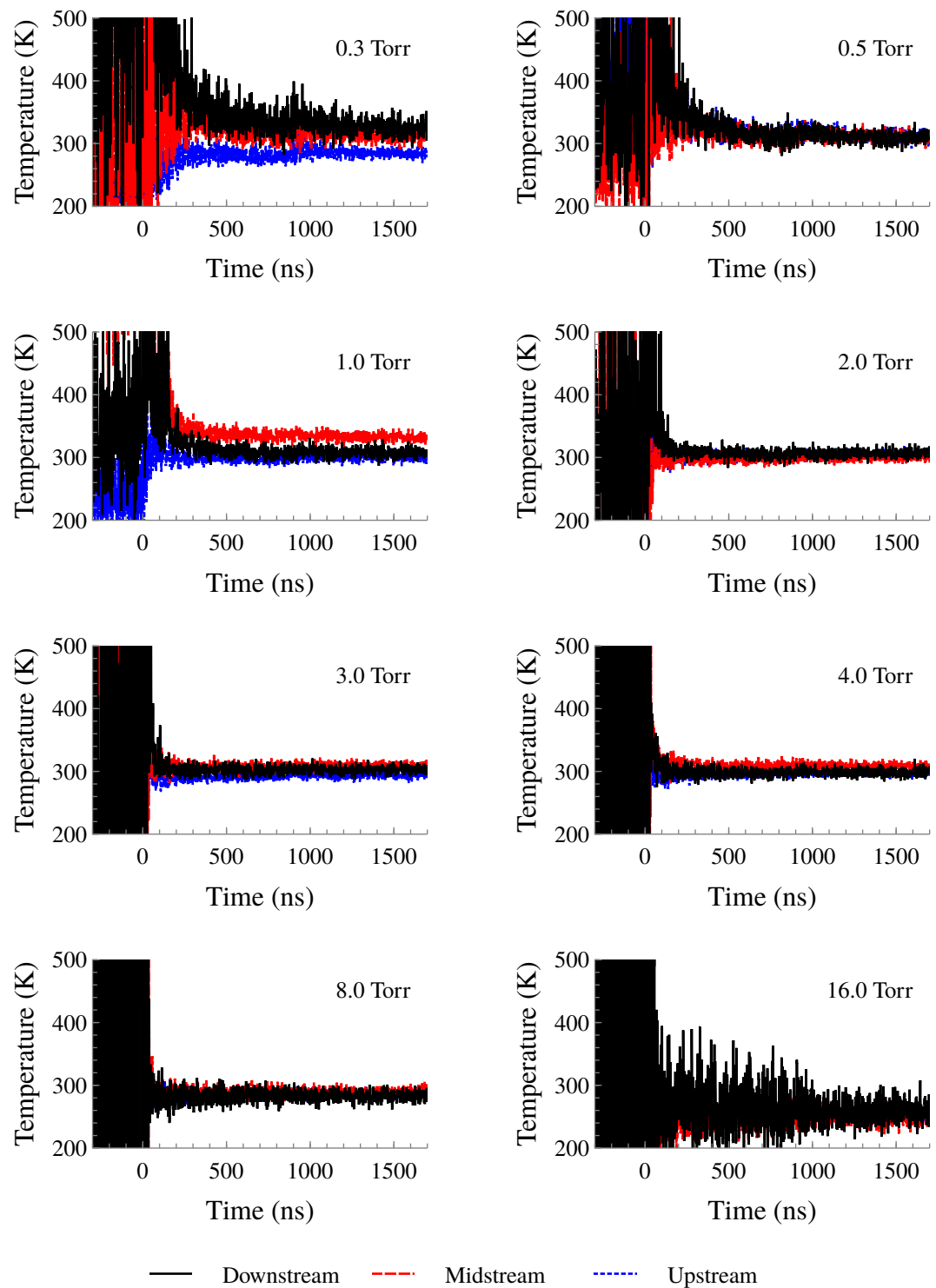


Figure 4.5: Plot of the gas temperatures at each of the operating pressures and each axial location as a function of time.

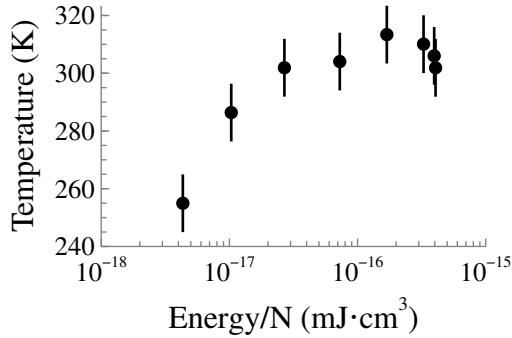


Figure 4.6: Plot of the average gas temperature as a function of deposited energy.

comparison of the calculated spectra and the original absorption spectra revealed no obvious errors. However, as will be seen later, the metastables were the least dense at 16.0 Torr. This, along with the large variation of the temperatures between time points suggest that the standard deviation in the calculations is higher than estimated.

Only a limited number of similar direct temperature measurements exist within the literature. The work of Walsh et al. [84] provides the most direct comparison. In their study, they measured the heating in a planar discharge with helium and a small admixture of oxygen as the working gas. The system was held at atmospheric pressure and had a gas flow rate of 5 slm. Instead of absorption spectroscopy, the rotational spectra of the oxygen was used to determine the temperature. Temperatures ranged from 300-340 K, depending on the average power dissipated in the plasma. Walsh et al. suggested that the observed temperature increase was a result of Joule heating, that is, heating of the gas as a result of electrons colliding with neutral particles. As this process scales with temperature, it would not be expected to be present in the trends from figure 4.6. The presence of a measurable fraction of a molecular gas (oxygen) allows for several other heating mechanisms to occur. Dissociation of the oxygen can impart translational energy to the daughter particles, heating the gas. Additionally, excited the energy contained in rotational and (to a lesser extent) vibrational states can be converted to translational energy in collisions [108].

Other experiments have demonstrated minimal gas heating for RPNDs. Plasma bullets,

like those of Laroussi and Lu [82, 83], tend to be associated with minimal heating. However, others have observed measurable heating with temperatures ranging from 400-1000 K [75, 76, 109, 110] (see appendix B for detailed study in air at NASA Glenn Research Center). A comparison of the experimental conditions shows that heating was only observed in molecular gases, though there were cases in which no heating was observed [111], likely a result of the low repetition rate and energy deposition. These similarities emphasize the importance of the additional heating pathways linked to molecular gases.

For comparison recent simulations and rate calculations [87, 112] have provided estimates of the electron temperature in the range of 10-20 eV. As a result, all of the discharges mentioned are very much nonthermal in nature. That said, the negligible heating in the helium RPND studied here may provide a significant advantage in some applications, as even the moderate temperature increases in molecular discharges can threaten material integrity. For example, most commercial polymers are only rated to 300° C, making them susceptible to damage without careful thermal management.

4.3.2 Line-integrated Densities

As described in the analysis section, the laser-absorption spectroscopy also yielded the line-integrated metastable densities. Figure 4.7 shows the metastables dynamics for each operating pressure and at each location. Similar to the temperature measurements, there is a substantial uncertainty during the pre-pulse period for pressures greater than 1.0 Torr. However, for 1.0 Torr and below, there are detectable populations of triplet metastables, around $7 \times 10^{14} \text{ m}^{-2}$. These excited atoms are the remnants of the previous pulses which have not been destroyed or left the system. Despite the efforts made to limit the noise in the signals, there is a significant number of erroneous data points in the downstream measurements for pressures below 3.0 Torr. It is not clear why this measurement location was particularly susceptible to plasma-related noise. In all cases, the photodiode remained in the grounded enclosure and only optical components were moved.

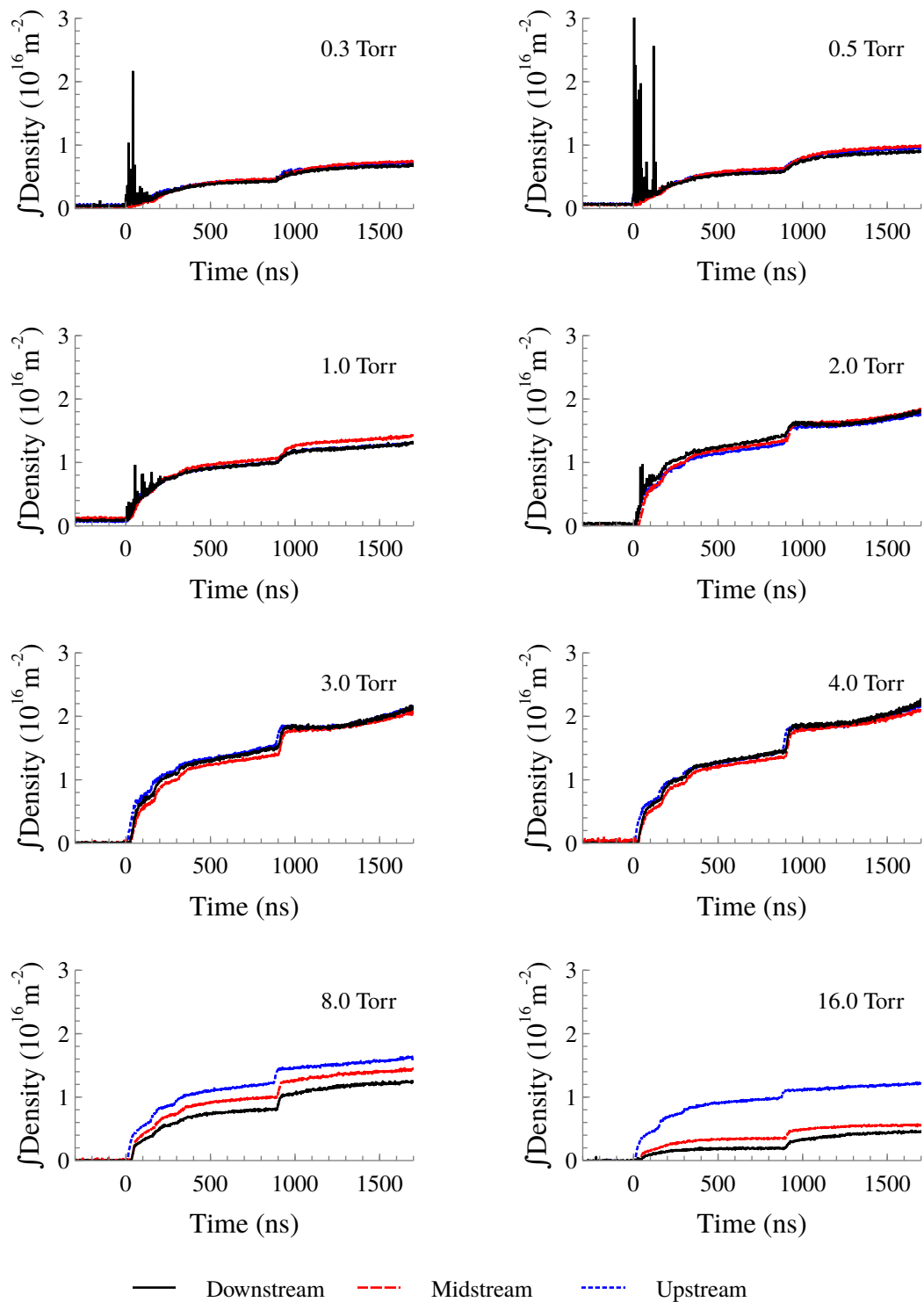


Figure 4.7: Plots of the line-integrated metastable densities at each of the operating pressures and each axial location as a function of time.

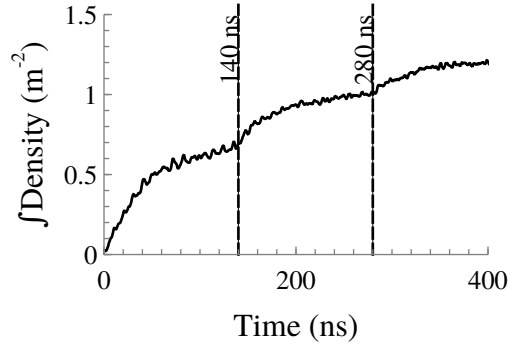


Figure 4.8: Zoomed in view of the increases in metastable density as a result of pulse reflections.

In each case, the metastable population exhibits two short bursts at 140 and 280 ns. This is shown in more detail in figure 4.8. The timing of these bursts correlate with the arrival of pulse reflections. This suggests that even after the plasma has formed, additional pulses are still able to deposit a significant amount of energy in the plasma. This appears to contradict the predictions made by the one-dimensional drift models of Adamovich et al. [67] and Nikandrov et al. [68] which stated that little energy is coupled into the plasma after breakdown occurs. In addition to the smaller bursts in density, another can be noted at about 900 ns which corresponds to the double-pulsing observed in the current-voltage characteristics of Chapter 3.

By 200 ns after the pulse, the estimated standard deviation in all cases is approximately $2 \times 10^{14} \text{ m}^{-2}$. Based on this, it can be concluded that the metastable populations had no significant axial dependence below 8.0 Torr. However, both 8.0 and 16.0 Torr conditions showed notable differences in the metastable population as a function of distance from the anode. As might be expected, the upstream location (closest to the anode) has a high metastable population than the other two. At 16.0 Torr, the line-integrated density at the upstream location was over twice that of either location.

This behavior is reminiscent of that observed by Vasilyak et al. [19] in FIW devices. It was noted that the electric field of the wave would attenuate with distance. In order to

interpret this, they considered the wave to consist of two components: a moving ionization front with a finite width, and the plasma left in its wake. They state that the plasma, with its finite conductivity, will have some voltage drop across it, and as it grows, this drop increases. As a result the voltage drop across the ionization front can never be greater than the overall potential applied to the system and is constantly diminishing as it moves away from the energized electrode. If true, this behavior would be associated with a reduction in the rate of metastable generation in the front, thus explaining the high pressure data in figure 4.7.

In order to compare the metastable measurements to other results, it's necessary to know the density as opposed to the line-integrated value. In this case, it shall be assumed that the metastable atoms are distributed uniformly along the beam path through the plasma. This suggests that the metastable densities in the RPND lie in the range of $0\text{--}1 \times 10^{12} \text{ cm}^{-3}$. This is significantly less than the measurements of Stevefelt, Pouvesle, and Bouchoule [113], however their system involved an atmospheric-pressure discharge and energy deposition of up to 0.2 J (compared to a maximum of 5.5 mJ in this experiment). Urabe et al. [114] measured metastable densities of up to $4 \times 10^{11} \text{ cm}^{-3}$ with laser-absorption spectroscopy in a helium jet at atmospheric pressure. Nersisyan, Morrow, and Graham made measurements suggesting a metastable density of about $1.5 \times 10^{10} \text{ cm}^{-3}$ in a DBD [115]. Though the discharge was not pulsed, Millard et al. measured densities from 5×10^9 - $1.2 \times 10^{11} \text{ cm}^{-3}$ in helium glow at 2.0 and 5.0 Torr [105]. While none of these experiments are a direct comparison, they do suggest that the results obtained above are within reason.

4.3.3 Metastable Destruction

In addition to the fast metastable dynamics, measurements were made of the long-term trends of the metastable populations. Afterglow measurements such as these are less subject to the noise and bandwidth limitations of the short timescale measurements. This makes it possible to obtain relatively clean and precise values for the metastable densities. However, without the applied electric field, the nonequilibrium dynamics of the system rapidly disap-

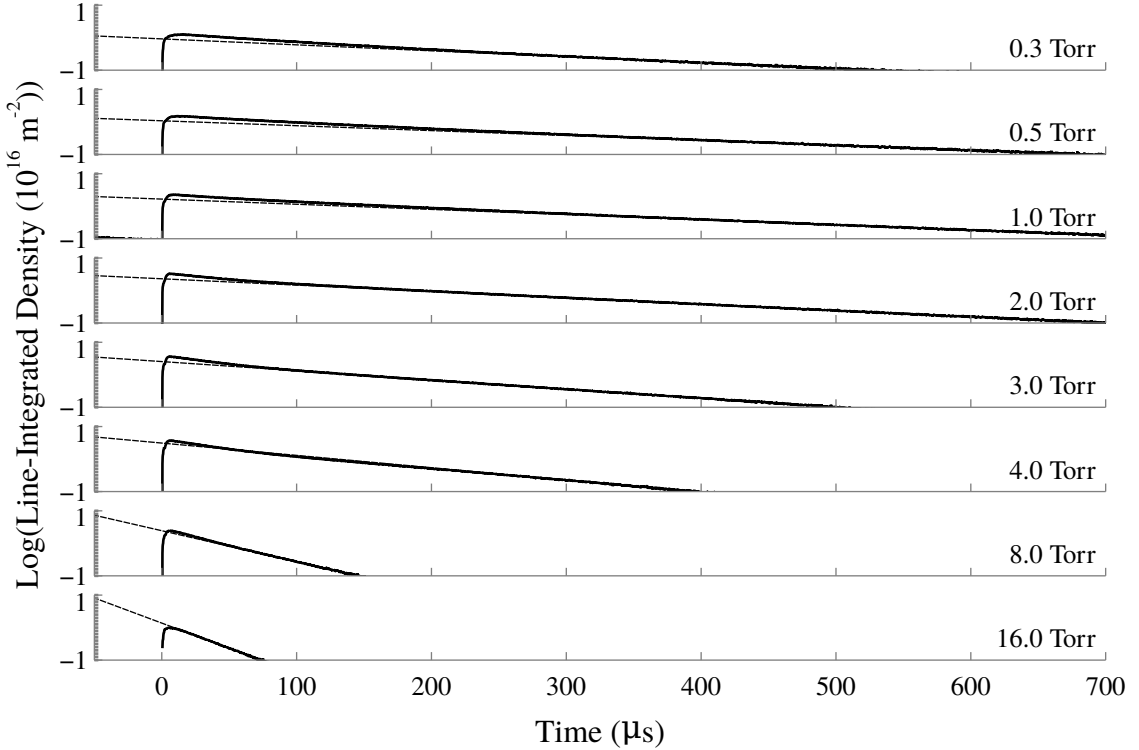


Figure 4.9: Measurements of the long-duration metastable density trends. Exponential fits are indicated by the dotted lines.

pear. Therefore, while these measurements provide some insight on the initial conditions, they cannot describe the dynamics of the RPND alone.

That said, a large body of work has been conducted on helium afterglow discharges, which makes this regime attractive as a point of comparison. Furthermore, these measurements include the peak metastable populations for each operating pressure (which are missing from figure 4.7). The peak metastable densities and the lifetime of the metastable populations are of interest as they can produce charged particles through Penning ionization of each other or impurities [115]. This extends the ionization period in rare gas RPNDs well past the voltage pulse itself. Also, as seen in figure 2.6, all excited states in the triplet manifold will eventually decay to the triplet metastable level. Thus, a substantial portion of the energy deposited in the plasma is contained in this one level.

Figure 4.9 contains logarithmic plots of the metastable populations for each operating

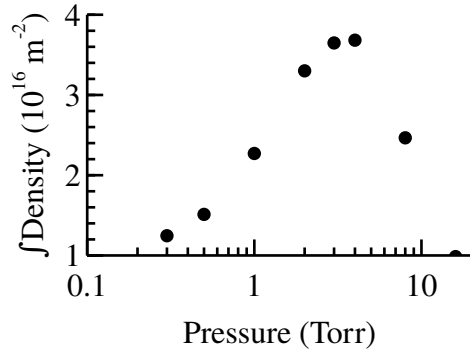


Figure 4.10: Peak line-integrated metastable densities as a function of pressure.

condition, all measured at the midstream location. In addition, an exponential function was fit to the tail of each trend, represented by the dotted line. On these time scales, the destruction of metastables in the RPND apparatus can be described by four different mechanisms: diffusion, Penning ionization of impurities, Penning ionization between metastables, and three-body collisions resulting in helium dimer formation. All processes with the exception of the Penning ionization between metastables have an exponential dependence, thus any deviation from an exponential decay is likely a result of Penning ionization [116].

As can be seen, a number of the decay curves deviate from a strictly exponential decline. This deviation appears to be more substantial at the lower pressures. For example, the decay at 16.0 Torr appears strictly exponential. Initially, this deviation was believed to be the result of Penning ionization between metastables. The rate at which this takes place is proportional to the square of the metastable density. Therefore, if this is the process responsible for these deviations, it should be most severe for the highest metastable densities. However, per figure 4.10, this is not the case. If Penning ionization between metastables were the dominant loss mechanism, it would be reduced at the lower pressure conditions, contrary to what was observed.

Ultimately, the behavior of the metastable populations in the afterglow can be best understood by a comparison of the depopulation rates for each process. Figure 4.11 illustrates the aforementioned decay processes at 0.3 Torr, for a variety of metastable densities. The

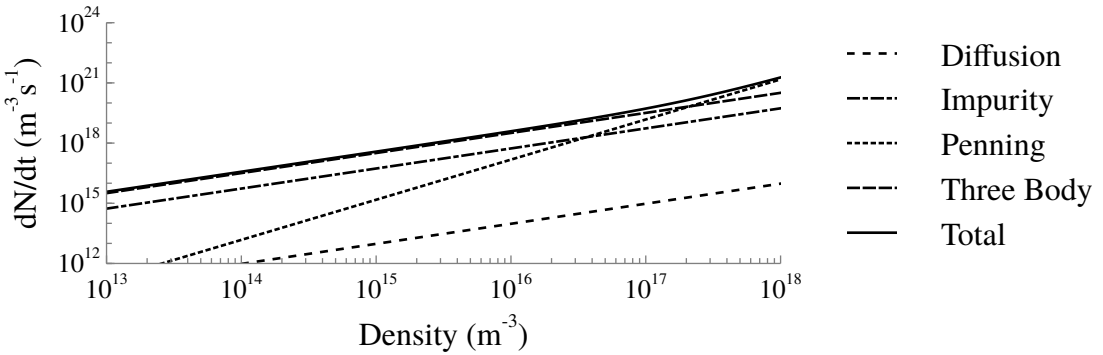


Figure 4.11: Comparison of the decay rates for various processes at 0.3 Torr as a function of metastable density.

rate constants for these processes were obtained from the study by Deloche et al. [116] and the work of Pouvesle et al. [113] (specifically for the rate of Penning ionization of nitrogen impurities). The gas impurities were assumed to be nitrogen, and the mole fraction was assumed to be 80 ppm, as was estimated in Chapter 3.

As can be seen, the dominant loss mechanism above metastable densities of $2 \times 10^{17} \text{ m}^{-3}$ was Penning ionization between two metastable atoms. Below this density, the three-body process responsible for dimer formation was dominant. However, the three-body process scales with the square of the neutral gas pressure. As a result, as the pressure is increased this mechanism quickly overtakes all the others. Therefore, the exponential dependence of the decay at higher pressures is not representative of any change in the importance of Penning ionization between metastables, but rather the increasing importance of three-body collisions. This severely restricts the longevity of the metastable states at higher pressures, and reduces their ability to prolong the charged particle population.

From figures 4.11 and 4.9, it can be seen that, aside from the deviations at lower pressures, the decay curves are well-matched by the exponential functions. As a result, it is possible to use the fitting functions to estimate the pre-pulse metastable densities as a function of pressure. These estimates are consistent with the short-scale measurements from figure 4.7. The estimated values of the pre-pulse metastable densities are compiled in ta-

Table 4.1: Listing of the extrapolated, pre-pulse line-integrated metastable densities, and decay coefficients as a function of pressure.

Pressure (Torr)	Integral Density (m^{-2})	Decay Constant (s^{-1})
0.3	1.34×10^{14}	4.23×10^3
0.5	3.36×10^{14}	3.47×10^3
1.0	4.29×10^{14}	3.65×10^3
2.0	2.60×10^{14}	4.48×10^3
3.0	3.94×10^{13}	6.47×10^3
4.0	5.04×10^{12}	8.73×10^3
8.0	7.08×10^6	2.20×10^4
16.0	4.74×10^0	3.56×10^4

ble 4.1. along with the decay constants. These results show reasonable agreement with the earlier pre-pulse metastable densities, and are within a factor of two or less. This supports the previous measurements, and provides some confidence that the other extrapolations are also accurate representations of the pre-pulse metastable densities.

The decay constants are about an order of magnitude larger than those recorded by Phelps and Molnar [104] at similar pressures. This almost certainly reflects the presence of the impurities in the system. Figure 4.11 shows that impurities are a moderate contributor to the decay of the metastable atoms even at low pressures. Similar measurements and calculations by Deloche et al. [116] confirm the lower decay constants of Phelps and Molnar. In addition, their results showed a relatively consistent proportionality between the electron density and metastable density (on the order of one for every ten). Therefore, these density values may be read as a rough approximation of the electron densities within the RPND.

4.4 Summary

A laser diode-based absorption spectroscopy experiment was set up to observe the development of the RPND on short (0-1700 ns) and long (0-700 μs) time scales. The measurements on the short time scale provide some of the only detailed measurements of the RPND during its development. The design of the system and post-processing software carefully

accounted for plasma-related noise, background emissions, and laser drift. The absorption spectra model showed excellent agreement with the measured spectra and the matching algorithm produced consistent and reliable results almost all cases.

Temperature measurements from the Doppler broadening of the absorption spectra showed no appreciable gas heating at any operating pressure. These results contrast with some measurements made in molecular RPNDs where a variety of additional mechanisms are available to transfer kinetic energy from electrons to heavier species.

The line-integrated density results indicate that the plasma is axially uniform across the tube at lower pressures. The 8.0 and 16.0 Torr conditions show significant attenuation in the metastable densities as a function of distance from the anode. This may present a geometric limit to the use of similar RPNDs in material processing. The dominant metastable loss mechanism at low pressures and short time periods is Penning ionization between metastables. However, losses are eventually dominated by three-body dimer formation for all cases. Peak metastable generation is optimized at 4.0 Torr. However, the peak pre-pulse metastable densities, and possibly the electron densities, are optimized at 1.0 Torr. Interestingly, this corresponds with the maximum measured energy deposition from Chapter 3.

These measurements provide an important foundation upon which to develop a more encompassing perspective of how the RPND develops. Specifically, the generation of the metastable atoms is related to a number of other plasma parameters, including: electron density, electron temperature, EEDF, and electric field. Provided a sufficiently detailed model, it should be possible to capture these relationships, and use the measured metastable densities to infer the evolution of these quantities as well as other excited states in the system.

CHAPTER 5

Modeling

Though the line-integrated metastable densities are one of only a few measurements made in the development of the RPND, they only provide a limited view of what is happening. In addition to the metastables are ions, electrons, a vast array of other excited states, and the electric fields. In an effort to expand on the details of what is occurring within the RPND, it is desirable to develop a model which can infer other properties from the metastable measurements. This is possible, because the electrons which gain energy from the electric fields are those which excite the metastables, other excited states, and ions. The ideal model would solve the Boltzmann equation (equation 2.1) for each species, over the entire geometry, in all dimensions, for as long as was required to reach equilibrium.

Unfortunately, these requirements are somewhat problematic. Scale lengths of $10 \mu\text{m}$ are required in order to resolve the sheath effects, resulting in approximately 2×10^{13} spatial cells. Conservatively, the time steps would be about 1 ns in length. At a minimum, the system required about five minutes to reach equilibrium, thus necessitating 3×10^{11} solution steps. The largest velocity can be estimated as an electron accelerated across the full applied potential (6.6 keV), and the lowest velocity would be room temperature (0.04 eV). This produces a velocity discretization of about 6×10^7 cells. Thus the size of the parameter space in question is about 3.6×10^{32} . Given that the fastest computer in the world operates at 39 petaflops, a calculation of this magnitude would take around 0.3 billion years. Of course, this is for only a single particle species, the total number in the system is runs in the

dozens (not including the impurities).

5.1 Model Development

It should be apparent that the Boltzmann equation must be simplified in order to model the system in a reasonable amount of time. As discussed in Chapter 2, the most common approach to this is the use of moments of the Boltzmann equation which drastically simplifies the velocity terms. Frequently, the moments of the Boltzmann equation are used to develop various fluid approximations for plasmas [91] (e.g. the two fluid equations, the magnetohydrodynamic equations, etc.). This approach has been tremendously successful in the description of everything from plasma display panels [117] to interstellar plasmas [118].

There are some limitation to the capabilities of these fluid descriptions. For one, they require some assumption on the form of the EEDF. Often, the distribution is assumed to be a Maxwell-Boltzmann or Druyvesteyn, depending on the plasma conditions. In others, an approximate solution of the Boltzmann equation may be used to tabulate rate coefficients as a function of the mean energy [119]. In addition to this issue of the EEDF, fluid models in large or complex geometries can still be quite computationally expensive. This can limit the number of species and reactions which can be addressed [90].

In order to obtain an estimate of the detailed dynamics which occur as the RPND develops, it is necessary to consider additional simplifications of the Boltzmann equation. One such possibility is the use of a global model where the spatial dependence of the plasma parameters is assumed. This allows global model simulations to ignore the geometry of the system and focus on the particle interactions for long periods of time with reasonable computational requirements.

Here, a global model will be developed to describe the evolution of the plasma parameters along the measurement chords during the first pulse, and before the reflection. As was seen in the metastable measurements, there was little axial variation over the length of the

discharge. Thus, as far as the model is concerned, variations across the beam radius are negligible. However, it has been noted that a similar FIW [19] and the same RPND [120] exhibit radial variations in emission intensity, electron density, and metastable density. Furthermore, these variations appear to depend strongly on the operating pressure. Unfortunately, the cause of this is not clearly understood, though it has been suggested that high-energy electrons from the walls may be responsible [121]. Lacking any empirical, theoretical, or numerical results that provide the evolution of the radial profile during the discharge, it is necessary to assume one. In this case, the plasma will be assumed to be uniform across the diameter of the discharge. This assumption will affect the accuracy of the inferred plasma parameters, however future improvements in the understanding of these radial variations can be easily incorporated into the described model.

5.1.1 Continuity Equation

The global model begins with equation 2.4, the continuity equation. Having assumed that the spatial variations are zero, the equation reduces to,

$$\frac{dn_\alpha}{dt} = G_\alpha - L_\alpha, \quad (5.1)$$

where α identifies the particle species, G is the gain term, and L is the loss term. The gain and loss terms represent a large range of possible processes which are determined, in part, by the species under consideration. In this model, only helium, excited helium states, helium ions, and electrons will be treated. While impurities and dimers are very much a part of the discharge, this occurs on time scales that are relatively long in comparison to the excitation period. As was noted in Chapter 4, only 140 ns elapse before the reflection arrives at the plasma, while the e-folding time of the fastest decay is about 25 μ s.

Given the species of the system, there are several processes that should be given consideration for inclusion in the model.

1. Electron impact ionization
2. Electron impact (de)excitation
3. Atomic impact (de)excitation
4. Atomic excitation transfer
5. Dielectronic recombination
6. Three-body recombination
7. Radiative decay
8. Diffusion

As with the impurities and dimer formation, diffusion occurs on a much longer time scale, and thus is neglected. Three-body recombination in the volume of the discharge is not important at the estimated temperatures and densities [90], therefore this too is neglected. Dielectronic recombination is also quite rare, however the process was incorporated as part of the early models and thus maintained through the final revision. Inter-atomic excitation and de-excitation is not generally considered important given the low energies of the atoms in a discharge. However, excitation *transfer* can be an important process in gaseous discharges [90], making their inclusion necessary. Also important are the electron impact ionizations and excitations, as well as the radiative decay of the atoms.

Given these processes, it is possible to rewrite equation 5.1 as,

$$\frac{dN_i}{dt} = n_e \left[\sum_{j \neq i} N_j K_{j,i}^e(T_e) - N_i \sum_{j \neq i} K_{i,j}^e(T_e) \right] + \left[\sum_{j > i} N_j K_{j,i}^o - N_i \sum_{j < i} K_{i,j}^o \right] + N_g \left[\sum_{j \neq i} N_j K_{j,i}^a - N_i \sum_{j \neq i} K_{i,j}^a \right]. \quad (5.2)$$

In these equations, the subscripts of i and j represent states of helium, N is a state density, K is a rate coefficient, T_e is the electron temperature, and N_g is the neutral helium density. The first subscript of the rate coefficients represents the initial excited state while the second coefficient represents the final excited state. Therefore, K_{ij} represents a process that depopulates state i in favor of state j .

This equation is split into three sets of processes, represented by the superscripts of the rate coefficients: e - electronic, o - optical, and a - atomic. The first bracketed term on the right hand side contains all the rate coefficients for electron impact excitation and de-excitation, including ionization processes. The second bracketed term contains the rate coefficients for optical transitions in and out of the state. The final bracketed term contains the gains and losses as a result of excitation transfer caused by collisions with the ground state. Collisions between excited states are neglected given their relatively low densities.

The rate coefficients in equation 5.2 are compiled from a number of different sources. This is particularly straight forward in the case of the optical and atomic transitions, as neither features any dependence on the EEDF. The optical transition rates and level energies were obtained from the NIST Atomic Spectra Database [102]. The excitation transfer rate coefficients were from the studies of Catherinot and Dubreuil [122, 123]. These coefficients only covered the transitions of $\Delta n = 0$ for $n = 3, 4$ and no constants were found for other n or $\Delta n \neq 0$.

The semi-empirical relations derived by Ralchenko et al. [124] were used to calculate the electron (de)excitation and ionization cross sections through $n = 4$. These represent the most accurate set of cross sections available for neutral helium and have a quoted accuracy of 10-30% for $\Delta S = 0$, and $\geq 30\%$ for $\Delta S \neq 0$. The work of Ralchenko only provides the inelastic cross sections for collisions which increase the energy of the excited state. The inverse or superelastic cross sections can be calculated using the principle of detailed balance [100],

$$\sigma_{ji}(\epsilon) = \frac{\epsilon}{\epsilon \Delta \epsilon_{ij}} \frac{g_j^2}{g_i} \sigma_{ij}, \quad (5.3)$$

where $\Delta\epsilon$ is the threshold energy of the ij reaction and the g values are the statistical degeneracy of the states. Dielectronic recombination rates were adapted from the work of Nahar [125]. These cross sections can be used to calculate the rate coefficients for each reaction using equation 2.5. However, this poses the problem of what kind of energy distribution to use.

5.1.2 Distribution Effects

Per the discussion of the Boltzmann equation in Chapter 2, there are two readily available equilibrium solutions: the Maxwell-Boltzmann distribution, and the Druyvesteyn distribution. However, research by Starikovskaia and Starikovskii [24] has shown that the EEDF in a nitrogen FIW can deviate from both of these solutions. Such a result is not too surprising given the non-equilibrium nature of the FIW discharge. Since the RPND shares many of these same properties, it is possible that the equilibrium solutions do not apply to the RPND either.

In order to better understand how the energy distributions may behave in a RPND, a numerical study of the EEDF in a helium RPND was conducted. First, PIC code was used to simulate the effect of a voltage pulse on electrons in a quasi zero-dimensional geometry. This provided a series of baseline EEDFs which varied with respect to time. Then, at each time point, the mean energy was calculated from the PIC results. The mean energy was then used to generate equivalent approximate solutions of the Boltzmann equation, and Maxwell-Boltzmann distributions.

PIC simulations do not attempt to solve the Boltzmann equation directly. In essence, they are a model of an actual experiment and can have one, two, and three dimensional geometries. They consider a population of discrete macro-particles within the specified geometry, subject to specified fields, and governed by the basic laws of motion [6]. While each macro-particle has a specific location, velocity, charge, and mass, it is not the same as a single physical particle. It also possesses a statistical weight which allows it to repre-

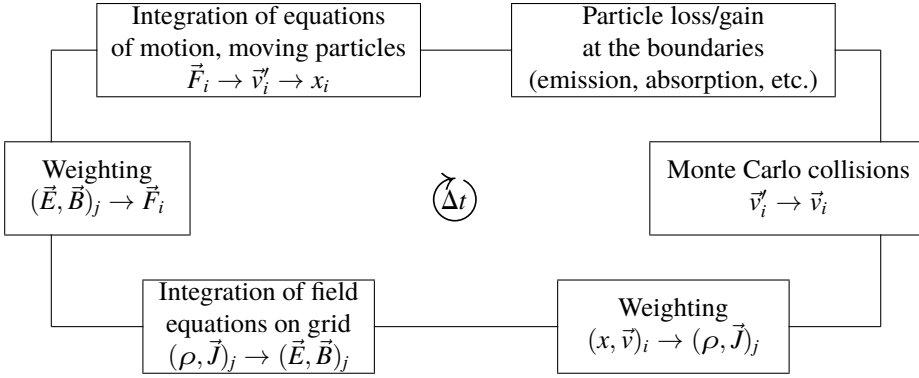


Figure 5.1: Schematic description of the PIC simulation process, adapted from [6].

sent a *group* of physical particles. Provided enough macro-particles, their velocities can be compiled to construct an estimate of the real EEDF.

The process by which the PIC simulation is conducted is illustrated in figure 5.1. The process begins with the definition of a system geometry and an applied electromagnetic field, \vec{E} and \vec{B} . In this case, the system is strictly one-dimensional, so each macro-particle only possess one spatial component, x . However, to account for magnetic field effects, each macro-particles possesses three velocity components, \vec{v} . This is followed by an initialization of the particle positions and velocities. The number of particles and the their positions are usually chosen to given a specific plasma density, and the velocities are often chosen to represent some initial distribution of energy. The Lorentz equation, $\vec{F} = q(\vec{E} + \vec{v} \times \vec{B})$, is then used to push each particle to a new position for a given time step, Δt . Particles born or lost at the boundaries are then accounted for. This is followed by a modeling of collisions (including ionization and excitation) using Monte Carlo techniques [6]. The charges of the macro-particles are then weighted to a spatial grid, and the fields are recalculated, and the next time step begins.

The XPDP1 code, developed by Verboncoeur et al. [126], was used to conduct the PIC simulations. The code was originally designed to simulate a one-dimensional discharge between two parallel electrodes. However, the electrodes complicate the study of

the EEDF. Charged particle collection near the boundaries will introduce spatial variations in the EEDF. In addition, such collection can lead to large regions of space charge which can shield out the applied electric field. In order to address these issues, the code was modified to use periodic boundary conditions. Such conditions result in a quasi zero-dimensional simulation, equivalent to a plasma of infinite extent. This eliminates the issue of spatial variations in the EEDF.

Previous measurements of the electric field in a similar FIW suggested that the electric field values varied from 0-350 Td [87]. Based on this, it was decided to examine the distribution characteristics from 10-600 Td. This range should be adequate to cover all conditions within the RPND in question. The background gas was helium at a pressure of 2.0 Torr. The initial plasma was assumed to be quasineutral with a density of $1.0 \times 10^8 \text{ cm}^{-3}$ and 10^4 macro-particles. Electrons were initialized with a thermal energy of 2.0 eV, and the helium ions were given an initial energy of 0.025 eV.

The internal set of cross sections, which include elastic scattering, excitation, and charge exchange were used. The cross sections have a semi-empirical form which increases linearly with energy to a peak value after which it declines as the logarithm of the energy, divided by the energy. The time domain of the simulation was 10 ns, approximately the time required for the EEDF to reach equilibrium with the applied field. The distributions from the PIC simulations were sampled every 0.25 ns. The spatial domain was discretized at $1 \mu\text{m}$ intervals over a total domain of 10 cm. Based on the highest energy electrons in the system, a time step of $4 \times 10^{-13} \text{ s}$ was chosen in order to satisfy the Courant-Friedrich-Lowy stability condition.

BOLSIG+ was used to obtain the approximate solutions of the Boltzmann equation [119]. This is a publicly available computer code which uses the two-term expansion of the Boltzmann equation to solve for the EEDF for a given electric field. In this approach, Legendre polynomials are used to expand the EEDF into an equilibrium solution and a relatively small non-equilibrium component. This implied assumption, that the distribution

is accurately represented by a small perturbation superimposed on an equilibrium solution, puts constraints on the magnitude of the reduced electric field. In the case of BOLSIG+, the solver fails to converge for fields approaching 1000 Td.

The solver was initialized with the cross sections for helium generated by Alves and Ferreira [127]. The temporal growth model for electrons was used, and the electron-electron collisions were not neglected as a result of the low ionization fraction in the RPND. Solutions were calculated for a range of electric fields and then tabulated according to their mean energy. A nearest neighbor interpolation scheme was used to generate an EEDF for the mean energies from the PIC simulations.

These same energies were used to determine equivalent Maxwell-Boltzmann distributions for comparison. The results of these calculations can be seen in figure 5.2, as a series of contour plots comparing the results for each approach. The jaggedness of the PIC simulations results from the finite number of particles in the system and the low probability of high energy electrons. This problem is ameliorated at higher electric fields where the probability of high-energy electrons increases. An increase in the number of electron macro-particles, resulting from ionization, also helps to reduce this effect.

At 10 Td, the EEDFs are relatively unchanged over the duration of the simulation. The subtle slopes of the contours suggest a small increase in the overall temperature and energy of the system. The rate of increase in temperature increases as the value of the electric field is increased. At 30 Td, the contours of each approach are essentially linear with similar slopes. The only noticeable deviation is the closer spacing of the contours from BOLSIG+. Thus the probability distribution falls off faster with energy for this case relative to the PIC simulations and the corresponding Maxwell-Boltzmann distributions.

At 60 and 100 Td, the PIC results and Maxwell-Boltzmann distributions continue to feature contour spacings which increase linearly with time. In contrast, the BOLSIG+ solutions have contour spacings which are monotonically increasing, but at a rate which varies in time. Additionally, the spacing between the various levels is less consistent than for the PIC

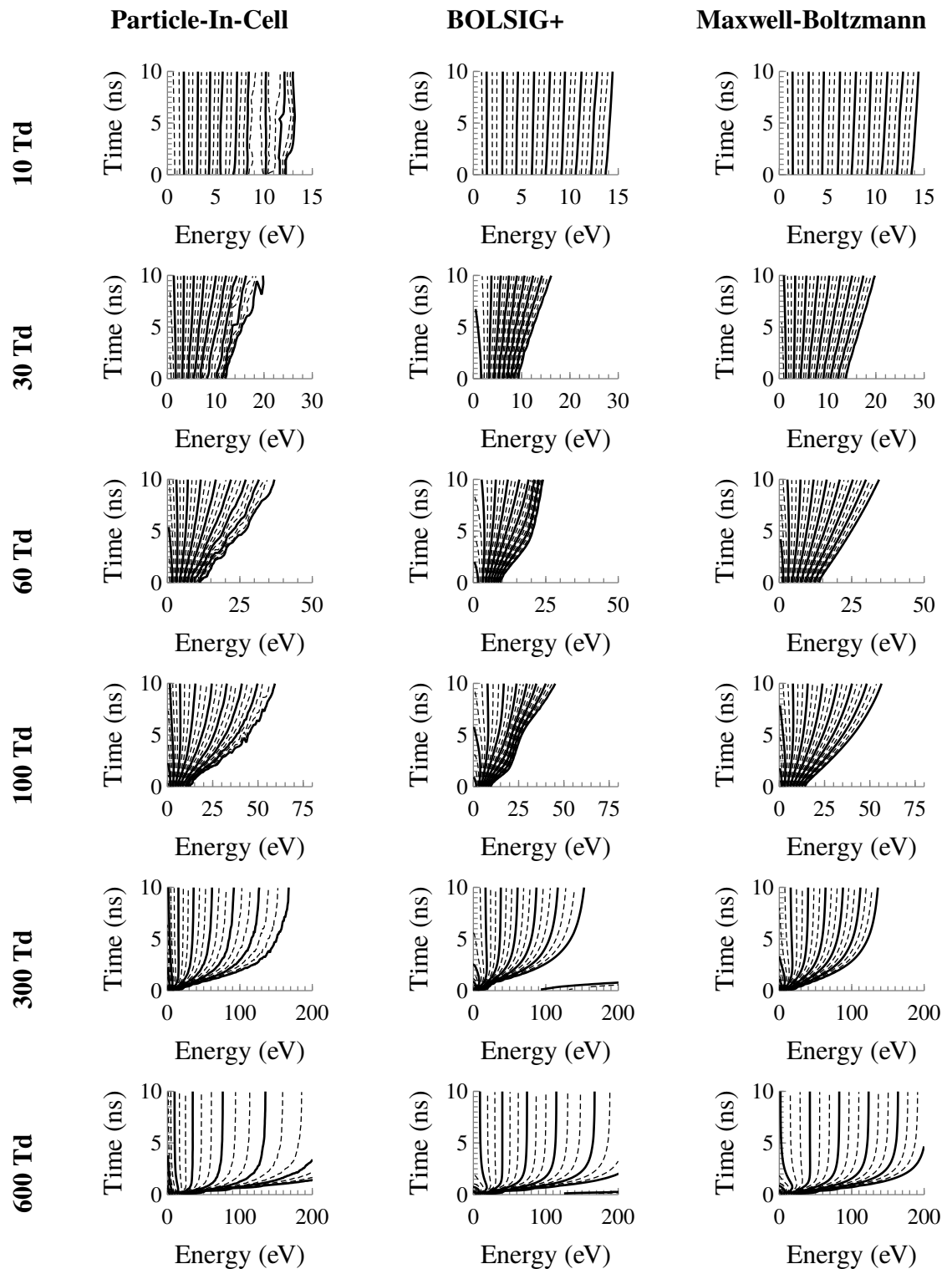


Figure 5.2: Contour plots of the EEDFs determined from PIC simulations, and the corresponding Maxwell-Boltzmann distributions for a range of electric fields.

simulations or the Maxwell-Boltzmann distributions. By the end of the simulation period, the overall width of BOLSIG+ contours is less than either of the other approaches.

However, by 300 and 600 Td the situation has slightly changed. The Maxwell-Boltzmann distributions show consistently less breadth than the PIC results of the BOLSIG+ solutions. Close examination shows that the PIC simulations have larger populations of low energy (less than 20 eV) and high energy (greater than 100 eV) electrons. This can be traced back to the form of the helium cross sections used in XPDPI. The only reactions available to electrons in the simulation are elastic scattering, excitation (19.6 eV threshold), and ionization (24.6 eV threshold). Thus the electron population is depleted at values above around 20 eV, as a result of these inelastic processes. Likewise, the electron population begins to rebound at higher energies as the inelastic processes turn off. The Maxwell-Boltzmann solutions are quite simple and do not account for the variation of the cross sections with respect to energy. This explains the increased consistency of the PIC and BOLSIG+ results at high electric field values.

Generally, the Maxwell-Boltzmann results appear to provide the best match to the PIC simulations at electric fields of 100 Td and below. At higher fields, the BOLSIG+ results provide a better approximation of the PIC results. If the electric fields measured by Takashima et al. are the same as those in the RPND studied here, then the Boltzmann solver would be the best choice at the peak field values. However, for a very large fraction of the time, the Maxwell-Boltzmann distribution would appear to provide the best approximation of the electron distributions in the system. As a result, it was decided to use this distribution for the development of the global model.

5.1.3 Energy Equation

Given a form for the distribution function, it is now possible to calculate the rate coefficients in equation 5.2 at each time step. However, as was seen in figure 5.2, the distribution function changes over time. In that case, the PIC simulations were used to calculate the mean

electron energy which, in turn, was used to determine the appropriate Maxwell-Boltzmann distribution. However, as of yet, no mechanism has been provided to evolve the mean electron energy in the absence of such simulations.

With suitable assumptions, equation 2.7 (the second moment of the Boltzmann equation) can provide the means to evolve the mean energy with each time step. Given the assumptions underlying the global model, the spatial derivatives can be neglected so that

$$\frac{d}{dt} \left(\frac{3}{2} p_e \right) = \frac{d}{dt} \left(\frac{3}{2} p_e \right) \Big|_{\text{coll}}. \quad (5.4)$$

Using the isothermal equation of state, $p = n k_B T$, this can be rewritten as,

$$\frac{d}{dt} \left(\frac{3}{2} n_e k_B T_e \right) = \frac{d}{dt} \left(\frac{3}{2} n_e k_B T_e \right) \Big|_{\text{coll}}. \quad (5.5)$$

The term on the RHS is the collision operator which expresses energy gained or lost by electrons¹ in particle collisions.

Several different forms of particles collisions must be considered by the global model. Once the electron population surpasses the 19.6 eV threshold, a great deal of energy will be exchanged with excited helium species through inelastic collisions. In addition, the electron population will tend to thermalize with the background gas over long periods of time via elastic collisions. Finally, energy is gained by the electrons through the applied electric field. Together, these phenomena replace the term on the RHS of equation 5.5 with,

$$\frac{e^2 n_e E(t)^2}{m_e k_m(T_e) N_g} - n_e k_m(T_e) N_g \left(\frac{3m_e}{M} \right) \frac{3}{2} k_B (T_e - T_g) - n_e \sum_i \sum_{j \neq i} K_{ij}^e N_i \Delta \epsilon_{ij}, \quad (5.6)$$

where $E(t)$ is the time-varying electric field, k_m is the electron momentum transfer frequency from Pack et al. [128], and $\Delta \epsilon_{ij}$ is the energy lost or gained by the electron in atomic

¹In some plasmas, it is desirable to also treat gas heating with a similar equation as it can have an appreciable impact on certain rate constants. However, as noted in Chapter 4, the gas temperature of the **rpdn!** in question remains at room temperature.

(de)excitation reactions. The first term includes the DC conductivity [90] of the plasma, and accounts for the heating of the electrons by the electric field. The second term is the elastic cooling of the electrons by the neutral atoms, where the gas temperature is assumed fixed. The third term is the energy gained or lost by the electrons in atomic (de)excitation reactions. Equation 5.6, with equations 5.5 and 5.2 are sufficient to solve for the evolution of the electron temperatures, electron densities, excited state densities, and plasma emissions as functions of time.

5.1.4 Model Solutions

Equation 5.2 can be rewritten for each atomic state, i , resulting in a set of linear, first order differential equations,

$$\begin{aligned}
 \frac{d}{dt} \begin{pmatrix} N_1 \\ N_2 \\ \vdots \\ N_M \end{pmatrix} &= n_e \begin{pmatrix} -\sum_{j \neq 1} K_{1,j}^e & K_{2,1}^e & \dots & K_{M,1}^e \\ K_{1,2}^e & -\sum_{j \neq 2} K_{2,j}^e & \dots & K_{M,2}^e \\ \vdots & \vdots & \ddots & \vdots \\ K_{1,M}^e & K_{2,M}^e & \dots & -\sum_{j \neq M} K_{M,j}^e \end{pmatrix} \cdot \begin{pmatrix} N_1 \\ N_2 \\ \vdots \\ N_M \end{pmatrix} \\
 &+ \begin{pmatrix} 0 & K_{2,1}^o & \dots & K_{M,1}^o \\ 0 & -\sum_{j < 2} K_{2,j}^e & \dots & K_{M,2}^o \\ \vdots & \vdots & \ddots & \vdots \\ 0 & 0 & \dots & -\sum_{j < M} K_{M,j}^e \end{pmatrix} \cdot \begin{pmatrix} N_1 \\ N_2 \\ \vdots \\ N_M \end{pmatrix} \\
 &+ N_g \begin{pmatrix} -\sum_{j \neq 1} K_{1,j}^a & K_{2,1}^a & \dots & K_{M,1}^a \\ K_{1,2}^a & -\sum_{j \neq 2} K_{2,j}^a & \dots & K_{M,2}^a \\ \vdots & \vdots & \ddots & \vdots \\ K_{1,M}^a & K_{2,M}^a & \dots & -\sum_{j \neq M} K_{M,j}^a \end{pmatrix} \cdot \begin{pmatrix} N_1 \\ N_2 \\ \vdots \\ N_M \end{pmatrix}, \tag{5.7}
 \end{aligned}$$

where M is the total number of atomic states and $\varepsilon_i < \varepsilon_{i+1}$. An additional equation can be added to separately account for electrons as well as electron-specific processes, however the model assumed quasineutrality by enforcing the relation $N_{ion} = n_e$. Changes in the density of each atomic state were calculated by numerical integration of these equations. The range of time scales exhibited by the RPND made it desirable to implement adaptive control of the time step size. For this reason, the Runge-Kutta-Fehlberg method, adapted from Bradie [129], was used.

Initial metastable densities were determined from the LAS measurements. Initial electron densities were determined from LCIF measurements made by Weatherford [121]. However, these measurements were only available for 1.0, 4.0, and 8.0 Torr. Exploratory simulations found that the final metastable density was a sensitive function of the initial electron population. As a result, model simulations were only conducted at these three conditions.

No electron temperature measurements were possible at the low densities in the prepulse period, therefore a temperature of 0.2 eV was assumed. This temperature was used to generate the equilibrium excited state densities for non-metastable states. As the LAS measurements showed no appreciable change in gas temperature, the neutral gas temperature was fixed at 300 K for the duration of the simulation.

Though the applied potential is well known, the actual form of $E(t)$ is significantly less clear. Again, FIW measurements such as those performed by Takashima et al. [87], as well as the RPND measurements of Ito et al. [79], and Müller [80] provide some idea of what to expect. Each study measured a Gaussian-like peak as the wave crossed the measurement point. In the quiescent period following the wave, a relatively small background electric field persisted, with a magnitude on the order of 20-25% of the of the wave. The duration and magnitude of this persistent field varied substantially between studies. Given the indeterminate value of this persistent field, the following simulations assumed a single Gaussian pulse for the form of the electric field. The time domain of the simulation was 190 ns, with the peak of the electric field pulse at 40 ns.

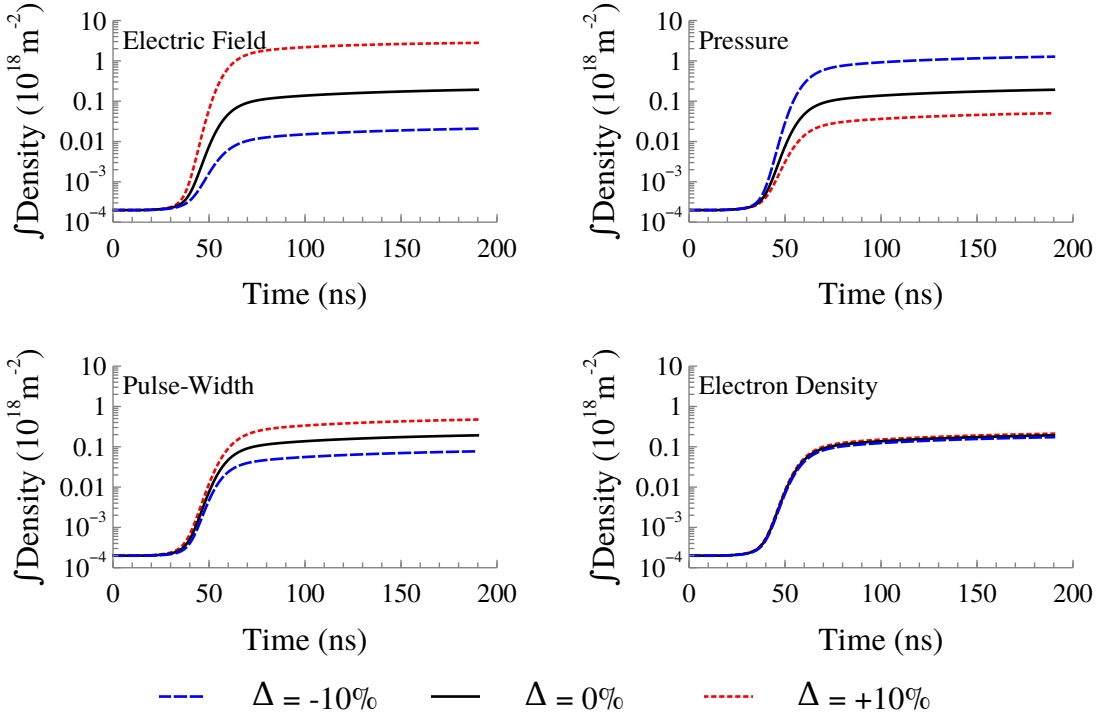


Figure 5.3: Simulations showing the effects of perturbations to the initial conditions on the metastable dynamics.

5.2 Perturbation Study

The global model simulations depended, to a large extent, on the initial conditions of the system. Without a clear process by which to calculate the error in the results of the simulations, it was desirable to investigate the sensitivity of the results to various factors. Of particular interest was how each variable affected the shape of the metastable dynamics. In order to examine these effects, a preliminary fit was made to the 4.0 Torr measurements, and the conditions of this fit were independently perturbed by $\pm 10\%$. The conditions studied were pressure, peak electric field, pulse-width, and initial electron density.

The results of these simulations are shown in figure 5.3

5.3 Plasma Dynamics

5.4 Summary

CHAPTER 6

Population Kinetics

CHAPTER 7

Conclusions

APPENDIX A

Millimeter-Wave Interferometry

APPENDIX B

Rotational Spectroscopy

As early as 2001, researchers have proposed the use of a novel, hybrid engine design for use in supersonic and hypersonic flight [130]. In some ways similar to an earlier program [131], it suggested that magnetohydrodynamic (MHD) accelerators were an enabling technology for hypersonic transport. Briefly, a MHD accelerator could be used to simultaneously produce energy and slow the inlet airflow. This would allow the use of a conventional turbojet engine at speeds well above its normal operational range.

However, MHD accelerators require an ionized fluid flow. Even at the high altitudes associated with hypersonic flight, this is not a trivial requirement. Originally, Macheret suggested the use of electron beams, carefully tuned to coincide with the peak in the ionization cross section. However, the use of electron beams in the ionization of high pressure gases is accompanied by a large number of technical issues, similar to those of some excimer lasers. Therefore, in 2002, Macheret et al. proposed the use of a RPND to produce an “electron beam” *in situ* [64] akin to the beams observed in certain FIW studies.

Previous studies of FIWs in air have observed fast gas heating of molecular systems [109]. Up to 40% of the input energy can be converted into translational energy through dissociation of oxygen and quenching or electronically excited nitrogen states. As the RPND physics are very similar to that of the FIW, there is the possibility that it may also cause fast gas heating. In combustion, this can play an important role in the chemistry, flame holding, and ignition delay. More generally, gas heating can impact material processing and

ionization efficiency. As such, it is important to develop reliable temperature diagnostics for RPNDs in molecular gases.

This appendix records the development of such a diagnostic for a moderate pressure RPND in air. The approach used measured the rotational spectra of a molecular system and used this information to infer the rotational temperature. As a result of the close energy-spacing of the rotational levels, this temperature is usually a good measure of the translational temperature of the system [132]. This technique is limited by the ability to detect light from the transitions, and by the equilibration time of the translational and rotational temperatures.

The measurement of rotational transitions is a common diagnostic for the measurement of gas temperatures, particularly in the field of combustion. Matching of the rotational spectra is typically accomplished with a computer program such as Specair [133] and LIF-BASE [134]. However, a survey of the available programs revealed little documentation about the calculation methods and none which provided the necessary flexibility how the spectra were generated. This necessitated the development of a program to automate the generation and matching of rotational spectra.

B.1 Experiment

B.2 Theory

B.3 Results

BIBLIOGRAPHY

- [1] J. J. Thomson. *Notes on Recent Researches in Electricity and Magnetism*. Clarendon Press, Oxford, UK, 1893.
- [2] J. D. Huba. *NRL Plasma Formulary*. Naval Research Laboratory, Washington, D.C., 2011.
- [3] J. I. Levatter and S. C. Lin. Necessary conditions for the homogeneous formation of pulsed avalanche discharges at high gas pressures. *Journal of Applied Physics*, 51(1):210, 1980.
- [4] E. E. Kunhardt and W. Byszewski. Development of overvoltage breakdown at high gas pressure. *Physical Review A*, 21(6):2069–2077, June 1980.
- [5] C. E. Moore and P. W. Merrill. Partial Grotrian Diagrams of Astrophysical Interest. Technical report, National Bureau of Standards, Washington, D.C., 1968.
- [6] C. K. Birdsall. Particle-in-cell charged-particle simulations, plus Monte Carlo collisions with neutral atoms, PIC-MCC. *IEEE Transactions on Plasma Science*, 19(2):65–85, April 1991.
- [7] Plasma 2010 Committee. *Plasma Science: Advancing Knowledge in the National Interest*. Number 2007. The National Academies Press, Washington, D.C., 2007.
- [8] K. E. Greenberg and G. A. Hebner. Electric-field measurements in 13.56 MHz helium discharges. *Applied Physics Letters*, 63(24):3282, 1993.
- [9] E. E. Kunhardt. Generation of large-volume, atmospheric-pressure, nonequilibrium plasmas. *IEEE Transactions on Plasma Science*, 28(1):189–200, 2000.
- [10] K. H. Becker, U. Kogelschatz, K. H. Schoenbach, and R. J. Barker. *Non-Equilibrium Air Plasmas at Atmospheric Pressure*. Institute of Physics Publishing, Bristol, UK, 2005.
- [11] S. Rauf and M. J. Kushner. Dynamics of a coplanar-electrode plasma display panel. II. Cell optimization. *Journal of Applied Physics*, 85(7):3470, 1999.
- [12] M. A. Malik, A. Ghaffar, and S. A. Malik. Water purification by electrical discharges. *Plasma Sources Science and Technology*, 10(1):82–91, February 2001.

- [13] H. Ayan, D. Staack, G. Fridman, A. Gutsol, Y. Mukhin, A. Yu. Starikovskii, A. Fridman, and G. Friedman. Application of nanosecond-pulsed dielectric barrier discharge for biomedical treatment of topographically non-uniform surfaces. *Journal of Physics D: Applied Physics*, 42(12):125202, June 2009.
- [14] M. Nishihara and I. V. Adamovich. Numerical Simulation of a Crossed Pulser-Sustainer Discharge in Transverse Magnetic Field. *IEEE Transactions on Plasma Science*, 35(5):1312–1324, October 2007.
- [15] K. Ostrikov, U. Cvelbar, and A. B. Murphy. Plasma nanoscience: setting directions, tackling grand challenges. *Journal of Physics D: Applied Physics*, 44(17):174001, May 2011.
- [16] U. Kogelschatz. Dielectric-Barrier Discharges: Their History, Discharge Physics, and Industrial Applications. *Plasma Chemistry and Plasma Processing*, 23(1):1–46, 2003.
- [17] F. Iza and J. Hopwood. Split-ring resonator microplasma: microwave model, plasma impedance and power efficiency. *Plasma Sources Science and Technology*, 14(2):397–406, May 2005.
- [18] I. V. Adamovich, W. R. Lempert, M. Nishihara, J. W. Rich, and Yu. G. Utkin. Repetitively Pulsed Nonequilibrium Plasmas for Magnetohydrodynamic Flow Control and Plasma-Assisted Combustion. *Journal of Propulsion and Power*, 24(6):1198–1215, November 2008.
- [19] L. M. Vasiliyak, S. V. Kostyuchenko, N. N. Kudryavtsev, and I. V. Filyugin. Fast ionisation waves under electrical breakdown conditions. *Physics-Uspekhi*, 37(3):247–268, March 1994.
- [20] J. L. Walsh, J. J. Shi, and M. G. Kong. Submicrosecond pulsed atmospheric glow discharges sustained without dielectric barriers at kilohertz frequencies. *Applied Physics Letters*, 89(16):161505, 2006.
- [21] S. M. Starikovskaia, A. Yu. Starikovskii, and D. V. Zatsepин. The development of a spatially uniform fast ionization wave in a large discharge volume. *Journal of Physics D: Applied Physics*, 31(9):1118–1125, May 1998.
- [22] L. Tonks and I. Langmuir. A General Theory of the Plasma of an Arc. *Physical Review*, 34(6):876–922, September 1929.
- [23] A. Anders. Tracking down the origin of arc plasma science-II. early continuous discharges. *IEEE Transactions on Plasma Science*, 31(5):1060–1069, October 2003.
- [24] S. M. Starikovskaia, N. B. Anikin, S. V. Pancheshnyi, D. V. Zatsepин, and A. Yu. Starikovskii. Pulsed breakdown at high overvoltage: development, propagation and energy branching. *Plasma Sources Science and Technology*, 10(2):344–355, May 2001.

- [25] V. M. Efanov, V. V. Karavaev, A. F. Kardo-Sysoev, and I. G. Tchashnikov. Fast ionization dynistor (FID)-a new semiconductor superpower closing switch. In *Digest of Technical Papers. 11th IEEE International Pulsed Power Conference (Cat. No.97CH36127)*, volume 2, pages 988–991. IEEE, 1997.
- [26] L. B. Loeb. Ionizing Waves of Potential Gradient: Luminous pulses in electrical breakdown, with velocities a third that of light, have a common basis. *Science (New York, N.Y.)*, 148(3676):1417–26, June 1965.
- [27] C. Wheatstone. Versuche, die Geschwindigkeit der Elektricität und die Dauer des elektrischen Lichts zu messen. *Annalen der Physik und Chemie*, 110(3):464–480, 1835.
- [28] W. v. Zahn. Spectralröhren mit longitudinaler Durchsicht. *Annalen der Physik und Chemie*, 244(12):675–675, 1879.
- [29] J. James. Die Abraham-Lemoinesche Methode zur Messung sehr kleiner Zeitintervalle und ihre Anwendung zur Bestimmung der Richtung und Geschwindigkeit der Entladung in Entladungsrohren. *Annalen der Physik*, 320(15):954–987, 1904.
- [30] R. Whiddington. The Discharge of Electricity through Vacuum Tubes. *Nature*, 116(2918):506–509, October 1925.
- [31] J. Beams. The Time Interval Between the Appearance of Spectrum Lines in Spark and in Condensed Discharges. *Physical Review*, 28(3):475–480, September 1926.
- [32] B. F. J. Schonland and H. Collens. Development of the Lightning Discharge. *Nature*, 132(3332):407–408, September 1933.
- [33] A. M. Cravath and L. B. Loeb. The Mechanism of the High Velocity of Propagation of Lightning Discharges. *Physics*, 6(4):125, 1935.
- [34] L. Snoddy, J. Beams, and J. Dietrich. The Propagation of Potential in Discharge Tubes. *Physical Review*, 50(5):469–471, September 1936.
- [35] E. Flegler and H. Raether. Der elektrische Durchschlag in Gasen nach Untersuchungen mit der Nebelkammer. *Zeitschrift f r Physik*, 99(9-10):635–642, September 1936.
- [36] L. B. Loeb and J. M. Meek. The Mechanism of Spark Discharge in Air at Atmospheric Pressure. I. *Journal of Applied Physics*, 11(6):438, June 1940.
- [37] L. B. Loeb and J. M. Meek. The Mechanism of Spark Discharge in Air at Atmospheric Pressure. II. *Journal of Applied Physics*, 11(7):459, 1940.
- [38] J. Meek. A Theory of Spark Discharge. *Physical Review*, 57(8):722–728, April 1940.
- [39] L. Fisher and B. Bedderson. Formative Time Lags of Spark Breakdown in Air in Uniform Fields at Low Overvoltages. *Physical Review*, 81(1):109–114, January 1951.

- [40] G. Kachickas and L. Fisher. Formative Time Lags of Uniform Field Breakdown in N₂. *Physical Review*, 88(4):878–883, November 1952.
- [41] G. Kachickas and L. Fisher. Formative Time Lags of Uniform Field Breakdown in Argon. *Physical Review*, 91(4):775–779, August 1953.
- [42] E. E. Kunhardt and Y. Tzeng. Development of an electron avalanche and its transition into streamers. *Physical review. A*, 38(3):1410–1421, August 1988.
- [43] I. D. Chalmers. The transient glow discharge in nitrogen and dry air. *Journal of Physics D: Applied Physics*, 4(8):1147–1151, August 1971.
- [44] W. Rogowski, E. Flegler, and R. Tamm. Über Wanderwelle und Durchschlag. *Archiv für Elektrotechnik*, 18(5):479–512, September 1927.
- [45] K. Buss. Der Stufendurchschlag. *Archiv für Elektrotechnik*, 26(4):266–272, April 1932.
- [46] T. E. Allibone and J. M. Meek. The Development of the Spark Discharge. II. *Proceedings of the Royal Society A: Mathematical, Physical and Engineering Sciences*, 169(937):246–268, December 1938.
- [47] T. E. Allibone and J. M. Meek. The Development of the Spark Discharge. *Proceedings of the Royal Society A: Mathematical, Physical and Engineering Sciences*, 166(924):97–126, May 1938.
- [48] T. E. Allibone. The Mechanism of a Long Spark. *Journal of the Institute of Electrical Engineers*, 82(497):513–521, 1938.
- [49] C. V. Boys. Progressive Lightning. *Nature*, 118(2977):749–750, November 1926.
- [50] T. E. Allibone. Development of the Spark Discharge. *Nature*, 161(4103):970–971, June 1948.
- [51] R. F. Saxe and J. M. Meek. Development of Spark Discharges. *Nature*, 162(4111):263–264, August 1948.
- [52] Yu. L. Stankevich and V. G. Kalinin. Fast Electrons and X-Ray Radiation during the Initial Stage of Growth of a Pulsed Spark Discharge in Air. *Soviet Physics Doklady*, 12, 1968.
- [53] G. A. Mesyats, Yu. I. Bychkov, and V. V. Kremnev. Pulsed nanosecond electric discharges in gases. *Soviet Physics Uspekhi*, 15(3):282–297, March 1972.
- [54] L. P. Babich, T. V. Loiko, and L. V. Tarasova. The physics of high-voltage nanosecond discharges in dense gases. *Radiophysics and Quantum Electronics*, 20(4):436–442, April 1977.

- [55] L. P. Babich, T. V. Loško, and V. A. Tsukerman. High-voltage nanosecond discharge in a dense gas at a high overvoltage with runaway electrons. *Soviet Physics Uspekhi*, 33(7):521–540, July 1990.
- [56] C. A. Fenstermacher. Electron-Beam-Controlled Electrical Discharge as a Method of Pumping Large Volumes of CO₂ Laser Media at High Pressure. *Applied Physics Letters*, 20(2):56, 1972.
- [57] A. J. Palmer. A physical model on the initiation of atmospheric-pressure glow discharges. *Applied Physics Letters*, 25(3):138, 1974.
- [58] R. O. Hunter. Electron beam controlled switching. In *International Pulsed Power Conference*, pages IC8–1 –IC8–6, New York, NY, 1976. Institute of Electrical Engineers, Inc.
- [59] B. M. Koval’chuk and G. A. Mesyats. Rapid cutoff of a high current in an electron-beam-excited discharge. *Soviet Technical Physics Letters*, 2(252), 1976.
- [60] B. B. Slavin and P. I. Sopin. Breakdown of a neutral gas by ionizing waves of the gradient of a negative potential. *High Temperature*, 30(1):1–9, 1992.
- [61] S. M. Starikovskaya and A. Yu. Starikovskii. Numerical modelling of the electron energy distribution function in the electric field of a nanosecond pulsed discharge. *Journal of Physics D: Applied Physics*, 34(23):3391–3399, December 2001.
- [62] S. V. Pancheshnyi, D. A. Lacoste, A. Bourdon, and C. O. Laux. Ignition of Propane-Air Mixtures by a Repetitively Pulsed Nanosecond Discharge. *IEEE Transactions on Plasma Science*, 34(6):2478–2487, December 2006.
- [63] S. M. Starikovskaya. Plasma assisted ignition and combustion. *Journal of Physics D: Applied Physics*, 39(16):R265–R299, August 2006.
- [64] S. O. Macheret, M. N. Schneider, and R. B. Miles. Modeling of air plasma generation by repetitive high-voltage nanosecond pulses. *IEEE Transactions on Plasma Science*, 30(3):1301–1314, June 2002.
- [65] S. J. Schneider, H. Kamhawi, and I. M. Blankson. Efficient Ionization Investigation for Flow Control and Energy Extraction. *AIAA 47th Aerospace Sciences Meeting*, 2009.
- [66] A. Yu. Starikovskii, A. A. Nikipelov, M. M. Nudnova, and D. V. Roupasov. SDBD plasma actuator with nanosecond pulse-periodic discharge. *Plasma Sources Science and Technology*, 18(3):034015, August 2009.
- [67] I. V. Adamovich, M. Nishihara, I. Choi, M. Uddi, and W. R. Lempert. Energy coupling to the plasma in repetitive nanosecond pulse discharges. *Physics of Plasmas*, 16(11):113505, 2009.

- [68] D. S. Nikandrov, L. D. Tsendar, V. I. Kolobov, and R. R. Arslanbekov. Theory of Pulsed Breakdown of Dense Gases and Optimization of the Voltage Waveform. *IEEE Transactions on Plasma Science*, 36(1):131–139, 2008.
- [69] J. L. Zimmermann, T. Shimizu, H. U. Schmidt, Y. F. Li, G. E. Morfill, and G Isbary. Test for bacterial resistance build-up against plasma treatment. *New Journal of Physics*, 14(7):073037, July 2012.
- [70] J. E. Foster, G. Adamovsky, S. N. Gucker, and I. M. Blankson. A Comparative Study of the Time-Resolved Decomposition of Methylene Blue Dye Under the Action of a Nanosecond Repetitively Pulsed DBD Plasma Jet Using Liquid Chromatography and Spectrophotometry. *IEEE Transactions on Plasma Science*, 41(3):503–512, March 2013.
- [71] G. Pilla, D. Galley, D. A. Lacoste, F. Lacas, D. Veynante, and C. O. Laux. Stabilization of a Turbulent Premixed Flame Using a Nanosecond Repetitively Pulsed Plasma. *IEEE Transactions on Plasma Science*, 34(6):2471–2477, December 2006.
- [72] M. Nishihara, J. W. Rich, W. R. Lempert, I. V. Adamovich, and S. Gogineni. Low-temperature $M=3$ flow deceleration by Lorentz force. *Physics of Fluids*, 18(8):086101, 2006.
- [73] A. Bao, Yu. G. Utkin, S. Keshav, G. Lou, and I. V. Adamovich. Ignition of Ethylene–Air and Methane–Air Flows by Low-Temperature Repetitively Pulsed Nanosecond Discharge Plasma. *IEEE Transactions on Plasma Science*, 35(6):1628–1638, December 2007.
- [74] G. Lou, A. Bao, M. Nishihara, S. Keshav, Yu. G. Utkin, J. W. Rich, W. R. Lempert, and I. V. Adamovich. Ignition of premixed hydrocarbon–air flows by repetitively pulsed, nanosecond pulse duration plasma. *Proceedings of the Combustion Institute*, 31(2):3327–3334, January 2007.
- [75] D. Z. Pai, G. D. Stancu, D. A. Lacoste, and C. O. Laux. Nanosecond repetitively pulsed discharges in air at atmospheric pressure—the glow regime. *Plasma Sources Science and Technology*, 18(4):045030, November 2009.
- [76] Y. Zuzeek, I. Choi, M. Uddi, I. V. Adamovich, and W. R. Lempert. Pure rotational CARS thermometry studies of low-temperature oxidation kinetics in air and ethene–air nanosecond pulse discharge plasmas. *Journal of Physics D: Applied Physics*, 43(12):124001, March 2010.
- [77] M. Nishihara, K. U. Takashima, J. R. Bruzzese, I. V. Adamovich, and D. Gaitonde. Experimental and Computational Studies of Low-Temperature Mach 4 Flow Control by Lorentz Force. *Journal of Propulsion and Power*, 27(2):467–476, March 2011.
- [78] T. Ito, D. Luggenhölscher, K. Kobayashi, S. Müller, U. Czarnetzki, and S. Hamaguchi. Electric field measurement in an atmospheric or higher pressure gas by coherent Raman scattering of nitrogen. *Journal of Physics D: Applied Physics*, 42(9):092003, May 2009.

- [79] T. Ito, K. Kobayashi, U. Czarnetzki, and S. Hamaguchi. Rapid formation of electric field profiles in repetitively pulsed high-voltage high-pressure nanosecond discharges. *Journal of Physics D: Applied Physics*, 43(6):062001, February 2010.
- [80] S. Müller, D. Luggenhölscher, and U. Czarnetzki. Ignition of a nanosecond-pulsed near atmospheric pressure discharge in a narrow gap. *Journal of Physics D: Applied Physics*, 44(16):165202, April 2011.
- [81] S. O. Macheret, M. N. Shneider, and R. C. Murray. Ionization in strong electric fields and dynamics of nanosecond-pulse plasmas. *Physics of Plasmas*, 13(2):023502, 2006.
- [82] M. Laroussi and X. Lu. Room-temperature atmospheric pressure plasma plume for biomedical applications. *Applied Physics Letters*, 87(11):113902, 2005.
- [83] X. Lu and M. Laroussi. Dynamics of an atmospheric pressure plasma plume generated by submicrosecond voltage pulses. *Journal of Applied Physics*, 100(6):063302, 2006.
- [84] J. L. Walsh, D. X. Liu, F. Iza, M. Z. Rong, and M. G. Kong. Contrasting characteristics of sub-microsecond pulsed atmospheric air and atmospheric pressure helium–oxygen glow discharges. *Journal of Physics D: Applied Physics*, 43(3):032001, January 2010.
- [85] G. V. Naidis. Modelling of streamer propagation in atmospheric-pressure helium plasma jets. *Journal of Physics D: Applied Physics*, 43(40):402001, October 2010.
- [86] D. Breden, K. Miki, and L. L. Raja. Computational study of cold atmospheric nanosecond pulsed helium plasma jet in air. *Applied Physics Letters*, 99(11):111501, 2011.
- [87] K. U. Takashima, I. V. Adamovich, Z. Xiong, M. J. Kushner, S. M. Starikovskaia, U. Czarnetzki, and D. Luggenhölscher. Experimental and modeling analysis of fast ionization wave discharge propagation in a rectangular geometry. *Physics of Plasmas*, 18(8):083505, 2011.
- [88] P. M. Bellan. *Fundamentals of Plasma Physics*. Cambridge University Press, 2008.
- [89] M. J. Druyvesteyn and F. M. Penning. The Mechanism of Electrical Discharges in Gases of Low Pressure. *Reviews of Modern Physics*, 12(2):87–174, April 1940.
- [90] M. A. Lieberman and A. J. Lichtenberg. *Principles of Plasma Discharges and Materials Processing*. John Wiley & Sons, Inc., Hoboken, NJ, USA, 2nd edition, April 2005.
- [91] F. F. Chen. *Introduction to plasma physics and controller fusion*. Springer, New York, NY, 2nd edition, 1984.

- [92] L. G. H. Huxley, R. W. Crompton, and M. T. Elford. Use of the parameter E/N. *British Journal of Applied Physics*, 17(9):1237–1238, September 1966.
- [93] J. Hornbeck. The Drift Velocities of Molecular and Atomic Ions in Helium, Neon, and Argon. *Physical Review*, 84(4):615–620, November 1951.
- [94] A. V. Phelps. Compilation of Electron Cross Sections, 2002.
- [95] T. W. Johns. Ionization Instability in Atmospheric-Pressure Gas Discharges. *Applied Physics Letters*, 20(12):495, June 1972.
- [96] H. R. Griem. *Principles of Plasma Spectroscopy*. Cambridge University Press, Cambridge, UK, 2005.
- [97] G. W. F. Drake. *Springer Handbook of Atomic, Molecular, and, Optical Physics: High Precision Calculations for Helium*. Springer New York, New York, NY, January 2006.
- [98] G. Herzberg. *Atomic Spectra and Atomic Structure*. Dover Publications, New York, NY, 2nd edition, 1944.
- [99] A. E. Siegman. *Lasers*. University Science Books, Sausalito, CA, 1986.
- [100] H. J. Kunze. *Introduction to Plasma Spectroscopy*, volume 56 of *Springer Series on Atomic, Optical, and Plasma Physics*. Springer Berlin Heidelberg, Berlin, Heidelberg, 2009.
- [101] W. Demtröder. *Laser Spectroscopy, Vol. 1*. Springer Berlin Heidelberg, Berlin, Heidelberg, 2008.
- [102] A. Kramida, Yu. Ralchenko, J. Reader, and NIST ASD Team. NIST Atomic Spectra Database (version 5.0), 2012.
- [103] A. F. H. van Gessel, E. A. D. Carbone, P. J. Bruggeman, and J. J. A. M. van der Mullen. Laser scattering on an atmospheric pressure plasma jet: disentangling Rayleigh, Raman and Thomson scattering. *Plasma Sources Science and Technology*, 21(1):015003, February 2012.
- [104] A. V. Phelps and J. Molnar. Lifetimes of Metastable States of Noble Gases. *Physical Review*, 89(6):1202–1208, March 1953.
- [105] M. W. Millard, P. P. Yaney, B. N. Ganguly, and C. A. DeJoseph. Diode laser absorption measurements of metastable helium in glow discharges. *Plasma Sources Science and Technology*, 7(3):389–394, August 1998.
- [106] D. W. Marquardt. An Algorithm for Least-Squares Estimation of Nonlinear Parameters. *Journal of the Society for Industrial and Applied Mathematics*, 11(2):431–441, June 1963.

- [107] E. Jones, T. Oliphant, and P. Peterson. SciPy: Open Source Scientific Tools for Python, 2001.
- [108] M. W. Kiehlbauch and D. B. Graves. Inductively coupled plasmas in oxygen: Modeling and experiment. *Journal of Vacuum Science & Technology A: Vacuum, Surfaces, and Films*, 21(3):660, 2003.
- [109] N. A. Popov. Fast gas heating in a nitrogen–oxygen discharge plasma: I. Kinetic mechanism. *Journal of Physics D: Applied Physics*, 44(28):285201, July 2011.
- [110] N. L. Aleksandrov, S. V. Kindysheva, M. M. Nudnova, and A. Yu. Starikovskii. Mechanism of ultra-fast heating in a non-equilibrium weakly ionized air discharge plasma in high electric fields. *Journal of Physics D: Applied Physics*, 43(25):255201, June 2010.
- [111] S. V. Pancheshnyi. Collisional deactivation of N₂(C3Πu, v=0, 1, 2, 3) states by N₂, O₂, H₂ and H₂O molecules. *Chemical Physics*, 262(2-3):349–357, December 2000.
- [112] N. L. Aleksandrov, S. V. Kindysheva, A. A. Kirpichnikov, I. N. Kosarev, S. M. Starikovskaia, and A. Yu. Starikovskii. Plasma decay in N₂, CO₂ and H₂O excited by high-voltage nanosecond discharge. *Journal of Physics D: Applied Physics*, 40(15):4493–4502, August 2007.
- [113] J. M. Pouvesle, a. Khacef, J. Stevefelt, H. Jahani, V. T. Gylys, and C. B. Collins. Study of two-body and three-body channels for the reaction of metastable helium atoms with selected atomic and molecular species. *The Journal of Chemical Physics*, 88(5):3061, 1988.
- [114] K. Urabe, T. Morita, K. Tachibana, and B. N. Ganguly. Investigation of discharge mechanisms in helium plasma jet at atmospheric pressure by laser spectroscopic measurements. *Journal of Physics D: Applied Physics*, 43(9):095201, March 2010.
- [115] G. Nersisyan, T. Morrow, and W. G. Graham. Measurements of helium metastable density in an atmospheric pressure glow discharge. *Applied Physics Letters*, 85(9):1487, August 2004.
- [116] R. Deloche, P. Monchicourt, M. Cheret, and F. Lambert. High-pressure helium afterglow at room temperature. *Physical Review A*, 13(3):1140–1176, March 1976.
- [117] S. Rauf and M. J. Kushner. Dynamics of a coplanar-electrode plasma display panel cell. I. Basic operation. *Journal of Applied Physics*, 85(7):3460, 1999.
- [118] T. J. Linde, T. I. Gombosi, P. L. Roe, K. G. Powell, and D. L. DeZeeuw. Heliosphere in the magnetized local interstellar medium: Results of a three-dimensional MHD simulation. *Journal of Geophysical Research*, 103(A2):1889, 1998.
- [119] G. J. M. Hagelaar and L. C. Pitchford. Solving the Boltzmann equation to obtain electron transport coefficients and rate coefficients for fluid models. *Plasma Sources Science and Technology*, 14(4):722–733, November 2005.

- [120] B. R. Weatherford, E. V. Barnat, Z. Xiong, and M. J. Kushner. Two-Dimensional Electron and Metastable Density Profiles Produced in Helium Fast Ionization Wave Discharges. *Bulletin of the American Physical Society*, Volume 57,, October 2012.
- [121] B. R. Weatherford. (personal communication), 2012.
- [122] A. Catherinot and B. Dubreuil. Quenching and excitation-transfer processes in the n=4 helium sublevels in a low-pressure glow discharge. *Physical Review A*, 23(2):763–774, February 1981.
- [123] B. Dubreuil and A. Catherinot. Quenching and excitation transfer in the n=3 helium sublevels in a low-pressure glow discharge. *Physical Review A*, 21(1):188–199, January 1980.
- [124] Yu. Ralchenko, R. K. Janev, T. Kato, D. V. Fursa, I. Bray, and F. J. de Heer. Electron-impact excitation and ionization cross sections for ground state and excited helium atoms. *Atomic Data and Nuclear Data Tables*, 94(4):603–622, July 2008.
- [125] S. N. Nahar. Photoionization and electron–ion recombination of He I. *New Astronomy*, 15(5):417–426, July 2010.
- [126] J. P. Verboncoeur, M. V. Alves, V. Vahedi, and C. K. Birdsall. Simultaneous Potential and Circuit Solution for 1D Bounded Plasma Particle Simulation Codes. *Journal of Computational Physics*, 104(2):321–328, February 1993.
- [127] L. L. Alves and C. M. Ferreira. IST-Lisbon Helium Cross Sections. Technical report, Instituto Superior Técnico, Lisbon, PT, 2013.
- [128] J. L. Pack, R. E. Voshall, A. V. Phelps, and L. E. Kline. Longitudinal electron diffusion coefficients in gases: Noble gases. *Journal of Applied Physics*, 71(11):5363, 1992.
- [129] B. Bradie. *A Friendly Introduction to Numerical Analysis*. Pearson Education, Upper Saddle River, NJ, 1 edition, 2006.
- [130] S. O. Macheret, R. J. Lipinski, R. B. Miles, and M. N. Shneider. Electron-Beam-Generated Plasmas in Hypersonic Magnetohydrodynamic Channels. *AIAA Journal*, 39(6):1127–1138, June 2001.
- [131] E. P. Gurijanov and P. T. Harsha. AJAX: New Directions in Hypersonic Technology. In *International Space Planes and Hypersonic Systems and Technologies*, pages 1–9, Seal Beach, CA, 1996. AIAA.
- [132] C. O. Laux. *Optical Diagnositcs and Radiative Emission of Air Plasmas*. PhD thesis, Stanford University, 1993.
- [133] C. O. Laux. Radiation and Nonequilibrium Collisional-Radiative Models. In D. Fletcher, J.-M. Charbonnier, G. S. R. Sarma, and T. Magin, editors, *von Karman Institute Lecture Series 2002-07*, Rhode-Saint-Genese, Belgium, 2002.

- [134] J. Luque and D. R Crosley. LIFBASE: Database and spectral simulation program, 1999.